Università degli studi ROMA TRE

PhD in Civil Engineering
XXII Cycle

PhD Thesis

Numerical modeling of waves for a tsunami early warning system

PhD Student: Claudia Cecioni

Tutors: Prof. Leopoldo Franco

Ing. Giorgio Bellotti

PhD Coordinator: Prof. Leopoldo Franco

Rome, February 2010

Collana delle tesi di Dottorato di Ricerca
In Scienze dell'Ingegneria Civile
Università degli Studi Roma Tre
Tesi n° 26

To my father Michele,
my mother Antonella
and my sister Martina

Acknowledgments

It is a pleasure to thank those who made this thesis possible. First and foremost I would like to thank my advisors Prof. Leopoldo Franco and Eng. Giorgio Bellotti. Their guidance and questions have been inspiring and extremely helpful in defining the research work of this thesis.

I had the opportunity to spend a visiting period, during my PhD years, at the Johns Hopkins University of Baltimore, MD, USA. I'm grateful to Prof. Robert A. Dalrymple for having shared with me his excellent knowledge in the field of Coastal Engineering.

I have also benefited from comments and discussions at various stage of the thesis from my colleagues Alessandro, Antonio, Elisa, Francesca, Marcello, Michele and Pietro. My PhD studies have been special thanks to them, not only for the enriching conversations, but because they have been a wonderful company during these years.

All my friends should deserve to be mentioned since they have been of strong support even from afar. Thanks to Annalisa and Muriel, and to Myriam and Ginevra.

A special thanks goes to Michele, for standing by my side and having encouraged me in all my ups and downs of my PhD studies.

This thesis is dedicated to my family, who always give me support and important advices.

Abstract

A numerical model based on the mild slope equation is applied to reproduce the propagation of small amplitude transient waves over mildly sloped sea bed. The model makes use of the Fourier transform to convert the time dependent hyperbolic equation into a set of elliptic equations in the frequency domain. Therefore the reproduction of the full frequency dispersion of waves is achieved, since each frequency component is solved using a dedicated elliptic equation.

The model results suitable to reproduce the tsunami far field propagation. Tsunamis are traditionally considered extremely long, single waves able of devastating the coast; however it has become well accepted that these kind of waves is a wave packet, that in most cases may exhibit a frequency dispersive behavior.

The results of available experimental studies on tsunami generated by landslides are used to validate the model. In the present work the waves generation is analyzed trough a wave-maker boundary condition, which works as a wave paddle in the physical models, otherwise it is included in the field equation. The mild slope equation is derived again taking into account the movement of the sea bottom, thus in the equation appears a forcing term which represents the effects of a tsunamogenic source. Validation and discussion about the effects of the source term, for different bottom movements, are presented. The comparison with other laboratory experiments were used to gain insigth on tsunami generation and propagation phenomena, and to test the model application in a tsunami early warning.

An important feature of the model, that in our opinion makes it suitable to be used in early warning, is that can be applied in two stages: one is extremely expensive from the computational point of view, the other is very fast and can be applied in real-time. Therefore the idea, when setting up an early warning system, is to define the scenarios and to perform the a

priori computations, then the results can be used for the simulation in real time, forecasting the properties of the waves at the desired points of the computational domain at an acceptable costs.

An example application of tsunamis propagating around the Stromboli island, in the south Tyrrhenian sea, Italy, is also presented to show the applicability of the present approach to real life scenarios.

Sommario

Un modello numerico basato sulla risoluzione dell'equazione 'mild slope equation' (MSE), è applicato per simulare la propagazione di onde di piccola ampiezza su fondali a debole pendenza. La MSE è un'equazione integrata sulla verticale e può essere scritta in termini di elevazione della superficie libera o di potenziale di velocità. La MSE scritta nel dominio del tempo è un'equazione iperbolica; nel presente modello l'equazione è risolta nel dominio della frequenza: applicando la trasformata di Fourier si ottiene un set di equazioni ellittiche, ciascuna delle quali risolve una componente in frequenza dello spettro ondametrico. In tal modo il modello risulta in grado di riprodurre la completa dispersione in frequenza delle onde.

Il modello è applicato per simulare la propagazione delle onde di maremoto (tsunamis) nel campo lontano. Nonostante le onde di maremoto siano considerate come onde estremamente lunghe, capaci di inondare e devastare la costa, negli ultimi anni è stato dimostrato che tali onde presentano un comportamento dispersivo in frequenza, tale per cui l'approssimazione di acque basse può risultare limitativa.

Il modello è stato validato tramite i risultati di alcuni esperimenti di laboratorio che riproducono onde di impulso generate dalla caduta di corpi rigidi in acqua. Tali esperimenti e il presente modello numerico sono stati implementati nell'ambito di una ricerca volta allo studio delle onde di maremoto generate da frana. La modellazione numerica della generazione delle onde è studiata attraverso una condizione al contorno, che impone una determinata velocità o elevazione della superficie libera ad un contorno del dominio di calcolo, oppure attraverso un termine sorgente inserito nell'equazione di campo. Nel presente lavoro la MSE è derivata anche nella condizione in cui si ammette una condizione al contorno sul fondale marino che varia anche nel tempo, rappresentando così il passaggio della frana o un terremoto sottomarino.

Il modello si presta adatto all'applicazione in un sistema di allerta tsunami (Tsunami Early Warning System) in quanto si può risolvere in due fasi. In una prima fase vengono riprodotti degli scenario di maremoto, conoscendo le possibili aree di generazione e ipotizzando l'intensità della causa di generazione. Questa prima fase richiede costi di calcolo elevati e per questo motivo deve essere risolta a priori. La seconda fase avviene in tempo reale, allorquando si verifica un evento di maremoto. Servendosi delle simulazioni già svolte e di misure di rilevamento dello onda di maremoto in tempo reale, il modello prevede le caratteristiche del maremoto nei punti di interesse e in tempi utili per mandare l'allarme.

E' inoltre mostrato un esempio di applicazione del modello nel sud del Mar Tirreno, Italia. L'esempio riproduce un evento di maremoto causato dalla caduta di una frana dall'isola di Stromboli. Quest'isola è un vulcano ancora attivo e, ad eventi eruttivi più gravosi, possono essere associati dislocamenti di terreno che, impattando sulla superficie del mare, possono generare onde di maremoto, come è successo il 30 Dicembre del 2002.

Contents

List of Figures

List of Tables

List of Symbol

BTE	Boussinesq Type Equations	[...]
L	Wave length	$[m]$
LSWE	Linear Shallow Water Equations	[...]
MSE	Mild Slope Equation	[...]
$N(x, y, \omega)$	Fourir transform of $\eta(x, y, t)$	$[m]$
NLSWE	Nonlinear Shallow Water Equations	[...]
T	Wave period	$[s]$
TEWS	Tsunami Early Warning System	[...]
c	Phase celerity	$[m/s]$
c_g	Group celerity	$[m/s]$
g	Gravity acceleration	$[m/s^2]$
$h(x, y, t)$	Water depth function	$[m]$
k	Wave number	$[rad/m]$
$p(x, y, z, t)$	Fluid pressure	$[N/m^2]$
$\mathbf{v} = (u, v, w)$	Fluid velocity vector	$[m/s]$
α	Sea bottom slope	$[rad]$
ϵ	Amplitude parameter	[...]
η	Water free surface elevation	$[m]$
μ	Wave length parameter	[...]
ρ	Fluid density	$[kg/m^3]$
$\phi(x, y, z, t)$	Velocity potential	$[m^2/s]$
$\Phi(x, y, z, \omega)$	Fourier transform of the velocity potential	$[m^2/s]$
ω	Angular frequency	$[rad/s]$

Chapter 1

Introduction

1.1 Tsunami

In the Coastal Engineering international scientific community, tsunamis are long water waves triggered by a sudden disturbance of the sea/ocean floor or the sea/ocean surface, which is usually caused by earthquakes, landslides or volcanic eruptions. The word tsunamis comes from the Japanese, with the meaning "harbor wave", and is related to the excitation of seiches induced into a harbor when the long tsunamis wave enters the closed basin. Both energy and momentum can take tsunamis waves thousands of kilometers across open ocean, carrying destruction on far shores hours after the impulse generating event. In deep water conditions, tsunamis can travel at celerities of 600-800 kilometers per hour, presenting wave heights of the order of some centimeters, wavelengths of the order of hundreds of kilometers. As the wave approaches shallow water near the coast, the wave celerity is reduced and the wave height significantly increases, sometimes exceeding also the value of 20 meters, with wave periods up to 20/30 minutes. Tsunamis are able to produce high wave runups which can flood the coastal areas and even destroy a city in the coast, and they are so destructive and dangerous even because can be rarely detected in open seas. Therefore it is very important the analysis of this phenomenon, especially considering the safety aspects related to the human activities along the coasts. Tsunamis waves have largely occurred in the oceans and well known is the tragic event of Sumatra Island, in the Indian Ocean, occurred the 26^{th} of December 2004 which caused the loss of about 300,000 human life; however very dangerous events have been also

registered in the Mediterranean sea, such as that occurred the 21^{st} of July, AD 365, at Alexandria, which caused 50,000 deaths, and that one occurred the December 28^{th}, 1908, at Messina, which caused 120,000 deaths. Regarding the Mediterranean sea, it is worth to mention the event occurred at the Stromboli volcano, on December 30, 2002, because is the case study of the present work. No human lives were lost, but the wave damaged properties along the shorelines of the Stromboli island and excited resonant modes of harbors along the coasts of Calabria.

1.1.1 Tsunamis generated by landslides

Waves generated by submarine or subaerial landslides are a particular type of tsunami waves. They can be triggered by landslides falling in artificial reservoirs, as the event of the Vayont valley, Italy, 1963 (Panizzo et al., 2005) or in natural lakes, or moreover in sea shorelines, as the event of Lituya Bay, Alaska, 1958 (Miller, 1960; Fritz et al., 2001), or the one of Stromboli volcano, Italy, 2002 (Tinti et al., 2005, 2006a, 2006b). Differently from tsunami waves triggered by a submarine disturbance, the subaerial landslide generated waves produce splashes and complex three dimensional water flows in the vicinity of the impact area. Then the perturbation travels for long distances, producing high water waves in the shallow water areas. In terms of the tsunamis generation mechanisms, two main differences can be found between tsunami waves triggered by landslides or by seismic disturbance of the sea floor. The first difference is on the duration of the generation process: a landslide takes more time to stop its movement, about the order of several minutes longer comparing to sea floor seismic motion. The second difference is in the source area involved in a seismic floor deformation which is larger than that of a landslide movement. Hence, coseismic displacements or vertical seafloor deformations, often generate tsunamis with long wavelength and long period, and their wave height, relatively small, is related with the earthquake magnitude. While tsunami generated by landslides are only limited in height by the landslide vertical displacement, which may reach several thousand meters.
Landslides falling into water represent one of the greatest tsunami hazards for coastal population and infrastructures, because of their consequences of flood and inundation, and because they offer little time for warning due to their proximity to the shore. In the case of artificial reservoirs the most

dramatic consequences are the dam overtopping, the flooding of the lake shorelines, and the seiching waves of the basin. It is clear how is important the understanding and the forecasting of landslide generated waves both for the safety of people and properties which are close to the impact area, and for the artificial reservoirs and dam management.
The generation of impulsive waves due to the impact of subaerial landslide into water is a complex phenomenon, involving several physical aspects. A first simplification can be done considering the whole phenomenon distinct in four phases, as it was proposed by Huber and Hager (1997). As can be seen from the sketch in Figure 1.1, in the first step the landslide starts moving, accelerates and then falls into water. The study of this part of the process lies in the scientific field of geology and soil mechanics. Step 2 sketches the impact of the landslide into water. This part of the process is at the base of wave generation, due to the energy exchange mechanism between the landslide and the water. The principal landslide parameters, (i.e. its volume, impact velocity, density, shape of the front, slope inclination angle) influence the features of the subsequent water wave motion. In the third step impulsive waves propagate into the reservoir or in the open sea, presenting a wave energy dispersion which is both longitudinal and directional. During the propagation wave features change as a function of the water depth, and refraction, diffraction and shoaling may occur. Finally, step 4 is related to the impulsive wave interaction with shorelines or structures. The impulsive wave runup may cause the flood of coastal areas, and, in the case of artificial reservoir, the dam can be overtopped thus flooding the downstream areas.

As far as the generated water waves are concerned, they may present very different shapes and dispersive features. Prins (1958), Wiegel et al. (1970) and Noda (1970) performed several physical experiments generating impulse waves by the falling of a solid block in a two dimensional wave flume. They concluded that, depending on the local water depth, the energy exchange between the landslide and the water, and the landslide volume, impact waves present different characteristics. Their experimental observation can be summarized by Figure 1.2, which presents a map of different wave types observed during impulse waves generation due to the vertical fall of a box (λ is the box width, d is the local water depth, $Fr = v/\sqrt{gd}$ is the dimensionless box falling velocity). The typical time series of water surface elevation at a given point are represented on the right part of Figure 1.2. Basically four types of impact waves were observed by these authors: (A) leading wave with oscillatory wave characteristics, (B–C) leading wave with solitary

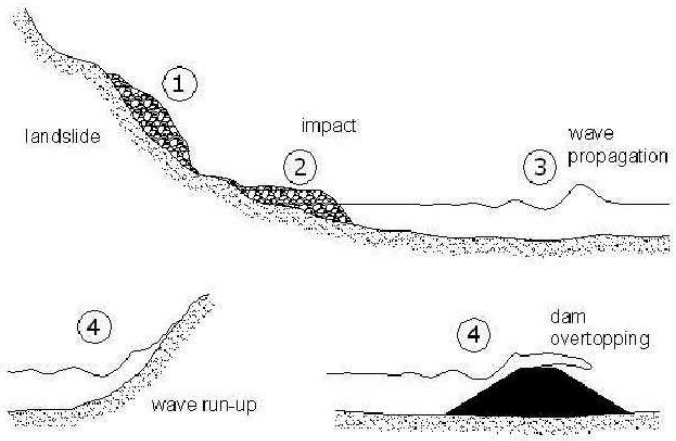

Figure 1.1: Principal phases in the phenomenon of subaerial landslide generated waves.

wave characteristics, followed by a trough connecting it with the dispersive wave pattern, (D–E) leading wave being a single wave with solitary wave characteristics, separated by the dispersive wave pattern, (F) solitary wave with complex form (bore in the first stage). As a general rule the generated waves type vary from (A) to (F) gradually as the values of λ/d and Fr increase. When the dimensions of the falling body are large in comparison to water depth, solitary waves are to be expected, vice versa a train of dispersive waves is likely to be generated in relatively deep water.

The tsunamis generation and propagation can be analyzed in the *near field* (in the vicinity of the impact area) or in the *far field* (where propagation takes place). The water wave field can be recognized to change from the *near field*, where the water motion is complex and three dimensional, presenting splashes and bores, to the *far field*, where the water motion is dominated by propagating water waves. In the definition of *near* or *far field*, some further considerations can be made. Considering the ratio between the volume of the landslide and that of the water body, where impulsive flows take place, three different cases can be recognized (see Figure 1.3): the first case (A), is the case of a large landslide falling into a small reservoir, the third case (C) contrary, is when a small landslide falls into a large reservoir or in the

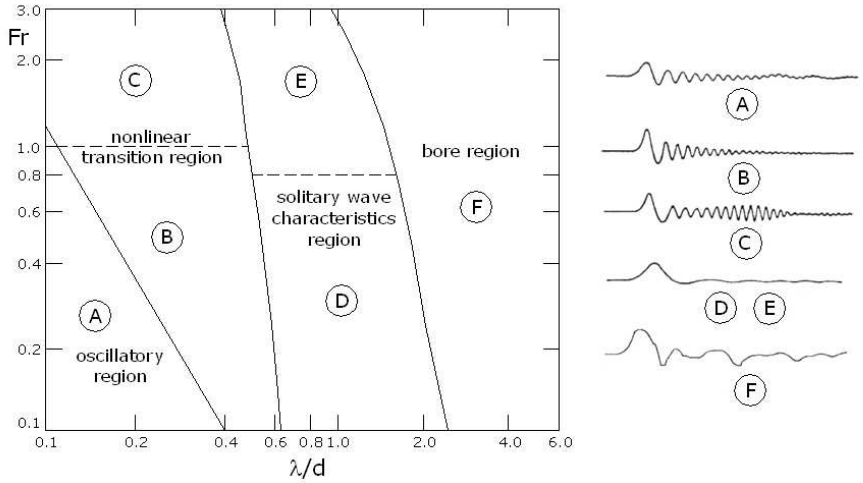

Figure 1.2: Different types of impulse waves defined as function of the landslide volume, represented by the dimensionless parameter λ/d, and the landslide velocity, represented by the Froud number Fr (picture taken from Noda, 1970).

open sea, and the second panel (B) of Figure 1.3 shows an intermediate case. The situation sketched in the panel A, is the limit of a case where the far field does not exist, that one on the panel C, shows a case where the near field is small compared to the far field, the intermediate situation (panel B) consist of near field and far field of comparable extents. So it is important to consider which could be the dominant aspects of the phenomenon before modeling subaerial landslide generated waves.

1.2 Aims and structure of the present work

In the recent past the research interest on tsunamis has risen enormously, due to the threat of the inundation consequences on coastal zone. Mathematical theory and physical model experiments have been implemented in order to get more insight about the physical processes and to plan defence strategies aimed to mitigate the effects of these events. The present work aims at developing a new numerical model and methodology to simulate the generation and propagation of tsunamis. The model is based on the mild

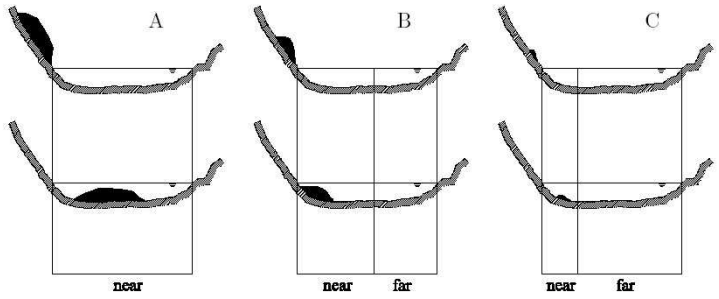

Figure 1.3: Three different main cases defined as a function of the ratio between the volume of the landslide and that of the water body.

slope equation (MSE hereinafter), originally developed by Berkhoff (1972), which is able to reproduce small amplitude transient waves, because is linear, and to properly simulate the full frequency dispersion of the waves. The numerical technique makes use of the Fourier Tranform (with respect to the time) of the wave equation in order to obtain an elliptic equation for each component of the wave spectrum, which are solved using a numerical finite element method. Solving the mild slope equation in the frequency domain potentially allows the solution of all the wave frequency components, which can be then superimposed, due to the linerity of the equations, to obtain the time domain solution.

The innovative feature of the model is in the computational procedure, more than in the model equations, which makes it suitable for the use in tsunami early warning system (TEWS). As it will be shown the model can be applied in real time. This is possible because the computational procedure is split into two parts. One is computationally expensive, and has to be carried out when preparing the system; the other one is very fast, and can be carried out in real time as the tsunami event takes place.

The present document is structured in 5 chapters. In the first one the topics and the aims of the work are already outlined. *Chapter 2* provides an overview of the mathematical water wave theories, with particular attention to those used to model tsunamis and to the recent works on this topic. In *Chapter 3* the model equations are derived and the numerical model is described. *Chapter 4* presents the model applications and shows the

model's validation for reproducing tsunamis generated by landslide. *Chapter 5* presents a model application to the Tyrrhenian Sea, in the Mediterranean Sea. There, at Stromboli island, as already mentioned, a tsunami event occured in December 2002. Stromboli is a still active volcano, and sometimes the most big eruptions are associated to landslides falling into the sea. The last chapter gives the conclusions and the final discussions of the present work.

Chapter 2

Tsunami wave modelling

In fluid mechanics the fluid is considered as a continuum; this allows all fluid properties to be described by mathematical functions that are continuous and differentiable. Thus modelling the fluids kinematics and dynamics, means applying the laws of conservation of mass and of momentum to a finite volume of fluid. Depending on the assumptions made in order to simplify the problem, different mathematical problem are obtained. The Navier-Stokes equations, within the continuity equation, represent a complete set of equations for fluid flows. Assuming that the fluid viscosity neglectable, i.e. away from the boundary layers and turbulence, it means that the fluid motion is irrotational (zero vorticity); in this case the Navier-Stokes equations reduce to the Euler equations. In this chapter the main irrotational water wave theories are outlined, and a literature review of the tsunami modelling is given.

2.1 Irrotational water waves theories

In general for the description of the water wave motion a system of reference as the one sketched in figure 2.1 is used, where x and y are the horizontal coordinates and z is the vertical one pointing upward. The plane x, y for $z = 0$ represents the still water free surface and the distance between this plane and the see bottom is defined by the water depth function $h\left(x, y, t\right)$. The fluid velocity and the fluid pressure inside the domain are defined respectively by the vector $\mathbf{v} = \{u, v, w\}$ and the scalar $p\left(x, y, z, t\right)$, while $\eta\left(x, y, t\right)$ defines the free water surface vertical displacement. Assuming an irrotational fluid, the

velocity vector field can be represented by a velocity potential $\phi(x, y, z, t)$, which is a scalar. The continuity equation for an incompressible fluid, in terms of velocity potential becomes the Laplace equation

$$\nabla_h^2 \phi + \phi_{zz} = 0 \qquad -h(x, y) < z < 0 \tag{2.1}$$

where ∇_h is the differential operator which means the divergence in the horizontal coordinates (x, y)

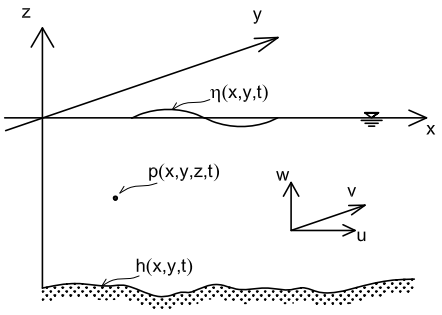

Figure 2.1: Reference sketch for the description of wave motion

The vectorial momentum equation, for an inviscid fluid (Euler equation), becomes the scalar Bernoulli equation in term of velocity potential

$$\phi_t + \frac{1}{2}\left(\phi_x^2 + \phi_y^2 + \phi_z^2\right) + \frac{p}{\rho} + gz = c(t) \qquad -h(x, y) \leq z \leq 0 \tag{2.2}$$

where $c(t)$ is an arbitrary function in the generalized Bernoulli equation. Hereinafter it is chosen to include $c(t)$ in ϕ_t, thus the right hand side of equation (2.2) can be put as zero. The kinematic boundary conditions allow the fluid particles to remain on that boundary. At the impermeable sea bottom $z = -h$ this is equivalent to assuming that the fluid velocity is parallel to the bottom at all points; at the free water surface $z = \eta$ means the fluid particles must follow the motion of the free surface

$$\phi_z + h_t + \nabla_h \phi \cdot \nabla_h h = 0 \qquad z = -h(x, y), \tag{2.3}$$

$$\phi_z - \eta_t - \nabla_h \phi \cdot \nabla_h \eta = 0 \qquad z = \eta(x, y, t) \tag{2.4}$$

At the free water surface a dynamic condition express that the external stresses on this boundary have to be balanced by equivalent internal stresses inside the fluid. For inviscid fluid the external stress is the atmospheric pressure acting on the boundary, which can be assumed to be zero, so the dynamic free surface boundary condition comes from the Bernoulli equation (2.2) imposing the pressure to be zero

$$\phi_t + \frac{1}{2}\left(\phi_x^2 + \phi_y^2 + \phi_z^2\right) + g\eta = 0 \qquad z = \eta\left(x, y, t\right) \tag{2.5}$$

The mathematical problem is rewritten here for the sake of clarity

$$\begin{cases} \nabla_h^2\phi + \phi_{zz} = 0 & -h\left(x,y\right) < z < 0 \\ \\ \phi_z + h_t + \nabla_h\phi \cdot \nabla_h h = 0 & z = -h\left(x,y\right) \\ \\ \phi_z - \eta_t - \nabla_h\phi \cdot \nabla_h\eta = 0 & z = \eta\left(x,y,t\right) \\ \\ \phi_t + \frac{1}{2}\left(\phi_x^2 + \phi_y^2 + \phi_z^2\right) + g\eta = 0 & z = \eta\left(x,y,t\right) \end{cases} \tag{2.6}$$

The problem defined as (2.6) can be formulated in an adimensional form, in order to estimate the relative order of magnitude of each term of the equation. The dimensionless problem, derived in details in the appendix A, results to be

$$\begin{cases} \nabla_h^2\phi + \frac{1}{\mu^2}\phi_{zz} = 0 & -h'\left(x,y\right) < z < 0 \\ \\ \frac{1}{\mu^2}\phi_z + \frac{1}{\epsilon}h_t + \nabla_h\phi \cdot \alpha = 0 & z = -h' \\ \\ \frac{1}{\mu^2}\phi_z - \eta_t - \epsilon\nabla_h\phi \cdot \nabla_h\eta = 0 & z = \epsilon\eta' \\ \\ \phi_t + \frac{1}{2}\epsilon\left(\phi_x^2 + \phi_y^2 + \frac{1}{\mu^2}\phi_z^2\right) + \eta = 0 & z = \epsilon\eta' \end{cases} \tag{2.7}$$

Problem (2.7) shows the presence of three dimensionless parameters

- $\mu = \frac{h}{L}$, the wave length parameter
- $\epsilon = \frac{a}{h}$, the amplitude parameter
- $\alpha = \nabla_h h$, the bottom slope

The water waves models can be classified depending on which restrictions are made on these dimensionless parameters; or, formulated in a different way, it can be said that under different conditions, different theories can be applied. With reference to the wave length parameter μ, the following conditions are considered

- $\mu < \frac{1}{20}$, shallow water or long waves conditions
- $\frac{1}{20} < \mu < \frac{1}{2}$, intermediate water conditions
- $\mu > \frac{1}{2}$, deep water or short waves conditions

while the amplitude parameter ϵ governs the linearity of the waves equations

- small values of ϵ implies linear equations
- large values of ϵ implies nonlinear equations

The Stokes waves theory, first derived by Stokes (1847), emerges from the dimensionless problem assuming to be in intermediate to deep water relative to the characteristic horizontal scale L. This means assuming $\mu = O(1)$. The Stokes wave theory is valid for small amplitude waves, i.e. small values of ϵ, and is derived following a perturbation expansion approach: the solution for the fluid velocity potential, ϕ, the free surface elevation, η and the pressure, p are expanded in a power series of ϵ. Then they are inserted back into the equations (2.7), which are solved at each order of the power series. The first order of approximation is relative to the power zero of ϵ, and is the case of linear Stokes waves equations. The mathematical problem becomes in dimensional variables

$$\begin{cases} \nabla_h^2 \phi + \phi_{zz} = 0 & -h(x,y) < z < 0 \\ \phi_z + h_t + \nabla_h \phi \cdot \nabla_h h = 0 & z = -h(x,y) \\ \phi_z - \eta_t = 0 & z = 0 \\ \phi_t + g\eta = 0 & z = 0 \end{cases} \tag{2.8}$$

Considering the next power of ϵ (i.e. larger values of the ratio a/h) the theory becomes nonlinear. The most evident effect of the second

order approximation is the asymmetry of the wave profile, which presents longer and smaller trough and peaked crests. The solution of the linear mathematical problem (2.8) gives the fluid velocity field $\phi(x, y, z, t)$ and the water surface elevation $\eta(x, y, t)$, and brings to the following relation, written in dimensional variables

$$\omega^2 = gk \tanh(kh) \tag{2.9}$$

which is named dispersion relation and essentially specifies the correlation between ω and k, which are respectively the angular frequency and the wave number, defined as $\omega = \frac{2\pi}{T}$ and $L = \frac{2\pi}{L}$, where T and L are respectively the wave period and the wave length. Since the wave celerity c is defined as $c = L/T = \omega/k$, equation (2.9) can be written as

$$c^2 = \frac{g}{k} \tanh(kh) \tag{2.10}$$

which gives the values of the phase velocity c for a given water depth and wave length. This relation inidcates that each wave travels with an appropriate velocity depending on its frequency. In particular longer waves travel faster than shorter ones, thus an irregular wave packet during its propagation evolves in a wave train with the longest waves proceeding and a tail of shorter waves following. This explains the name of dispersion relation, in the meaning that waves are dispersive in frequency.

In the region near the shore the water depth becomes so small that the incident wind generated waves are much longer than the water depth. This is the shallow water regions and these waves are termed as long waves. Mathematically it means that the wave field equations are approximated by assuming the wave length parameter to be small, $\mu << 1$. The shallow water theories describe the fluid motion for the long waves and are valid in the limit of $\mu < 1/20$. A consequence of imposing the limit of $\mu \to 0$ is that all waves travel with the same celerity, which does not depend on the frequency (i.e. the period). In this limit equation (2.10) provides $c = \sqrt{gh}$, therefore the long waves are called non-dispersive because, each frequency component travels at the same velocity thus do not evolve in a wave train but maintain the same shape.

The long wave theory is derived again from the dimensionless problem (2.7), and the solution ϕ is now assumed to be a power series of the small parameter μ. This procedure provides one system of equations for each order

of the power series. Shallow water theory is the approximation resulting from truncating the process at the lowest order possible.

Three different theories arise by considering the relative magnitude of the both small parameters ϵ and μ^2

- $\epsilon << O(\mu^2)$
- $\epsilon = O(\mu^2)$
- $\epsilon >> O(\mu^2)$

The first and the last cases are well described respectively by the linear shallow water waves equations (LSWE) and the nonlinear shallow water waves equations (NLSWE). When $\epsilon = O(\mu^2)$ nonlinear weakly dispersive equations describe the wave motion. These equations lead to the so called Boussinesq type equation (BTE).

For each theory, by substituting the series expansion of the potential in the kinematic and dynamic free surface boundary conditions, respectively a mass and a momentum equilibrium equations are achieved valid for a column of water. Thus the original mathematical problem is simplified to a set of two equations in the two dependent variables η and $\mathbf{v}$, which in the case of $\epsilon >> O(\mu^2)$ are

$$\begin{aligned} &\eta_t + \nabla_h \left[\mathbf{v}\left(\epsilon\eta + h_0\right)\right] = 0 \\ &\mathbf{v}_t + \epsilon\mathbf{v}\nabla_h\mathbf{v} + g\nabla_h\eta = 0 \end{aligned} \tag{2.11}$$

by neglecting the ϵ order terms, i.e. $\epsilon << O(\mu^2)$ the linear shallow water equations are achieved

$$\begin{aligned} &\eta_t + \nabla_h \left(\mathbf{v}h_0\right) = 0 \\ &\mathbf{v}_t + g\nabla_h\eta = 0 \end{aligned} \tag{2.12}$$

The Boussinesq equations include the lowest order effects of frequency dispersion and nonlinearity. They can thus account for the transfer of energy between different frequency components, the shape of individual waves changes, and the evolution of the wave group propagating in varying water depth. Different BTE have been implemented in order to extend the range of applicability to deeper water, by improving the dispersion characteristics

of the equations. Nwogu (1993) derived a form of the BTE which uses the velocity at an arbitrary distance from the still water level instead of the commonly used depth-averaged velocity. His equations reduce to

$$\begin{aligned} &\eta_t + h\nabla_h \mathbf{v} + \alpha_1 h^3 \nabla_h^2 (\nabla_h \mathbf{v}) = 0 \\ &\mathbf{v}_t + g\nabla_h \eta + \alpha h^2 \nabla_h^2 \mathbf{v}_t = 0 \end{aligned} \tag{2.13}$$

where $\mathbf{v}$ is the velocity at the water depth $z = z_\alpha$, and $\alpha_1 = \alpha + \frac{1}{3}$, with α determined by

$$\alpha = \frac{z_\alpha}{h}\left(\frac{1}{2}\frac{z_\alpha}{h} + 1\right); \qquad \frac{z_\alpha}{h} = -0.530. \tag{2.14}$$

The first order Stokes equations are widely used to reproduce wind generated waves in deep water. As the waves approach the coast, the assumption of $\epsilon << 1$ is no more valid, the higher order Stokes equations have to be used. Tsunamis are considered as extremely long, single waves able of devastating the coast, thus the long wave theories result suitable in the tsunami wave modeling. In the next section are shown some relevant works on the mathematical modeling of tsunami.

2.2 Tsunami waves modeling. Literature review

Tsunami are generally regarded as long waves in comparison with the wind generated waves. Thus traditionally mathematical models based on the Nonlinear Shallow Waters Equations (NLSWE) (2.11) were used to simulate the wave field. Other research works reveal that linear shallow water theory is also suitable to model tsunami propagation, in the regions where the wave amplitude is much smaller than the water depth, i.e. the ocean zone before the shoaling effects. However in the recent past it has become well accepted that although tsunami are generated with a shape of solitary long crested waves, when they propagate over a deep sea/ocean, evolve into a train of waves, due to the frequency dispersion effects, thus the shallow water approximation could not be able to reproduce this aspect.

Kulikov et al. (2005) have demonstrated, on the basis of satellite recordings of the December 26, 2004 Indian Ocean tsunamis, that the waves generated by such a huge earthquake were strongly frequency-dispersive.

In the work of Tadepalli & Synolakis (1996) it also appears that some important features of the tsunamis propagation, such as the fact that the first wave has a trough traveling in front of the crest, can be predicted by using model equations that take into account the frequency-dispersion. They proposed a model which assumes that the solitary wave like tsunami have the shape of leading-depression N-wave. In the far propagation field they solve the Korteweg-de Vries equations, while in the near shore field they use LSWE. Intensification of the height of tsunamis waves can also be induced by frequency dispersion, as suggested by Mirchin & Pelinovsky (2001).

The NLSWE however, although able of taking into account amplitude-dispersion (i.e. the nonlinear effects) of the waves, cannot reproduce the frequency-dispersion, which as mentioned before may be of relevant importance. When studying the propagation of these waves over large geographical areas it is common that the height of tsunamis is several order of magnitudes smaller than the water depth. The typical wave height of a large, destructive tsunamis is of 1 m, while the water depth over which it propagates may be of 100, 1000 m. The steepness of the waves is also extremely small, since the length is of the order of the kilometers. This suggests that nonlinear effects may be neglected or at least may be of secondary importance in comparison to the proper reproduction of the frequency-dispersion. It is worth to mention however that the above considerations mostly apply for the far field and not in proximity of the coast (i.e. in very shallow waters), where the nonlinear effects become important.

In the last decades the Boussinesq-type equations (Peregrine, 1967; Madsen et al, 1991; Wei & Kirby, 1995; Nwogu, 1993) have therefore become the most suitable model for the tsunamis simulation. These equations allow the reproduction of wave nonlinearity, relevant in the coastal shallow areas, but they take into account of a weakly frequency dispersion of water waves, thus being able to simulate its propagation a bit further in the deep water conditions. Several versions of this type of models are available. The complexity of the model equations (and therefore the computational costs), however grows with the increased ability of the models of reproducing the nonlinear and the frequency-dispersive effects.

Watts and Grilli carried out research studies on tsunami generated by landslides (Watts et al., 2003; Grilli et al., 2005). They build up GEOWAVE which is a comprehensive tsunami simulation model formed by combining the Tsunami Open and Progressive Initial Conditions Sytem (TOPICS), for the wave maker and tsunami generation, with the FUNWAVE model

for the tsunami propagation and inundation. TOPICS uses curve fits of numerical results from a fully nonliner potential flow model to provide approximate landslide tsunami sources for tsunami propagation models, based on marine geology data and interpretations. While the simulation of tsunami propagation and inundation is carried out with the long wave propagation model FUNWAVE, which is based on fully nonlinear Boussinesq equations, with an extended dispersion equation, in the sense that ist matches the linear dispersion relationship for deep water waves. They incuded a breaker model in FUNWAVE in order to simulate inundation of dry land. In their work, Grilli et al. (2005) performed numerical and experimental models of tsunami generated by landslide slumps and slides.

Not taking into account the wave frequency dispersion can be even worse in the cases of landslide generated tsunamis, because the landslide, moving further in deeper water, still generates waves, which are generally shorter relatively to the water depth. Lynett & Liu (2002) developed a mathematical model to describe the generation and propagation of submarine landslide generated water waves. Their model consist of a depth integrated continuity equation and momentum equations which include full nonlinear, but weakly frequency dispersion effects. They pointed out two main differences between the tsunami generation mechanism of a submarine landslide and a submarine earthquake. First the duration of a landslide is much longer, indeed the time history of the seafloor movement will affect the characteristic of the generated wave, and can not be considered just as an initial impulsive condition. Second, the typical wavelength of the tsunami generated by landslide is shorter, therefore, the frequency dispersion could be important even in the wave generation region. In their model equations the ground movement is the forcing function, they have therefore developed a new version of the BTE, starting from bottom boundary conditions that take into account the seafloor deformations given by the landslide. They have obtained model equations that naturally incorporate the effect of the moving bottom and are able to satisfactorily reproduce the frequency dispersion of the waves. They also suggest that the effects of the moving bottom on the surface waves depend on the wave frequency.

Sammarco & Renzi (2008) developed an analytical two-horizontal dimension model to analyze the different physical features of landslide-induced tsunamis along a straight coast. Their model is based on the forced linear long-wave equation of motion (LSWE). In particular they noticed that after a short transient immediately following the landslide generation, the

wave motion starts to be trapped at the shoreline and finally only transient long-shore traveling edge waves are present. Longer waves travel faster and are followed by a tail of shorter waves, while new crests are created. Unlike transient waves generated and propagating in water of constant depth, for landslide-induced tsunamis along a sloping beach the larger waves are not in the front of the wave train, but are shifted toward the middle of it. Experimental comparison shows the validity of the model in reproducing the physical behavior of the system. Their close analysis on the trapped waves of landslide tsunamis along a straight beach is in the following compared with the model presented in this document.

The MSE has been originally developed by Berkhoff (1972) for purely harmonic waves, and due to its elliptic nature it was able of providing the steady-state wave field. The MSE is a depth integrated equation that, whitin appropriate boundary conditions, describes the waves propagation over mildly slope sea bottom. It is derived from the adimensional problem (2.7) by assuming $\epsilon << 1$ and $\alpha << 1$, as it will be shown in section 3.1.1. Copeland (1985) starting from the elliptic MSE obtained an hyperbolic time-dependent version of the equations, which however was used to achieve the steady-state wave field induced by periodic waves (see also Madsen & Larsen, 1987). Also Smith & Spring (1975) and Radder & Dingemans (1985) developed hyperbolic time-dependent MSE. Kubo et al. (1992) and Kirby et al. (1992) studied the applicability of the time-dependent equations to random waves. However they concluded that only very narrow banded frequency wave spectra are properly reproduced by the hyperbolic versions of the MSE, since some coefficients of the equations are calculated using the frequency of the carrier wave. Lee et al. (2006; 2003) have further enhanced the ability of these models also including the effect of rapidly varying bottom.

None of the above mentioned models seems able of dealing with broad banded spectrum wave field, such as that resulting for tsunamis. Kirby et al. (1992) separated the whole wave spectrum into several narrow bands and for each of these solved the time-dependent MSE.

It is worth to mention here few research studies on tsunami generation and propagation carried out using physical models. Between the most recent works it can be cited the one of Enet and Grilli (2007). They performed large three dimensional laboratory experiments to study tsunamis generated by rigid underwater landslides, with the main purpose of both gain insight into landslide tsunami generation processes and provide data for subsequent validation of a three dimensional numerical model. The experiments were

carried out in a wave tank of the Ocean Engineering Department at the University of Rhode Island, USA. In their model the landslide is reproduced with a smooth and streamlined rigid body which slides down a plane slope, starting from different underwater positions. They have carried out a detailed study of the law of landslide motion and relative discussions about the generated waves features.

With regard to the landslide generated tsunami, the works of Di Risio et al. (2009a; 2009b) need to be mentioned even because were used in the present work to validate the numerical model. The paper of Di Risio et al. (2009a) describes three dimensional laboratory experiments carried out at the Environmental and Maritime Hydraulic Laboratory (LIAM) of the University of L'Aquila, Italy, and reproduce a rigid landslide body sliding on a plane slope. The paper of Di Risio et al. (2009b) describes other three dimensional experiments which simulate an equal landslide body sliding down the flank of a conical island, builded in the middel of a large wave tank. This physical model is built at the Research and Experimentation Laboratory for Coastal Defence (LIC), of the Technical University of Bari, Italy. More details about both physical models are given in sections 4.4 and 4.5 where their results are used to validate the numerical model.

Chapter 3

Description of the numerical model

The numerical model here described is based on the linearized mild slope equation (MSE) and is able of reproducing the full frequency-dispersion of small amplitude tsunamis, which makes it an attractive tool for the simulation of these waves in the far field. The main difference with BTE models is not in the results, which for the typical properties of the tsunamis may be of the same order of accuracy, but mostly in the computational procedure that, as shown in the following, makes it suitable for the use in tsunamis early warning systems. The model presented in this work directly uses the Fourier Transform of the time-dependent MSE and solves the resulting equations in the frequency domain. The problem therefore reduces to the solution of the traditional elliptic MSE and the time series of the surface elevation is then recovered by means of the Inverse Fourier Transform. This procedure guarantees accurate reproduction of the frequency-dispersion, since each component of the wave field is modeled using a dedicated elliptic equation. The MSE is a depth integrated equation, thus solves the wave field assuming that the kinematic (fluid velocities) and the dynamic (fluid pressures) features vary along the water depth according to a predefined function. The depth integrated models represent a good compromise between accuracy of the results and computational costs.

The present chapter contains one section which derives the model equations, i.e. the MSE and the boundary conditions, in the frequency domain. Particular focus is given on how the waves are generated inside the domain, which can be achieved by imposing a wave maker boundary

condition or a forcing source term in the field equation. Different model applications are described in section 3.2, which mostly depend on how the waves are numerically generated and on which would be the purpose of the modeling: gain insight on the tsunami propagation process or predict tsunami wave height and time of arrival for a early warning system. In the last section a further application of the model is presented, which makes use of the solution of the parabolic approximation of the MSE, matched with its elliptic version.

3.1 Model equations derivation

3.1.1 Field equation

As starting point the linearized (small amplitude) water wave equations for an incompressible irrotational fluid on an uneven bottom are taken, i.e. equations already derived in the mathematical problem (2.8)

$$\nabla_h^2 \phi + \phi_{zz} = 0 \qquad -h(x,y) \leq z \leq 0 \tag{3.1}$$

$$\phi_t + g\eta = 0 \qquad z = 0 \tag{3.2}$$

$$\eta_t - \phi_z = 0 \qquad z = 0 \tag{3.3}$$

$$\phi_z + \nabla_h \phi \cdot \nabla_h h = 0 \qquad z = -h(x,y), \tag{3.4}$$

where again, $\phi(x,y,z,t)$ is the velocity potential in the fluid, $\eta(x,y,t)$ is the instantaneous elevation of the free surface, $h(x,y)$ is the water depth and g is the gravity acceleration, while ∇_h is the differential operator which means the divergence in the horizontal coordinates (x,y). All these variables are real and scalar.

The dynamic and kinematic boundary conditions at the free surface, equations (3.2) and (3.3), can be incorporated in a single equation

$$\phi_z + \frac{1}{g}\phi_{tt} = 0 \qquad z = 0 \tag{3.5}$$

The solution of the given problem is assumed to be of the form

$$\phi(x,y,z,t) = \varphi(x,y,t)\, f(z) \tag{3.6}$$

where $\varphi(x, y, t)$ is the velocity potential at the undisturbed free water surface $z = 0$ and $f(z)$ is a function that describes how the kinematic field varies along the water depth. Note that φ can be complex and includes the effects of reflected waves, while f can be chosen as that resulting from the linear wave theory valid for harmonic waves propagating in constant depth, which however still holds in the case of mildly sloping bottom, i.e.

$$f(z) = \frac{cosh\left[k\left(h+z\right)\right]}{cosh\left(kh\right)} \tag{3.7}$$

where k is the wave number.
From the assumption (3.6) it comes that

$$\phi_z = \varphi f_z = k\varphi \frac{sinh\left[k\left(h+z\right)\right]}{cosh\left(kh\right)} \tag{3.8}$$

and

$$\phi_{zz} = k^2\varphi \frac{cosh\left[k\left(h+z\right)\right]}{cosh\left(kh\right)} = k^2\phi \tag{3.9}$$

therefore the Laplace equation (3.1) can be written as

$$\nabla_h^2\phi + k^2\phi = 0 \tag{3.10}$$

The following considerations are made:

$$f(z) = 1 \qquad at \quad z = 0 \tag{3.11}$$

$$f_z = 0 \qquad at \quad z = -h; \tag{3.12}$$

$$f_z = ktanh\left(kh\right) = \frac{\omega^2}{g} \qquad at \quad z = 0; \tag{3.13}$$

In order to depth integrate the field equation (Laplace equation 3.1), here it is made use of the Green's Theorem, which states

$$\int_a^b \left(\Phi_1\nabla^2\Phi_2 - \Phi_2\nabla^2\Phi_1\right)dx = \left[\Phi_1\nabla\Phi_2 - \Phi_2\nabla\Phi_1\right]_a^b \tag{3.14}$$

where Φ_1 and Φ_2 are generic functions of x. For the present purposes it is assumed $x = z$, $\Phi_1 = f(z)$ and $\Phi_2 = \phi(x, y, z, t)$, therefore

$$\int_{-h}^{0}\left(f\frac{\partial^2\phi}{\partial z^2}-\phi\frac{\partial^2 f}{\partial z^2}\right)dz=\left[f\frac{\partial\phi}{\partial z}-\phi\frac{\partial f}{\partial z}\right]_0-\left[f\frac{\partial\phi}{\partial z}-\phi\frac{\partial f}{\partial z}\right]_{-h} \tag{3.15}$$

Substituting the Laplace equation (3.1) in the first term at the left hand side (LHS), and the boundary conditions at $z=0$ and $z=-h$ (3.5 and 3.4) and using equations (3.13, 3.12), in the right hand side (RHS) terms, then, after changing the sign, equation (3.15) becomes

$$\int_{-h}^{0}\Big(f\nabla_h^2\phi+k^2f\phi\Big)dz=\frac{1}{g}\varphi_{tt}+\varphi\frac{\omega^2}{g}-\left[f\nabla_h h\nabla_h\phi\right]_{-h} \tag{3.16}$$

the LHS can be seen as the integration over the depth of the field equation. Considering that

$$\nabla_h\phi=\nabla_h\left(\varphi f\right)=f\nabla_h\varphi+\varphi\nabla_h f \tag{3.17}$$

and

$$\nabla_h^2\phi=f\nabla_h^2\varphi+2\nabla_h\varphi\nabla_h f+\varphi\nabla_h^2 f \tag{3.18}$$

using the expression (3.17) for the last term of the RHS and expression (3.18) for the first term of the LHS, equation (3.16) becomes

$$\begin{array}{l}\int_{-h}^{0}\left(f^2\nabla_h^2\varphi+2f\nabla_h f\nabla_h\varphi+f\varphi\nabla_h^2 f+k^2f^2\varphi\right)dz=\\ \frac{1}{g}\left(\varphi_{tt}+\omega^2\varphi\right)-\left[f\nabla_h h\left(f\nabla_h\varphi+\varphi\nabla_h f\right)\right]_{-h}\end{array} \tag{3.19}$$

Now the first two terms of the LHS of equation (3.19) can be written as

$$\nabla_h\left(f^2\nabla_h\varphi\right)=f^2\nabla_h^2\varphi+2f\nabla_h f\nabla_h\varphi \tag{3.20}$$

Reordering equation (3.19) it comes that

$$\begin{array}{l}\int_{-h}^{0}\nabla_h\left(f^2\nabla_h\varphi\right)dz+\left[\nabla_h h f^2\nabla_h\varphi\right]_{-h}+\varphi k^2\int_{-h}^{0}f^2dz=\\ -\int_{-h}^{0}\varphi f\nabla_h^2 f dz-\varphi\nabla_h h\left[f\nabla_h f\right]_{-h}+\frac{1}{g}\left(\varphi_{tt}+\omega^2\varphi\right)\end{array} \tag{3.21}$$

For the first two terms on the LHS it can be applied the Leibniz's rule, therefore the equation (3.21) can be written as

$$\begin{array}{l}\nabla_h\left(\int_{-h}^{0}f^2\nabla_h\varphi dz\right)+\varphi k^2\int_{-h}^{0}f^2dz-\frac{1}{g}\left(\varphi_{tt}+\omega^2\varphi\right)=\\ -\varphi\int_{-h}^{0}f\nabla_h^2 f dz-\varphi\nabla_h h\left[f\nabla_h f\right]_{-h}\end{array} \tag{3.22}$$

Knowing that

$$\int_{-h}^{0} f^2 dz = \frac{cc_g}{g} \tag{3.23}$$

where c and c_g are respectively the phase and group celerity. By multiplying equation (3.44) for g it results

$$\begin{array}{l} \nabla_h \left(cc_g \nabla_h \varphi\right) + \varphi k^2 cc_g - \varphi_{tt} - \omega^2 \varphi = \\ -g\varphi\{\int_{-h}^{0} f\nabla_h^2 f dz + \nabla_h h \left[f\nabla_h f\right]_{-h}\} \end{array} \tag{3.24}$$

the RHS terms can be shown to be $O\left(\left(\nabla_h h\right)^2, \nabla_h^2 h\right)$. Therefore if the mild-slope assumption is introduced, $\nabla_h h \ll kh$ corresponding to $\nabla_h h L/h \ll 1$ it can be argued that the $\left(\nabla_h h\right)^2$-terms $\ll$ LHS terms. Similarly, $\nabla_h^2 h \ll \nabla_h h$, which is a natural additional assumption because $\nabla_h^2 h = O\left(\nabla_h h\right)$ can only occur over short distances without changing $O\left(\nabla_h h\right)$. This means that the RHS terms are $\ll$ of all the others terms, we therefore get

$$\varphi_{tt} - \nabla_h \left(cc_g \nabla_h \varphi\right) + \left(\omega^2 - k^2 cc_g\right) \varphi = 0 \tag{3.25}$$

which is the **hyperbolic version of the MSE** in terms of fluid velocity potential and is usually referred to as the 'time-dependent mild-slope equation', allowing the simulation in the time-domain of the wave propagation. To obtain the MSE in terms of the free surface elevation η, equation (3.25) needs to be differentiated with respect to time.

$$\varphi_{ttt} - \nabla_h \left(cc_g \nabla_h \varphi_t\right) + \left(\omega^2 - k^2 cc_g\right) \varphi_t = 0 \tag{3.26}$$

and then use the dynamic boundary condition at the free surface (3.2)

$$\eta = -\frac{1}{g}\varphi_t \tag{3.27}$$

from which we obtain that $\varphi_t = -g\eta$ and $\varphi_{tt} = -g\eta_t$, those expressions can be substituted into equation (3.26) to get, after dividing by g

$$-\eta_{tt} + \nabla_h \left(cc_g \nabla_h \eta\right) - \left(\omega^2 - k^2 cc_g\right) \eta = 0 \tag{3.28}$$

which is the hyperbolic version of the MSE in terms of free surface elevation.

As previously said the time dependent MSE is not able to reproduce broad banded spectra sea state, due to the fact that equation (3.28) contains some coefficients which have to be calculated by assuming a dominant frequency of

the wave spectrum, thus the validity of the resulting equation would be only for narrow frequency-spectra seas (see the recent work by Lee et al., 2006 and references therein). By employing the spectral approach, the model can on the contrary cover a broad spectrum wave field, typical of tsunamis, since for each wave frequency a dedicated elliptical equation is solved.

The **elliptic version of the MSE** can be obtained by taking the Fourier Transform of equation (3.28), then it comes

$$\nabla_h \left(cc_g \nabla_h N \right) + k^2 cc_g N = 0 \tag{3.29}$$

where $N(x, y, \omega)$ is the Fourier Transform of $\eta(x, y, t)$. Alternatively by assuming a time harmonic wave motion, thus the water free surface elevation assumes the form of

$$\eta(x, y, t) = a(x, y) \cdot e^{i\omega t} \tag{3.30}$$

and obtaining the same equation of (3.29)

$$\nabla_h \left(cc_g \nabla_h a \right) + k^2 cc_g a = 0 \tag{3.31}$$

Equation (3.29) (or (3.31)) is the elliptic MSE as derived by Berkhoff (1972). It is commonly used for the reproduction of harmonic waves, and it represents a formidable tool for studying the propagation of small amplitude waves into harbors and over coastal areas (Zhao et al., 2001). However it is to be kept in mind that several (potentially infinite) values of ω are to be considered and therefore many equations like (3.29) need to be solved to obtain the final result in the frequency domain. Once the equations (3.29) are solved with the appropriate boundary conditions (discussed later) for each frequency ω, the result in the time domain can be achieved by taking the Inverse Fourier Transform of $N(x, y, \omega)$ to obtain $\eta(x, y, t)$.

3.1.2 Boundary conditions

Boundary conditions used in this model are the fully reflective conditions at solid boundaries, the radiation condition, which allows the waves to freely exit the domain, and the wave-maker boundary condition.

The full-reflection boundary condition can be expressed by imposing the fluid velocity in the direction orthogonal to the boundary to be zero. By using the kinematic free surface boundary equation (3.3) it follows that the

derivative of the Fourier Transform of the free surface elevation η along the normal to the reflective boundary should be zero (see Mei, 1983):

$$N_n = 0. \tag{3.32}$$

The radiation boundary condition can be obtained by using a mathematical formulation that allows the waves that propagate toward the open boundaries to freely exit the computational domain. This condition can be easily formulated for progressive outgoing waves (Sommerfeld, 1964; Van Dongeren & Svendsen, 1997)

$$\eta_t + \frac{c}{cos\,(\theta_n)}\eta_n = 0 \tag{3.33}$$

where θ_n is the angle the wave direction forms with the outgoing normal to the considered boundary.

The Fourier Transform of equation (3.33) provides the radiation condition in the frequency domain (see Beltrami et al., 2001; Steward & Panchang, 2000)

$$N_n + ikcos\,(\theta_n)N = 0. \tag{3.34}$$

Please note that the equation (3.34) is nonlinear in the sense that θ_n is not known a priori and depends on the solution itself. Iterative techniques can therefore be applied or a reasonable estimate of this parameter can be used to solve the indeterminacy.

The waves generation in the numerical domain can be modeled with two different approaches: by means of a wave-maker boundary condition or by means of a source term included in the field equation. The latter approach is discussed in the next section 3.1.3. A wave-maker boundary condition can be seen as a wave paddle used in physical models (although here evanescent modes are not reproduced) and can be applied when the wave generation mechanism occurs close to a boundary of the numerical domain. The wave-maker boundary can be 'open' in the sense that generates the waves inside the domain and even allows the waves to exit the domain through it, i.e. the vertical section of an harbor opening, modeling the wave field inside the harbor. Otherwise the wave-maker boundary can be 'closed' thus reflects the incoming waves. The latter is the case of the wave field generated by an aerial landslide entering into the sea water when it is known the point of the impact.

The wave-maker boundary condition is conveniently formulated in terms of the velocity potential at $z = 0$ as follows

$$\varphi_n = u^I, \qquad z = 0, \tag{3.35}$$

where u^I is the velocity at $z = 0$ of the desired wave field orthogonal to the wave-maker boundary.

In order to obtain a mathematical expression involving η and consequently N we make use of the dynamic boundary condition at the free surface (3.2) which if transformed in the frequency domain results as follows

$$i\omega\Phi = -gN, \tag{3.36}$$

providing the usual relationship between Φ and N:

$$\Phi = -\frac{g}{i\omega}N \tag{3.37}$$

which allows rewriting of the wave-maker condition as

$$N_n = -\frac{i\omega}{g}U^I \tag{3.38}$$

being U^I the Fourier Transform of the desired time series of velocity at $z = 0$. It is worth to remind that the proposed wave-maker condition is used to specify the fluid velocity at $z = 0$, and that the velocity field for $-h < z < 0$ is assumed to vary as the function f. Evanescent modes are therefore not included in this formulation.

3.1.3 Waves generation

When the numerical domain entirely includes the wave generation area, this can be modeled by adding a source term in the field equation. In that case the right hand side of equation (3.29) is different from zero.

Here it is demonstrated how the MSE is modified in order to incorporate the effects of the movements of the bottom, such those occurring during earthquakes and submerged landslides. It is assumed that the water depth function $h\,(x, y, t)$ varies also with the time. Thus the kinematic boundary condition at the bottom results to be

$$\phi_z + h_t + \nabla_h\phi \cdot \nabla_h h = 0 \qquad z = -h \tag{3.39}$$

The Laplace equation within the free surface boundary conditions and the so modified bottom boundary condition, represent a problem as that formulated in the section 3.1.1. If the same procedure of depth integration is followed, it will appear an extra term. From the Green Theorem it results

$$\int_{-h}^{0}\left(f\frac{\partial^2\phi}{\partial z^2}-\phi\frac{\partial^2 f}{\partial z^2}\right)dz=\left[f\frac{\partial\phi}{\partial z}-\phi\frac{\partial f}{\partial z}\right]_0-\left[f\frac{\partial\phi}{\partial z}-\phi\frac{\partial f}{\partial z}\right]_{-h} \tag{3.40}$$

which, using the modified boundary conditions, now becomes

$$\int_{-h}^{0}\Big(f\nabla_h^2\phi+k^2f\phi\Big)dz=\frac{1}{g}\varphi_{tt}+\varphi\frac{\omega^2}{g}-[fh_t]_{-h}-[f\nabla_h h\nabla_h\phi]_{-h} \tag{3.41}$$

Operating the same step used to achieve equation (3.19) in this case it results

$$\begin{array}{l}\int_{-h}^{0}\left(f^2\nabla_h^2\varphi+2f\nabla_h f\nabla_h\varphi+f\varphi\nabla_h^2 f+k^2f^2\varphi\right)dz=\\ \frac{1}{g}\left(\varphi_{tt}+\omega^2\varphi\right)-\frac{1}{cosh(kh)}h_t-\left[f\nabla_h h\left(f\nabla_h\varphi+\varphi\nabla_h f\right)\right]_{-h}\end{array} \tag{3.42}$$

Now incorporating the first two terms of the LHS of equation (3.42) follows

$$\begin{array}{l}\int_{-h}^{0}\nabla_h\left(f^2\nabla_h\varphi\right)dz+\left[\nabla_h h f^2\nabla_h\varphi\right]_{-h}+\varphi k^2\int_{-h}^{0}f^2dz=\\ -\int_{-h}^{0}\varphi f\nabla_h^2 f dz-\frac{1}{cosh(kh)}h_t-\varphi\nabla_h h\left[f\nabla_h f\right]_{-h}+\frac{1}{g}\left(\varphi_{tt}+\omega^2\varphi\right)\end{array} \tag{3.43}$$

Applying the Leibniz's rule for the first two terms on the LHS and knowing that

$$\int_{-h}^{0}f^2dz=\frac{cc_g}{g} \tag{3.44}$$

it results

$$\begin{array}{l}\nabla_h\left(cc_g\nabla_h\varphi\right)+\varphi k^2cc_g-\varphi_{tt}-\omega^2\varphi=\\ -h_t\frac{g}{cosh(kh)}-g\varphi\{\int_{-h}^{0}f\nabla_h^2 f dz+\nabla_h h\left[f\nabla_h f\right]_{-h}\}\end{array} \tag{3.45}$$

for the same assumptions of being on mild slope sea bottom ($\nabla_h h=\alpha<<1$), the following MSE is achieved

$$\varphi_{tt} - \nabla_h \left(cc_g \nabla_h \varphi\right) + \left(\omega^2 - k^2 cc_g\right) \varphi = -\frac{g}{cosh\left(kh\right)} h_t \tag{3.46}$$

which again in terms of water free surface becomes

$$-\eta_{tt} + \nabla_h \left(cc_g \nabla_h \eta\right) - \left(\omega^2 - k^2 cc_g\right) \eta = -\frac{1}{cosh\left(kh\right)} h_{tt} \tag{3.47}$$

and in the frequency domain becomes

$$\nabla_h \left(cc_g \nabla_h N\right) + k^2 cc_g N = -\frac{1}{cosh\left(kh\right)} fft\left(h_{tt}\right) \tag{3.48}$$

Equation (3.48) is an elliptic equation, written in terms of the free surface elevation in the frequency domain, with a forcing term which accounts for the movements of the sea floor.

3.2 Model applications

The model applications depend on how the waves are numerically generated. Two alternative approaches have been already discussed. The first approach makes use of the wave-maker boundary conditions, the second one is based on the source term in the model equation. Both these approaches can be used following a 'direct' or an 'indirect' procedure. The 'direct' one is applicable when the movement of the bottom is known, or when the properties of the waves to be generated are known at the wave-maker boundary. In this case from the proper time series of $h\left(x, y, t\right)$, and its time derivatives, it can be easily calculated by means of the discrete Fourier Transform, the transformed variable $fft\left(h_{tt}\right)$ to be used into the equation (3.48). Equivalently if the fluid velocity at $z = 0$ is known at the wave-maker it can be directly used into equation (3.38).

The 'indirect' procedure is convenient when the surface elevation time series is known at some points of the computational domain and the position of the area (or of the boundary) where the waves are generated is known. In this case it is possible to find the source terms appearing into equations (3.48) or (3.38) by an inversion technique as follows. The first step is to solve the model equations using a unit value of the source term. The result of such preliminary computation is referred to as $N'\left(x, y, \omega\right)$. In view of the linearity of the problem the true solution in the frequency domain $N\left(x, y, \omega\right)$ can be

obtained by multiplying N' for the Fourier Transform of the unknown source term, indicated as $S(\omega)$:

$$N\left(x, y, \omega\right) = S(\omega) N'\left(x, y, \omega\right). \tag{3.49}$$

Let assume that at one point P of the computational domain the elevation of the surface η_P is available, i.e. the free water surface registration. Then at that point the transformed variable N_P can be easily calculated. Equation (3.49) can be inverted to obtain the source term $S(\omega)$:

$$S(\omega) = \frac{N_P(\omega)}{N'_P(\omega)} \tag{3.50}$$

where N'_P is the result of the unit source term computations at the point P. Of course this procedure is easy to apply using only the surface elevation at one point and when an identical source term, which in principle is a complex number, applies to all the generation areas/boundaries. This implies for example that the waves are generated with the same height and phase.

If the records at more than one point are available, two alternative uses can be made of the data. On the one hand it can be assumed that the source term is identical for all the generation areas/boundaries, and an optimization procedure can be used to find the value that best fits the data. On the other hand it can be assumed that each of the generation area/boundary has its own value of the source term and it is possible to write a linear system to be solved for these unknown source terms. Alternatively an over-determined system (the number of records available is greater than the number of source terms to be found) can be solved by means of an optimization procedure.

A further practical point of interest is that the discrete Fourier Transform is used and a finite set of equations is obtained, representing a finite time interval in the frequency domain. The integral transform of the data used to generate the waves (time series of η_P, h, u^I) is carried out using the Fast Fourier Transform. Each of the resulting field equations in the frequency domain (3.29) or (3.48) is solved using an available mild slope equation solver based on the finite element method (for details see Beltrami et al., 2001; Bellotti et al., 2003). The inverse transform of N is finally carried out using the Inverse Fast Fourier Transform.

As far as the length of the time interval to be considered is concerned it should be kept in mind that when solving partial differential equations using the discrete Fourier Transform the solution is obtained for a finite time

interval; it is assumed that the solution is periodical over that time interval and that it repeats identically over the following and the preceding time. Therefore the selected time interval should be long enough to allow all the wave energy to exit the computational domain trough the open boundaries before the time interval ends. Otherwise interference between wave energy coming from different time intervals is obtained. If all the wave energy has left the domain at the end of the computation, the following one has zero initial conditions everywhere, as desired.

To save computational time the elliptic equation (3.29) or (3.48) can be solved only for those wave frequencies for which the Fourier Transform of the source terms used to generate the waves is significantly greater than zero. Some wave components (especially the high frequency ones) receiving negligible energy should not been considered and the corresponding equation (3.29) or (3.48) not solved.

The model here presented has some features that make it suitable to be used in early warning systems for the tsunamis. Firstly it can be applied in two stages: one is extremely expensive from the computational point of view, the other is very fast and can be applied in real-time. The idea is first to define the computational domain and the areas/boundaries where the waves are generated and to solve the elliptic equations using a unit value of the source term. This part of the procedure may be computationally expensive since the solution of hundreds of elliptic equations may require hours or days. However after these computations have been performed and the results at the points of interest have been saved, the actual computation of the wave propagation is very fast. Once the time series of the waves to be generated ('direct' approach) or the time series of the waves recorded at some point of the domain by tidal gauges ('indirect' approach, as it would be for early warning systems) are available, the source term can be quickly calculated and the results at each point obtained by means of the inverse Fourier transform. As known these computations, for the amount of data commonly used for the problems studied here, take few seconds also on very slow computers. Therefore when setting up an early warning system the big part of the work is to define the scenarios (generation areas/boundaries), and to perform the unit source terms computations. Then the results can be used for the simulation in real time, forecasting the properties of the waves at the desired points of the computational domain at an acceptable computational cost. In the section 5.3 is presented an application of the model which shows an example of tsunami forecasting in real time: after

the a priori heavy computations with a unitary source term are solved, it is shown how the model predicts in few seconds the water surface elevation at one target point, as the data become available at a point close to the generation area.

3.3 Application of the parabolic approximation of the MSE

The MSE of elliptic type defines a problem which is in general properly posed only if boundary conditions are specified along the boundaries of the computational domain. In order to obtain a numerical solution over a large area in the horizontal plane, a great amount of computing time and storage is required, because the elliptic equation needs simultaneous solution over the whole area. Therefore there was a natural incentive for developing an approximation of the MSE which bypasses these numerical difficulties. The parabolic equation method served that objective. It consists in approximating the elliptic wave equation to a parabolic equation, which is easier to solve numerically because allows a solution scheme which proceed along the predefined wave direction. The standard parabolic wave equation has the disadvantage that the direction of waves must be substantially similar to the predefined one. As the waves refract and diffract, they change direction and the accuracy of the approximation decrease with increasing angle between waves and the initial predefined direction.

An application of the model implemented in this work regards a matching between the elliptic MSE, solved in a closed domain where diffraction and reflection are important, and the parabolic MSE, solved in a larger domain where waves propagate undisturbed. The idea behind this matching is to reduce the computational costs using a faster numerical technique when solving the waves propagation over large oceanic areas, so that the model can be more efficient and results of practical use.

A further point of interest is that the tsunamogenic source can be typically viewed as a small region with respect to the full domain where the tsunamis can propagate, this is specially true in the case of landslide generated tsunamis. It is therefore clear that the waves will travel radially away from the source and thus the use of cylindrical coordinates apperas to be very appropriate. In the following the parabolic MSE is derived in a cartesian

coordinates system of references, while in the appendix B.3 it is derived the transformation of coordinates by adopting a cylindrical system of reference.

3.3.1 Derivation of the parabolic MSE

The first derivation for surface water waves of the parabolic type mild slope equation was given by Radder (1979). He demonstrated a method based on the use of a splitting-matrix, which divides the wave field into transmitted and reflected components. The result is a pair of coupled equations for the transmitted and the reflected fields. By assuming that the reflected is negligible, i.e. no backscattering, a parabolic equation is obtained for the transmitted field.

Further Liu & Tsay (1983) have described a method for obtaining the back-scattered wave by an iterative procedure, using coupled equations similar to those obtained by Radder (1979). An advantage of his approach is that it emphasizes explicitly that the parabolic approximation correspond to neglecting the reflected part of the waves.

Liu & Mei (1976), derived the parabolic equation by employing the WKBJ-approximation (see afterward) for the velocity potential, and they studied wave shoaling on a plane beach and interacting with breakwaters, while Mei & Tuck (1980) studied waves diffracted by slender obstacles in water of constant depth.

Kirby & Dalrymple (1988, 1984, 1983) obtained the same the parabolic mild slope equation for weakly non linear waves, using the multiple-scale perturbation expansion of Yue & Mei (1980) but allowing slow variations of the water depth.

Here the parabolic approximation of the MSE is briefly derived, starting from the elliptic MSE in term of free water surface elevation

$$\nabla_h \left(cc_g \nabla_h N \right) + k^2 cc_g N = 0 \tag{3.51}$$

The mild slope assumption yields that the horizontal length scale (Λ) over which the water depth varies considerably is much larger than the wave length scale (λ). Because of that many waves are present in the region of variable depth. Thus such problems are called short-waves asymptotic, in the sense that the wave length is short compared to the dimension of the region where it propagates. Short-waves asymptotic method are also known as WKBJ methods after Wentzel, Kramer, Brillouin and Jeffreys developed

these methods for use in quantum mechanics in the 1920ies. The essence of the WKBJ expansion method is to suppose that the amplitude function varies much more slowly than the phase function in the horizontal space. Thus the WKBJ approximated solution of the MSE is taken, with the restriction of considering waves propagating only in x direction:

$$N(x,y) = A(x,y)\, e^{-i\int k dx} + c.c. \tag{3.52}$$

Since the wave motion is primary in the x-direction, the variation of the amplitude in the y direction is an order of magnitude slower than in the x direction. This can be expressed formally by introducing other variables named X and Y and given by

$$\begin{aligned} X &= \epsilon^2 x \\ Y &= \epsilon y \end{aligned} \tag{3.53}$$

where ϵ is a small parameter. The changed variables implies that the horizontal space derivatives become

$$\begin{aligned} \frac{\partial A}{\partial x} &= \frac{\partial A}{\partial X}\frac{\partial X}{\partial x} = \epsilon^2 \frac{\partial A}{\partial X}; \qquad \frac{\partial^2 A}{\partial x^2} = \epsilon^4 \frac{\partial^2 A}{\partial X^2} \\ \frac{\partial A}{\partial y} &= \frac{\partial A}{\partial Y}\frac{\partial Y}{\partial y} = \epsilon \frac{\partial A}{\partial Y}; \qquad \frac{\partial^2 A}{\partial y^2} = \epsilon^2 \frac{\partial^2 A}{\partial Y^2} \end{aligned} \tag{3.54}$$

The first term of the MSE (3.51) can be expanded, yielding to

$$cc_g\eta_{xx} + (cc_g)_x \eta_x + cc_g\eta_{yy} + (cc_g)_y \eta_y + k^2 cc_g\eta = 0 \tag{3.55}$$

Then substituting equation (3.52) into equation (3.55) and using the new variables (X and Y) it yields to

$$\begin{aligned} &cc_g\left[\epsilon^4 A_{XX} + 2\epsilon^2 A_X ik + \epsilon^2 ik_X - k^2 A\right] + \epsilon^2 (cc_g)_X \left[\epsilon^2 A_X + ikA\right] + \\ &\epsilon^2 (cc_g A_Y)_Y + k^2 cc_g A = 0 \end{aligned} \tag{3.56}$$

if the terms of order $O(\epsilon^4)$ are neglected, the equation (3.56), after some simplifications, at the order $O(\epsilon^2)$ becomes

$$2ikcc_g A_X + i(cc_g k)_X A + (cc_g A_Y)_Y = 0 \tag{3.57}$$

Equation (3.57) is the parabolic approximation of the MSE, its solution provides the slowly varying amplitude $A(x,y)$, which multiplyed by

the exponential function $e^{-i\int kdx}$, gives the water surface elevation for monochromatic waves.

Equation (3.57) can be viewd as a convection-diffusion equation, except that instead of solving the time marching of the heat, the wave spatial (x-direction) advancing is sought for. For the solution of the parabolic MSE a Crank-Nicolson finite difference numerical tecnique is implemented, which uses the central difference for the x-space derivative at the position $x_{i+1/2}$ and the second order central difference for the y-space second derivative at position y_j and . Thus equation (3.57) written in finite differences becomes

$$\begin{aligned} &2ikcc_g\frac{A_j^{i+1}-A_j^i}{\Delta x}+iA\frac{(cc_gk)_j^{i+1}-(cc_gk)_j^i}{\Delta x}+\frac{(cc_g)_{j+1}^{i+1}-(cc_g)_{j-1}^{i+1}}{2\Delta y}\frac{A_{j+1}^{i+1}-A_{j-1}^{i+1}}{2\Delta y}+\\ &\frac{cc_g}{2}\left[\frac{A_{j+1}^{i+1}-2A_j^{i+1}+A_{j-1}^{i+1}}{\Delta y^2}+\frac{A_{j+1}^{i}-2A_j^{i}+A_{j-1}^{i}}{\Delta y^2}\right]=0 \end{aligned} \tag{3.58}$$

Writing equation (3.58) by expliciting the unknown term A^{i+1} as function of the known ones A^i a system with a tridiagonal matrix is achieved. The solution of a tridiagonal system is computed by means of the Thomas algorithm, which strongly reduces the computational costs and it is a simplified form of a Gaussian elimination (see Appendix C).

The validation of the solution of the parabolic MSE and its matching with the solution of the elliptic MSE is shown in the section 4.6 by means of some numerical experiments. For the validation experiment the parabolic MSE is solved in cylindrical coordinates (r and θ).

Chapter 4

Model validation

This chapter describes the model validation, carried out by comparing the model results with those obtained from different experiments, physical or numerical, choosen as reference solution. All the physical models described and used for comparison were performed in the same framework of research projects aimed at studying landslide waves.

Sections 4.1 and 4.2 show the first comparisons carried out between the numerical simulations anf two physical model measurements. The physical models have been carried out at the Environmental and Maritime Hydraulic Laboratory (LIAM) of the University of L'Aquila, Italy. Both models aim at studying the propagation of water waves generated by landslide, where a simplified reproduction of the generation mechanism is carried out, as it will be explained. The first model is performed in a wave channel, while the second one in a wave tank, allowing the study of the three dimensional phenomeno. These experiments are used to validate the indirect procedure to generate waves at a boundary of the numerical domain. A further point of interest addressed in these 2 sections is the comparison with two long wave models (based on the LSWE and on the linearized BTE), in order to show the importance of a proper reproduction of frequency-dispersion. Section 4.3 describes some numerical 3-D experiments implemented in order to validate the inclusion of the source term in the MSE (equation 3.48). They consist in a comparison between the present depth integrated model with a 3-D numerical model, which solves the Laplace equation and reproduces the landslide movement in the bottom boundary condition. As it will be explained, the 3-D code is taken as the reference solution to validate the correct inclusion of the wave generation term in the MSE. Further validation

is carried out by comparison with other physical experiments (see section 4.4), which intend to reproduce the landslide generated waves using a realistic model of the landslide, and a wave tank large enough to study the wave propagation in the far field. The physical model was build at the LIAM laboratory of L'Aquila University, Italy.

Section 4.5 describes other experiments carried out at the Research and Experimentation Laboratory for Coastal Defence (LIC), of the Technical University of Bari, Italy. These experiments reproduce the particular case of a landslide falling at the flank of a conical island and allow the analysis of the generated wave field close to the island and in the far propagation field. The physical experiments are reproduced with the numerical model which provides results in good agreement with the laboratory measurements. The numerical model is tested both with the 'indirect' and the 'direct' procedure, in order to validate its application to work in a early warnuìing system and to gain more insight on generation and propagation of tsunamis for this particular bathymetric configuration.

In the end, section 4.6 presents a test case to validate the model application to large geographical areas, by means of matching the solution of the elliptic MSE with its parabolic approximation.

4.1 The Scott–Russel's wave generator

The physical model reproduces the so called Scott-Russel's wave generator (see the sketch on figure 4.1 and the picture on figure 4.2), i.e. a box falling vertically into the water (Monaghan & Kos, 2000). The wave flume is made up of steel and PVC, and is 12.00 m long, 0.30 m wide and 0.45 m high; the box (0.10 m x 0.10 m x 0.30 m) is made of PVC. The wave generator was placed at one end of the flume while at the other end absorbing material was used to reduce the wave reflection.

The water level oscillations were measured by means of five resistive wave gauges placed along the flume, respectively at 0.40, 0.85, 1.30, 1.75 and 2.20 m from the left boundary of the flume. The gauges were characterized by an instrumental noise lower than 0.1%. The data were collected using a 16 channels National Instruments analog-to-digital conversion board. The recorded water level data cover a period of 20 s with a 1000 Hz sampling frequency. The experiments were carried out for four different water depths (0.06 m, 0.10 m, 0.18 m and 0.23 m), and for each of these the box was

released with the bottom placed at $-0.03\ m$, $0.00\ m$ and $0.03\ m$ from the still water surface; for further details refer to Di Risio (2005) and Panizzo et al. (2002).

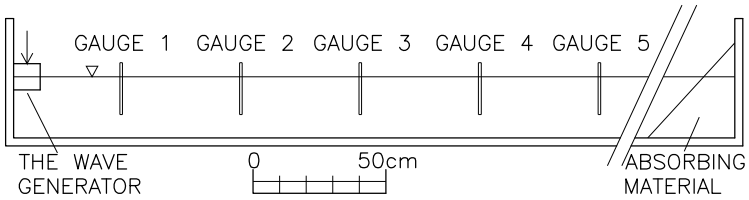

Figure 4.1: Sketch of the experimental layout of the Scott Russell's Wave generator experiment.

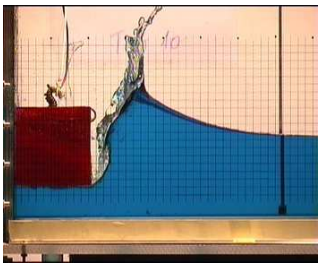

Figure 4.2: Instantaneous picture of the reproduction of a Scott Russell's Wave generator experiment.

The numerical simulations are performed using a one-dimensional domain. The left boundary of the numerical domain falls at the point where the right-bottom corner of the box impacts the water surface. At that point the wave-maker boundary condition (3.38) is imposed, while at the right boundary the radiation condition (3.34) is used, although in the physical model the absorption of the outgoing waves was not perfect. The numerical domain has a total length of 4 m and here the MSE expressed by equation (3.29) is solved. The time series reproduced in the numerical model is of 10 s, using a Δt of 0.001 s. This results in a total of $10,000$ time steps, which in

the frequency domain correspond to the same number of angular frequencies ω, ranging between $2\pi 10^{-1}\ rad/s$ and $2\pi 10^{3}\ rad/s$. By taking advantage of the fact that the results in the positive semi-axis of the frequency are complex conjugates of those along the negative semi-axis, only half of the solution is sought for.

The 'indirect' procedure is applied to calculate the source term to be used in the wave-maker boundary condition (left boundary), being known the elevation of the free surface at the points where the gauges are located. The experimental results at the gauge 1 are used to estimate the source term, while the results at gauges 2, 3, 4 and 5 are compared with the numerical model results. The first step is to solve the field equation (3.29) together with the boundary conditions described in section 3.1.2, where a unit source term is imposed at the wave-maker boundary condition (3.38). Consequently the unit solution $N'(x,\omega)$ is obtained in the computational domain; the value of this variable at the point corresponding to the gauge 1 is referred to as $N_1'(\omega)$. The records obtained at the gauge 1 are then used to calculate the variable $N_1(\omega)$ as the Fourier Transform of the experimental time series of the surface elevation. Since during the experiments, part of the generated waves were reflected at the right boundary, the records obtained at the gauge 1 suffer of reflected and re-reflected (at the left boundary) waves. However it was easy to estimate the time at which the reflected waves had affected the records and to smoothly set the signal to zero, in order to avoid generation of spurious waves in the numerical test. The source term $S(\omega)$ to be used in the boundary condition is then calculated by an equation equivalent to the (3.50). The results in the whole computational domain are given by

$$N(x,\omega) = S(\omega)\, N'(x,\omega)\,. \tag{4.1}$$

The water surface elevation $\eta(x,t)$ is obtained using the Inverse Fast Fourier Transform with respect to the time, for each computational point of interest, such as those at the position of the wave gauges.

The results of one representative test are presented. The water depth used in the experiment is of 0.23 m and the box released with the bottom placed at the still water level. Figure 4.3 shows the surface elevation, $\eta(t)$, measured by the five gauges (dashed red lines) and those resulting from the numerical simulations with the present model (solid black lines).

The waves typically present first a crest, then a trough; this is due to the

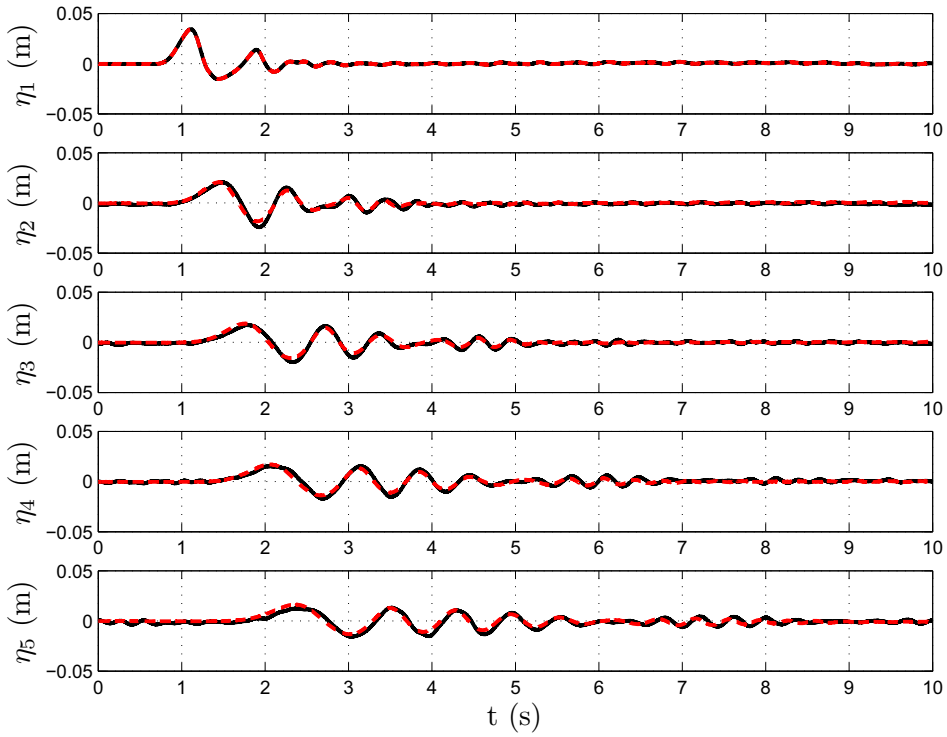

Figure 4.3: Surface elevation at gauges 1, 2, 3, 4, 5 (from top to bottom). Solid black lines represent results from the present model, dashed red lines are experimental values.

generation device, which acts like a piston that generates firstly a positive wave. The waves appear to lengthen as they propagate away from the generation area (i.e. their period increases). The wave height decreases, mainly due to the frequency dispersion, which makes the wave train to become longer, and therefore the wave energy to be less concentrated in space.

Figure 4.4 presents the surface elevations for the same test case, comparing the physical model measurements (dashed red lines) with the results of the present model used with the approximation of the long wave theory, i.e. without frequency dispersion, (dashed black line), and the results of the solution of the linearized version of the BTE of Nwogu (1993) (thin solid line). Please note that the numerics used to solve the equation is

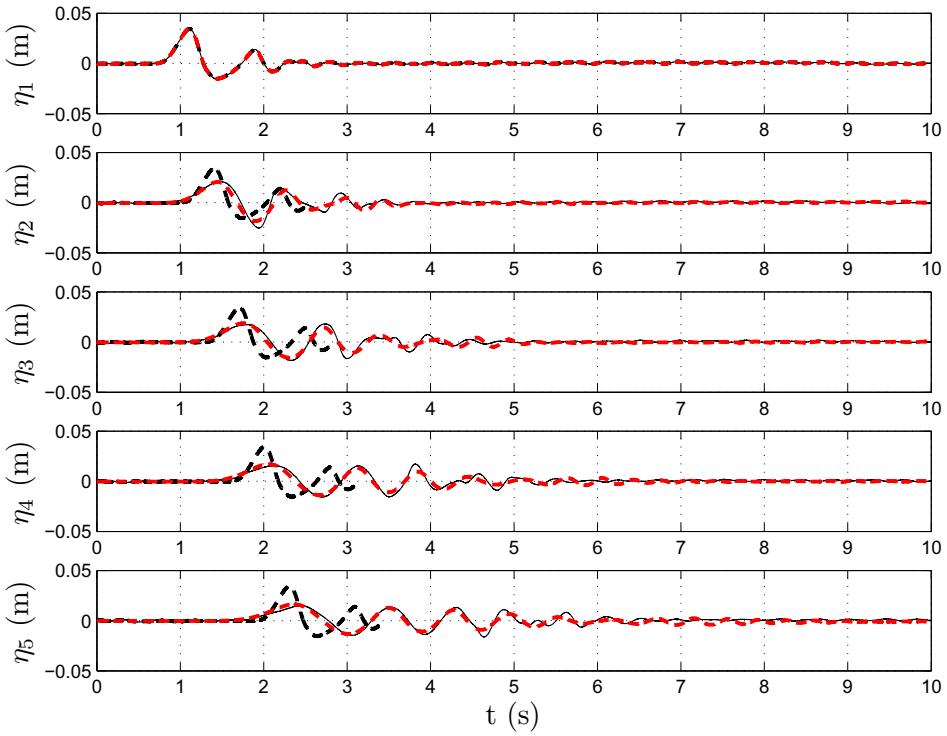

Figure 4.4: Surface elevation at gauges 1, 2, 3, 4, 5 (from top to bottom). The dashed red lines again represent the experimental values. The dashed black lines are the present model results solved with the long wave approximation. The thin black line represents the model based on the BTE (Nwogu, 1993). Please note that the dashed black line is truncated after the first two waves, to make the results more readable.

identical for the models.

The results of the present numerical model, as seen in figure 4.3, appear to compare satisfactorily with the experimental data. Important properties of the waves at hand, such as the arrival time of the crest, the wave height and the wave period are reproduced with high accuracy. The elevation of the first wave crest at the gauge 5 is evaluated with an underestimation of about 12%. The solution of the BTE (figure 4.4), as expected, also results to be in perfect agreement with the experiments. On the contrary the LSWE reproduce waves that propagate with a frozen shape along the domain. The

first crest arrives earlier than that measured in the experiments, and the waves are higher than those expected. Of course the non proper reproduction of the frequency dispersion leaves all the wave components to propagate together. As the distance from the generation area grows these errors become unacceptable.

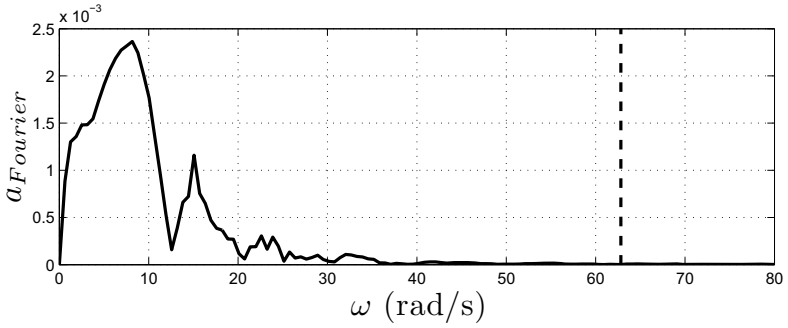

Figure 4.5: Amplitude spectrum of the surface elevation at gauge 1 for the experiment with water depth sets at 0.23 m and the box released from the still water level. The dashed line indicates the highest frequency component reproduced in the model.

It is worth to briefly discuss how the energy of these considered transient waves is distributed in the frequency domain. The modulus of the Fourier Transforms coefficients of the measured water level oscillations at gauge 1 is reported in the figure 4.5 against the angular frequency. The figure is cut at the angular frequency of 80 rad/s, because it is considered not advisable to show the wave spectra until the $2\pi \cdot 10^3$ angular frequency, and it can be noted that very high frequency components, as expected, receive minor energy. The accurate reproduction of these waves may therefore be avoided in order to save computational time. For the present experiments it has believed sufficient to solve the equation (3.29) up to frequencies corresponding to $kh = 92.6$ ($0.1Hz < f < 10Hz$). This limit is shown in the Figure 4.5 by the vertical dashed line. The higher frequency component corresponds to a wave length (for the considered water depth) of 0.0156 m, thus an appropriate finite element grid (the maximum distance from the computational nodes) of 0.0015 m has been used since a resolution of about 10 nodes per wave length is required; the resulting number of Degrees of Freedom (DOF) is 42,600. The solution of the elliptic equation has been carried out, using always the

same, very fine grid, for 100 discrete frequencies. The total computational time is of the order of 8 minutes on an AMD Opteron 246 2GHz computer equipped with 4GB of RAM.

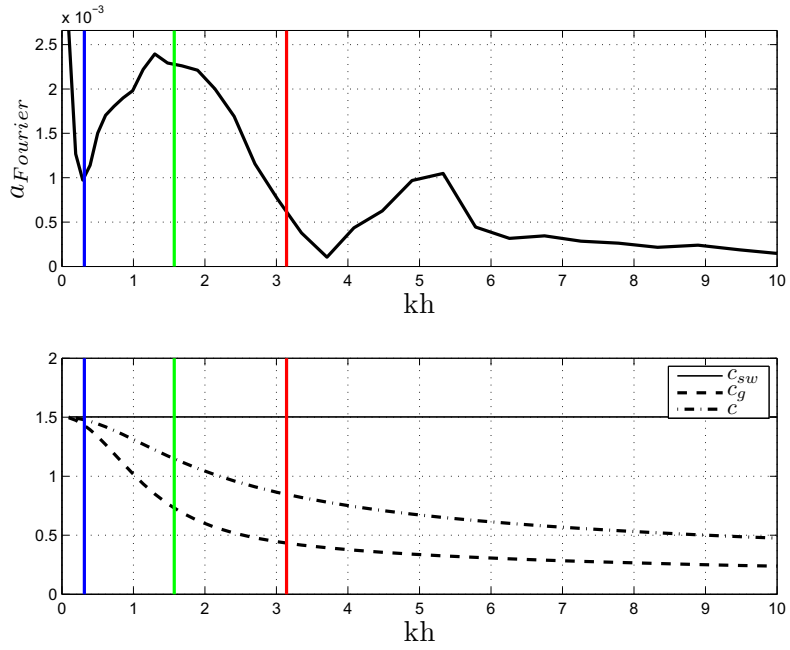

Figure 4.6: Upper panel: amplitude spectra of the surface elevation equal to that described in caption of Figure 4.5 versus the wave length parameter. Lower panel: distribution of the wave celerities over the wave length parameter; the three vertical solid lines represent the frequencies corresponding to $h/L = 1/20$ (blue), $h/L = 1/4$ (green) and $h/L = 1/2$ (red).

The figure 4.6 looks in more detail how the wave energy is distributed in frequency. In the upper panel the same amplitude spectra of the water level oscillation at gauge 1 is reported now versus the wave length parameter written as kh. The figure is zoomed only for those frequencies where there is the major wave energy content. In the lower panel are reported the wave celerity functions against the same wave length parameter: the solid line represents the wave celerity in the shallow water approximation ($c_{sw} = \sqrt{gh}$), while the dash-dot line and the dashed line represent respectively the phase

and group celerity obtained from the wave dispersion relation. Three vertical solid lines, in both panels, show the frequencies corresponding to $h/L = 1/20$, $h/L = 1/4$ and $h/L = 1/2$ (blue, green and red respectively). These values correspond roughly to the limit of applicability respectively of the long waves theory, of the traditional BTE by Peregrine (1967), and to the deep-water waves limit. It is clear that much of the wave energy belongs to wave components hardly reproducible with traditional, non dispersive long waves models. Many tests (up to 50) have been reproduced in order to further validate the model, always obtaining similar results. However, as the water depth used in the experiments decreases (and the generation mechanism remains the same), the waves tend to become longer with respect to h. In those conditions the differences between the frequency dispersive and the non dispersive one are reduced. Furthermore, for very small water depths (i.e. $h = 0.06$ m), the ratio between the amplitude of the waves and h becomes such that the nonlinear effects (i.e. the amplitude dispersion) appear to dominate the propagation. Under those conditions the present model, which is based on linearized equations, becomes unapplicable and may lead to unrealistic results, such as the fact that the waves propagate much slowly than those in nature. A limit to respect is that the amplitude of the waves should not be larger than 1/4 of the water depth.

4.2 Axial-symmetric landslide generated waves

The experiments described in this section are similar to those of the Scott-Russel wave generator, but they occur in a wave tank instead of a wave channel. The physical model reproduces a quarter of a cylinder falling vertically in the corner of a wave tank, as depicted in the sketch reported on the left panel of Figure 4.7 and in the picture of Figure 4.8. The tank is built in bricks; dimensions in plan are of 10.8 m and 5.4 m; the maximum water depth is of 0.8 m. A system of five resistive wave gauges, placed along a line as indicated in the Figure 4.7, measures the water level oscillations. The gauges used are identical to those described in the previous section and their distance from the corner where the waves are generated is of 0.63, 1.33, 2.04, 2.75 and 3.45 m. The experiments were carried out using four different values of the water depth, respectively 0.09, 0.16, 0.28 and 0.36 m; the body

was released from several levels above and below the still water surface. Two cylinders, one with a height of 0.157 m and a radius 0.157 m, the other one with a height and a radius of respectively 0.157 m and 0.215 m have been used.

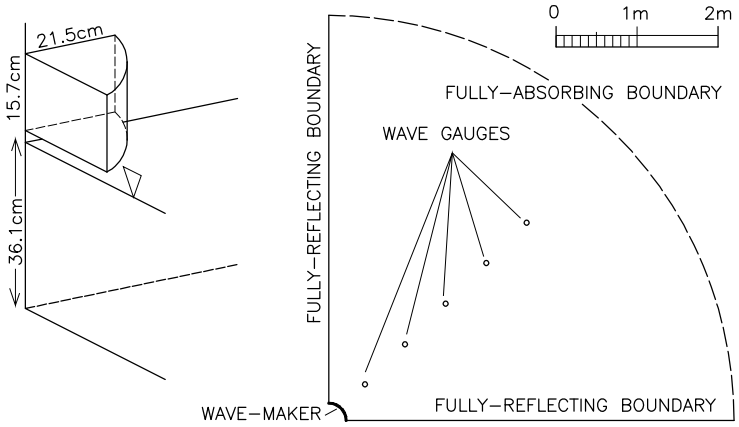

Figure 4.7: Layout of the axial-symmetric experiment (left panel) and sketch of the computational domain (right panel).

The selected numerical computational domain is a quarter of a circle (radius of 5.0 m) as shown on the right panel of Figure 4.7. At the corner a small quarter of a circle whose radius is identical to that of the cylinder, is used to specify a wave maker boundary condition. Along the curved boundary absorption of the outgoing waves is achieved by means of the radiation boundary condition. It is to be stressed that in the physical model experiment the waves were almost perfectly reflected at the walls, and this introduces a possible source of discrepancy between experimental data and numerical computations, that will be discussed later.

The time series reproduced by the numerical model is 20 s long, and a Δt=0.001 s has been used, resulting in a total of $20,000$ time steps and a corresponding number of ω to be considered in the frequency domain. The Fourier Transform of the surface elevation at the gauge 1 has been preliminary used to evaluate those frequencies for which it was worth to solve the field equation (3.29). It was concluded that 40 frequencies had to be considered for the solution of the equation (3.29), for the range $0.05Hz <$

Figure 4.8: Picture of the experiment.

$f < 2\ Hz$. The higher frequency component, for the considered water depth, has a wave length of 0.39 m and consequently the maximum length of the finite element of the computational grid is of 0.04 m (DOF = 26,400). The total computational time for the solution of the 40 elliptic equation is, on the same computer described before, of 12 minutes.

Here again the results of one representative test are illustrated. It has been carried out using a water depth of 0.36 m and the cylinder (radius of 0.215 m) released with the bottom placed at the still water surface. The recorded time series of the water surface elevation is reported in Figure 4.9 (dashed red lines). On the same Figure, as for the previous validation test, the results of the present model are reproduced using a solid thick lines, while the thin dashed black lines represent the results of the LSWE. The source term used at the wave-maker boundary has been calculated using the experimental results at the gauge 1. However, since these records are affected by the waves reflected at the side walls, only the first part of the signal has been used when applying the equation (3.50), setting smoothly the rest of the time series to zero.

Careful comparison of the records at the 5 gauges allows estimation of the time at which the reflected waves contaminate the records of the first wave packet, radiating from the generation area. At the gauge 1 it appears

that the radiating wave packet is recorded for $2 < t < 6$ s, while the reflected waves reach this gauge for $t > 9$ s. For the subsequent gauges the reflected waves arrive earlier and the radiating waves arrive later than for the gauge 1. The first packet of radiating waves measured at the gauge 1, 2 and 3 appears to be not strongly affected by the reflected ones. On the contrary the records at the gauges 4 and 5 are likely to be completely affected by the reflected waves and therefore these results should be used with care.

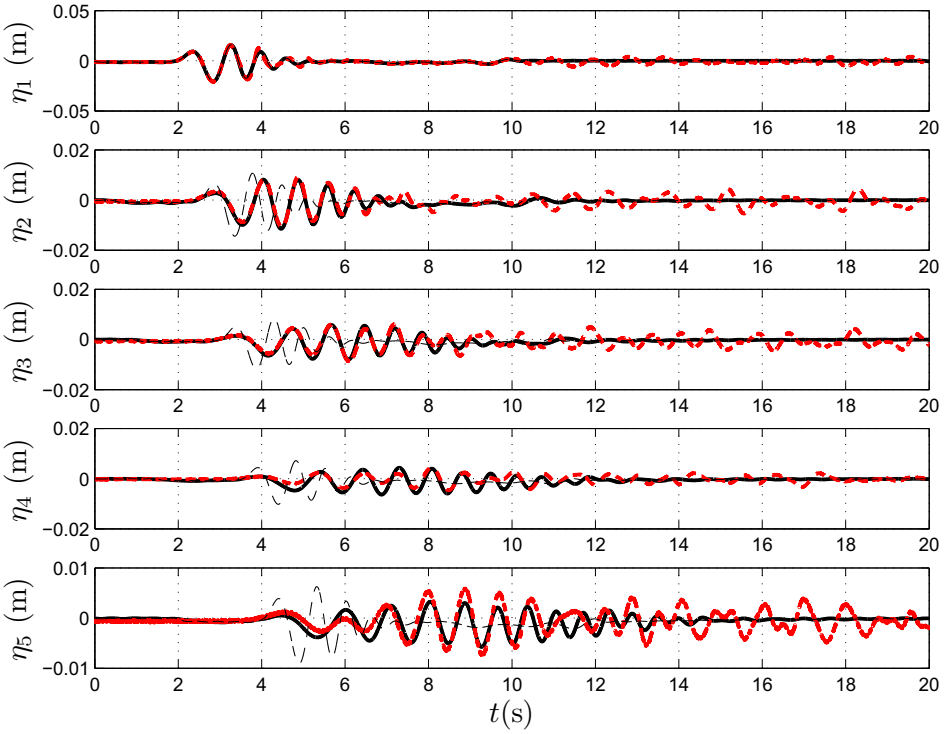

Figure 4.9: Axial-symmetric experiment. Surface elevation at gauges 1, 2, 3, 4, 5 (from top to bottom). Solid thick line represents results from the present model, dashed red lines are experimental values and the dashed black lines are the results of the present model with wave celerity from the long wave approximation.

Similarly to the experimental results presented in the previous section, the waves appear to undergo frequency dispersion as they propagate away from the generation area, i.e. their period appears to increase and the wave packet

becomes less concentrated in space and time. This also makes the height of the waves to become smaller. Here however, the waves also undergo the so called circumferential dispersion, i.e. the height of the waves decreases in view of the fact that the wave front becomes longer as they propagate. The numerical model is able of carefully reproducing the experimental results. This is especially true for the first gauges (1, 2, 3 and 4). The results are not good for the gauge 5, where the height of the predicted waves is smaller than that measured. This is probably due to the effect of the reflected waves, which were not modeled numerically. Results of the same order of accuracy would be obtained using the BTE of Nwogu (1993), that are not presented here for sake of clarity of the figure.

The LSWE appear to provide a wave field different from that observed in the experiment. The wave packet predicted by these equations remains very similar during the propagation, although the circumferential dispersion (properly taken into account by the model) induces a decrease of the wave height, as expected. However the arrival time of the highest waves appears to be predicted with large errors.

4.3 Inclusion of waves generation term - Numerical experiments

This section describes some numerical experiments which reproduce the water waves generated by the deformation of the bottom due to the movement of a submerged landslide. The idea is to validate how the effects of the bottom movement are reproduced in the depth integrated model using equation (3.48). Here the model is applied with a 'direct' procedure, meaning that the deformation of the sea floor is known, and its effects on the free water surface are simulated.

These experiments compare the results of the depth integrated model with those of a three dimensional one, which can be regarded as the reference (i.e. the true) solutions. The three dimensional model solves the Laplace equation within the linearized boundary conditions. It uses the same numerical scheme of the depth integrated model, thus the equations are solved in the frequency domain and are formulated as follows

$$\nabla_h^2 \Phi + \Phi_{zz} = 0 \tag{4.2}$$

$$\Phi_z - \frac{\omega^2}{g}\Phi = 0 \tag{4.3}$$

$$\Phi_n = fft\left(h_t\right) \tag{4.4}$$

$$\Phi_n + ikcos\left(\theta_n\right)\Phi = 0 \tag{4.5}$$

where $\Phi\left(x, y, z, \omega\right)$ is the Fourier transform of $\phi\left(x, y, z, t\right)$. Equation (4.2) is the Laplace equation, equation (4.3) is the free surface dynamic and kinematic boundary condition, equation (4.4) represents the moving bottom boundary condition and equation (4.5) is the radiation condition.

In order to further investigate on the source term included in the mild slope equation, some consideration can be made. When the extension of the seismic source is very large in comparison with the water depth a well accepted method for incorporating the effect of the moving seafloor into the depth integrated equations is to assume that the bottom movements instantaneously transfer to the surface elevation. A source term calculated as the time derivative of the water depth is added to the continuity equation (right hand side)

$$\eta_t + \bigtriangledown \cdot \left(\vec{v}h\right) = -h_t \tag{4.6}$$

where as usual η, $\vec{v}$ and h represent respectively the instantaneous elevation of the free surface, the depth integrated horizontal velocity of the fluid and the water depth. Since the movements induced by earthquakes are very fast in comparison with the waves celerity, these are alternatively represented as initial conditions for the wave model.

The problem becomes much more complicated for tsunamis generated by landslides. These can still be regarded as seafloor deformations, but the spatial extent of the source is usually not much larger than the water depth. Furthermore the time scale of the landslide movements is comparable to that of the waves propagation. Three dimensional numerical models are therefore applied to get detailed descriptions of the flow field, see for example Grilli et al. (2002). Depth integrated models are able also in this case to properly simulate the wave propagation in the far field, but cannot give a detailed description of the flow in the generation area. In these cases it is well accepted that the movements of the bottom do not transfer as they are

to the free surface; Tinti et al. (2006b), have therefore proposed to express the continuity equation as follows

$$\eta_t + \nabla \cdot (\vec{v}h) = -h_t \frac{1}{cosh\,(k_s h)}. \tag{4.7}$$

Their method makes use of the time derivative of the water depth as a source term in the continuity equation, multiplied by a filter function which depends on the water depth (and therefore may vary in space) and on the length of the landslide. In equation (4.7) $k_s = \frac{2\pi}{L_s}$ is the wave number of the landslide, being L_s its length, while the water depth is calculated as the sum of the fixed bottom depth and the landslide elevation $h\,(x,t) = h^{bottom}\,(x) - h^{landslide}\,(x,t)$.

The effect of the wave frequency on the filter function between the seafloor movements and the surface waves has been addressed by Kervella et al. (2007). They have solved the linearized problem of the wave generation by seafloor movements over an horizontal bottom, using integral transforms. They have found that in the source term the time derivative of the bottom has to be multiplied by a filter function which has the form of that used by Tinti et al. (2006b), but it contains the wave number of the wave (k) instead of that of the landslide (k_s). Of course this appears natural if the solution is sought for in the wave frequency field, as Kervella et al. (2007) do, because the wave number k can be calculated for each value of the wave frequency. This is not obvious when solving time-depending model equations as the NLSWE using time-marching numerical schemes.

In order to improve the technique proposed by Tinti et al. (2006b), which is very simple and useful for pratical purposes, and following the idea of Kervella et al. (2007), their considerations are applied to the present model, therefore the MSE was derived considering a moving bottom boundary condition. As already demonstrated in section 3.1.3, including the sea-floor generation mechanism into the field equation brings to equation (3.48), here reported for clarity

$$\nabla_h\,(cc_g\nabla_h N) + k^2 cc_g N = -\frac{1}{cosh\,(kh)} fft\,(h_{tt}) \tag{4.8}$$

In the present subsection the effect of different landslides, moving on different water depths, is analyzed trough the right hand side of equation (4.8). The model's equations are solved also with the linear long wave approximation, in order to highlight the importance of reproducing or not the

wave frequency dispersion. The resulting wave fields are sometimes presented also in terms of amplitude spectra.

Many computations, varying the water depth, the landslide length and kinematic have been performed. Here however for the sake of brevity, results of few experiments are shown, which can be considered as representative of the majority of simulations. Two sets of sample results reproducing the wave field generated by submerged landslides in a constant depth domain, and in a slope are presented.

4.3.1 Constant depth experiments

The numerical experiments presented in this section are carried out using a constant water depth of 1 m. The landslide is modeled as a semi-ellipse which at a certain instant suddenly starts to move along the bottom at a velocity of 1 m/s for 2 s, for a total displacement of 2 m. We have tested two landslides with different lengths of 2 m (short landslide) and 4 m (long landslide), both with the same height (thickness) of 0.1 m. In the sketch of figure 4.10 the numerical domain, which is 10 m long, is represented. The results presented in the following refer to the two points depicted in the sketch: Point A at 1 m at the right of the crest of the landslide before it starts moving; Point B is at 6 m from the initial position of the landslide.

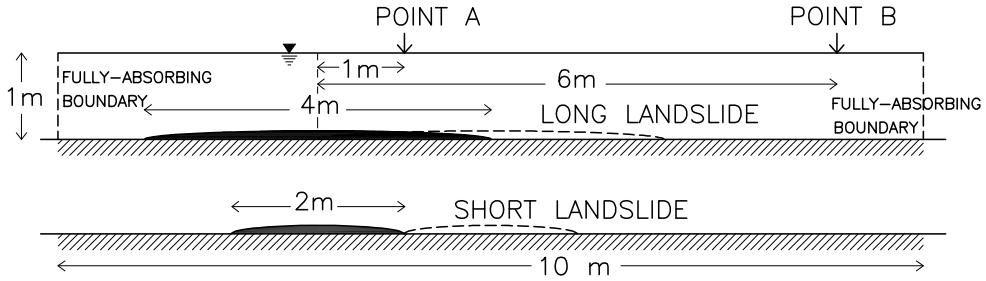

Figure 4.10: Sketch of the computational domain with the two different landslides lengths.

The present frequency-dispersive model is applied in a 1D domain 10 m long; the right hand side term used in the governing equation (4.8) is zero

everywhere except in the area where the semi-elliptic landslide moves. At the boundaries ($x = 0$ and $x = 10\ m$) the waves are allowed to exit the domain by imposing the radiation condition specified by the equation (3.34). The simulations here presented reproduce a time series of 100 s, using a Δt of 0.1 s. This results in a total of 1000 time steps, that in the frequency domain corresponds to the same number of angular frequencies ω, in the range between $2\pi \cdot 10^{-2}$ and $2\pi \cdot 10$. In the practice the MSE (4.8) is solved just for the frequencies in the range of $2\pi \cdot 10^{-2} \leq \omega \leq 2\pi \cdot 2$, where there is a significant content of wave energy. The higher frequency component has, for the considered water depth, a wave length of 0.4 m, thus the maximum distance between the computational nodes is of 0.04 m, since a resolution of about 10 nodes per wave length is required. The resulting number of Degrees of Freedom (DOF) is 201, and the elliptic equations for the 200 frequencies are solved on a 2 GHz CPU computer equipped with 4 GB of RAM (as all the other simulations presented here), with a total computational time of about 7 s.

In the simulations carried out with the three dimensional model, the Laplace equation (4.2) is solved in a two dimensional domain, again 10 m long and 1 m high (as the water depth). At the bottom boundary the condition of wave generation (4.4) is imposed, by letting the landslide to move along the bottom for 2 s. In order to compare the results with those of the depth integrated model, the same angular frequencies ω are solved ($2\pi \cdot 10^{-2} \leq \omega \leq 2\pi \cdot 2$). The finite element grid is composed of linear triangular elements, with the maximum distances between the nodes of 0.04 m, as for the depth integrated model. The number of DOF for these simulations is 8725 and the computational time is about 53 s.

In figure 4.11 the results of the numerical simulations with the two models are shown, in terms of the free surface elevation in time at the points A (left panel) and B (right panel) of figure 4.10. The landslide for the presented simulation is 4 m long and moves between $t = 10\ s$ and $t = 12\ s$. When the landslide starts moving, going in the direction of increasing x values, it generates a first crest-trough wave propagating in front of it, and a first trough-crest wave at its back. The results computed with the depth integrated model (solid black line) almost perfectly superimpose to the ones obtained from the three dimensional one (dashed red line). The good agreement is both in the generation (left panel) and in the propagation areas (right panel).

Simulations with the depth integrated model have been carried out also

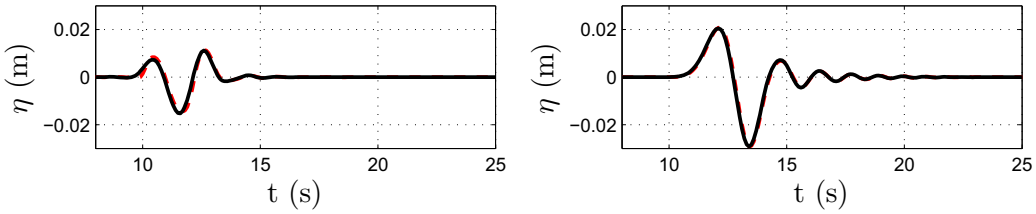

Figure 4.11: Comparison of the free surface elevation obtained from the three dimensional model (dashed red line) and that obtained from the depth integrated model (solid black line). The presented results are relative to the points A (left panel) and B (right panel) of figure 4.10.

by applying the filter function proposed by Tinti et al. (2006b) to the present model equation as follows

$$\nabla_h \left(cc_g \nabla_h N\right) + k^2 cc_g N = -\frac{1}{cosh\left(k_s h\right)} fft\left(h_{tt}\right) \tag{4.9}$$

In figure 4.12 the thin black line represents the surface elevation computed when applying equation (4.9), while the thick black line refers to the results of the proposed model (equation (4.8)). As in the previous figure, the left panel and the right panel show respectively the results at the point A and B. The comparison reveals that equation (4.9) provides a good reproduction of the first wave, but then presents a tail of spurious high frequency waves. This short wave packet does not appear in the simulations using equation (3.48), which attenuates the high frequency wave components. As stated by Kervella et al. (2007) '...the water column has an effect of a low pass filter, thus if the initial deformation contains high frequencies, they will be attenuated...'.

The results discussed so far are presented in terms of amplitude spectra in the frequency domain in the figure 4.13.

In this figure, the left panels (a, c and e) refer to a simulation with the short landslide (2 m long), while the right panels (b, d and f) to the same simulation with the long landslide (4 m). The top panels (a and b) reproduce the amplitude spectra at point A resulting from the three dimensional simulations (thin black lines), and those obtained with the depth

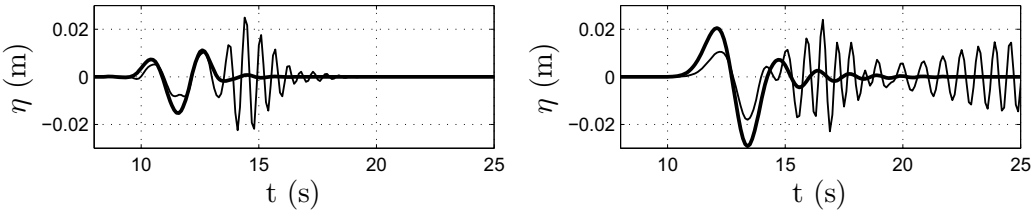

Figure 4.12: Comparison of the free surface elevation obtained from the depth integrated model with the frequency filter function (thick black line) and that obtained from the same model with the landslide filter function (thin black line). The presented results are relative to the points A (left panel) and B (right panel) of figure 4.10.

integrated model without applying any filter function to the source term (thick black lines) i.e. solving equation

$$\nabla_h \left(cc_g \nabla_h N \right) + k^2 cc_g N = -fft\left(h_{tt} \right) \tag{4.10}$$

The middle panels (c and d) represent the filter functions applied to the source term: the wave frequency filter, applied in the equation (4.8) (solid black lines), and the landslide filter applied in the equation (4.9) (dashed red lines). These functions are both constant in space since the water depth is constant all over the computational domain. When these filters are applied to the source term in the depth integrated simulations, the resulting amplitude spectra are those presented in the bottom panels (e and f): the solid black lines are those obtained solving equation (4.8), while the dashed red lines are those obtained solving equation (4.9). It is evident that without the application of any filter function the wave field contains much energy in the high frequencies, which do not result in the reference solution given by the three dimensional model. The landslide filter function has the same effect for all the wave frequencies, it changes only for different values of the ratio $\frac{h}{L_s}$. The wave frequency filter function on the contrary, depending on the wave number, reproduces the low-pass filtering effect of the water column above the landslide, thus attenuates the high frequency wave components. As seen in the previous figure, this filter allows to obtain results in very good agreement with the reference solution.

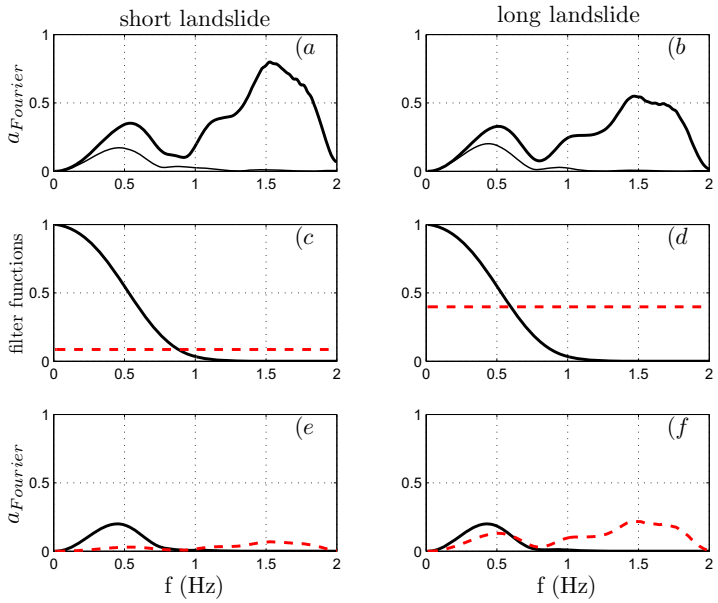

Figure 4.13: Panels a and b: absolute values of the Fourier transform coefficients of the water surface elevations at point A, computed with the three dimensional model (thin black line) and with the depth integrated model, without any filter function (thick black line); panels c and d: frequency filter (continuous black lines) and landslide filter (dashed red lines); panels e and f: absolute values of the Fourier transform coefficients of the water surface elevations at point A, computed with the depth integrated model, with the frequency filter (continuous black lines) and with the landslide filter function (dashed red line).

It is however clear that the presence of very high frequency waves is easily detectable when using a frequency-dispersive model. These waves would not appear so clearly when employing non-dispersive models. In order to show this, simulations with the depth integrated model based on the LSWE have been carried out, which lets each component to propagate at the same celerity. In particular the same experiments were simulated soving the following equations

$$\nabla_h \left(gh\nabla_h N\right) + \omega^2 N = -\frac{1}{cosh\left(kh\right)} fft\left(h_{tt}\right) \tag{4.11}$$

$$\nabla_h \left(gh\nabla_h N\right) + \omega^2 N = -\frac{1}{cosh\left(k_s h\right)} fft\left(h_{tt}\right) \tag{4.12}$$

and the model results are compared with the reference solutions of the three dimensional model.

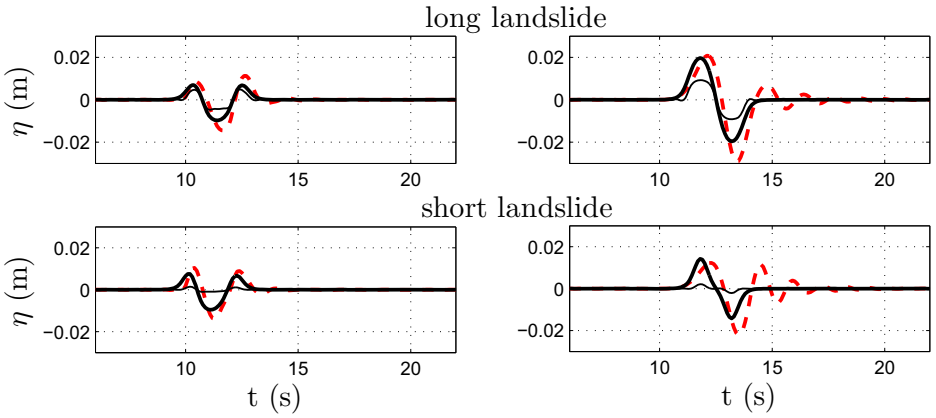

Figure 4.14: Comparison of the free surface elevation obtained from the three dimensional model (dashed red line) and from the long wave depth integrated model respectively using the frequency filter function (thick black line) and the landslide filter function (thin black line).The presented results are relative to the points A (left panels) and B (right panels) of figure 4.10.

Figure 4.14 shows the water surface elevation at point A and B (left and right panels respectively); the top panels refer to the long landslide simulation, while the bottom panel to the short landslide one. With the red dashed lines the three dimensional results are represented, the black lines are relative to the solution of equation (4.11) (thick lines) and equation (4.12) (thin lines). The comparison shows that a smaller extension of the generation area involves, for the landslide filter, a stronger cut in all the frequencies of the wave amplitude. As it can be seen by the thin lines in the bottom panels, these ones do not produce reliable results. The application of the wave frequency filter function better estimates the first crest-trough wave. However some differences arise in the comparison with the three dimensional solutions. These are due to the long wave approximation of the

depth integrated model, which provides a correct reproduction of landslide generated waves, only when the ratio $\frac{h}{L_s}$ is small.

4.3.2 Experiments on a plane slope

Another set of numerical experiments is carried out reproducing the movement of a submerged landslide on a plane beach. In the sketch of figure 4.15 the numerical domain is represented, which is 10 m long and with a $1:3$ slope; the landslide is also here a semi-ellipse, 4.21 m long and 0.1 m thick. The landslide suddenly starts to move after 10 s with a velocity of 1 m/s for 2 s and a total displacement of 2 m, as in the previous experiments.

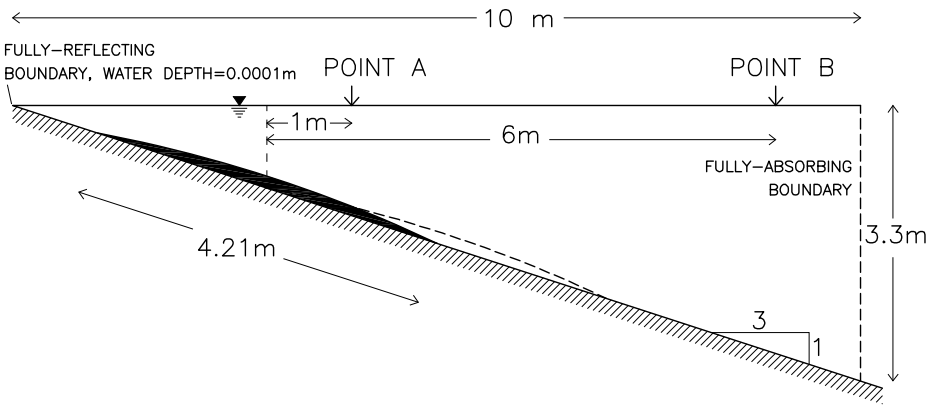

Figure 4.15: Sketch of the computational domain.

Numerical simulations were run with both the depth integrated model and the three dimensional one. The depth integrated model is applied in a one-dimensional domain, representative of the free water surface. At the left boundary ($x = 0$ m) a reflecting boundary condition is imposed, by using a very small water depth (0.0001 m). At the right boundary, the water depth is equal to 3.3001 m and the waves are allowed to exit the domain, by applying the radiation condition (3.34). The numerical simulations reproduce a time series of 100 s, using a Δt of 0.1 s, as in the previous experiments. The field equation is solved for same 200 angular frequencies, in the range of $2\pi \cdot 10^{-2} \leq \omega \leq 2\pi \cdot 2$. The maximum distance between the computational

nodes is again of 0.04 m, therefore the same DOF as in the constant depth simulations are solved.

The three dimensional model, based on the Laplace equation (4.2) is solved in a two dimensional domain which covers the fluid field represented in the sketch of figure 4.15. The imposed boundary conditions are: a fully reflecting condition at the left boundary ($x = 0$), where a small water depth is imposed as for the depth integrated model; a radiation condition along the right boundary ($x = 10\ m$); then at the free surface the equation (4.3) is applied, which combines the dynamic and kinematic conditions, while at the bottom boundary the wave generation condition (4.4) is imposed. The same component of the wave spectrum of the depth integrated model are solved. The finite element grid is composed of triangular elements, with the maximum distances between the nodes of 0.04 m, as for the depth integrated model. Here the DOF= 15135 and the computational time for the solution of the 200 frequencies is about 130 s.

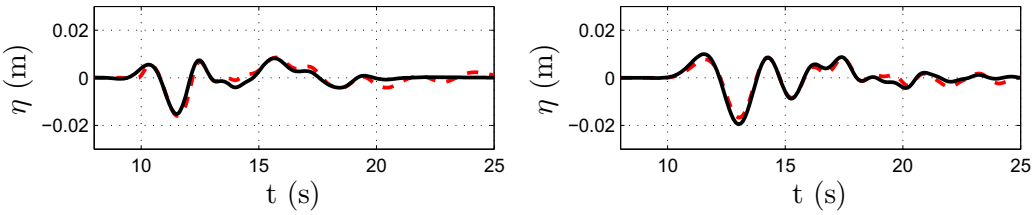

Figure 4.16: Comparison of the free surface elevation obtained from the three dimensional model (dashed red line) and that obtained from the depth integrated model with the frequency filter function (continuous black line). The presented results are relative to the points A (left panel) and B (right panel) of figure 4.15.

The figure 4.16 presents the results of the numerical simulations in terms of surface elevation obtained with the depth integrated model (continuous black line) and the three dimensional one (dashed red line). The left and the right panels refer to the results at point A and B, where the water depth is about 1.6 m and 3.3 m respectively. Also in this case the results of the two models appear to be in very good agreement. It is confirmed that the source term which reproduces the seafloor movements effects at the free surface has

to be function of the wave frequency.

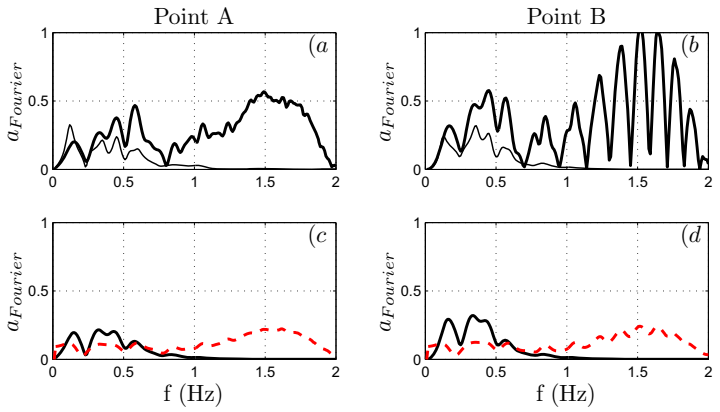

Figure 4.17: Panels a and b: absolute values of the Fourier transform coefficients of the water surface elevations, computed with the three dimensional model (thin black line) and with the depth integrated model, without any filter function (thick black line); panels c and d: absolute values of the Fourier transform coefficients of the water surface elevations, computed with the depth integrated model, with the frequency filter (continuous black lines) and with the landslide filter function (dashed red line).

These considerations can be supported also in this case by the analysis in the frequency domain. Figure 4.17 is similar to figure 4.13, but all the panels are representative of the same simulation with the long landslide. Here the left panels (a and c) refer to results picked up at the point A (water depth $\approx 1.6\ m$), while the right panels (b and d) refer to the results at point B (water depth $\approx 3.3\ m$). In the top panels (a and b), the thin black lines represent the reference amplitude spectra achieved with the three dimensional model, and the thick lines those obtained without using any filter in the depth integrated model. The bottom panels (c and d) show the amplitude spectra obtained applying the MSE with the source term filtered by the wave frequency filter (solid black lines) andthe landslide filter (dashed red lines). It is evident that the landslide filter predicts smaller long wave components and larger short waves than the desired ones, while the wave frequency filter is able of predicting the expected attenuation for each component of the wave field.

4.4 Landslide generated waves along a straigth beach

This section describes the results of numerical and physical experiments, which reproduce tsunami generated by landslide partially submerged, which falls down a sloping straight beach. The analysis of the generated wave field is given with particular attention to the propagation close to the shore. Three dimensional physical experiments, performed at the LIAM laboratory of L'Aquila University, Italy, are described in details in the paper of Di Risio et al. (2009a). The wave tank has dimensions in plan of 10.8 m in the long-shore direction and 5.4 m in the cross-shore one, while has a maximum water depth of 0.8 m. The landslide model is a rigid body, with the shape of an half of the ellipsoid described by the equation $x^2/a^2 + y^2/b^2 + z^2/c^2 = 1$, where $a = 0.2$ m, $b = 0.4$ m and $c = 0.05$ m, for a total volume $V = 0.0084$ m^3. In figure 4.19 is reported a sketch of the landslide model in the plan view and two transverse sections. The landslide is constrained to slide down the inclined surface by means of rails. The slope of the coast is of 1/3 (1 vertical, 3 horizontal). The generated water waves are free of propagating both offshore and alongshore, since the plan dimensions of the used wave tank are of at least one order of magnitude larger than the width of the landslide, which can be considered to be a length scale of the waves propagating alongshore. The experimental study has been carried out reproducing both subaerial and partially submerged landslides. The wave generation process is studied by means of video records of the near field and measurements of the landslide movement; the properties of the waves propagating along the coast are derived on the basis of runup and water surface level gauges.

A capacitive accelerometer (Metra-Mess CB41) is placed inside the landslide. The measurement of the acceleration of this body can then be used to reconstruct, by time integration, its velocity and position in time. A video camera frames the area where the landslide enters into the water. A regular grid has been drawn on the slope in order to analyze the image sequences. The water surface elevation has been measured in the wave tank by means of traditional resistive wave gauges (resolution of 0.1 mm, noise of 0.3 mm); however the focus of the research is mostly on the run-up along the coast. In order to measure the instantaneous movements of the shoreline special wave gauges have been built by the technicians employing two steel bars (square section of 4 mm x 4 mm) directly embedded into the PVC of

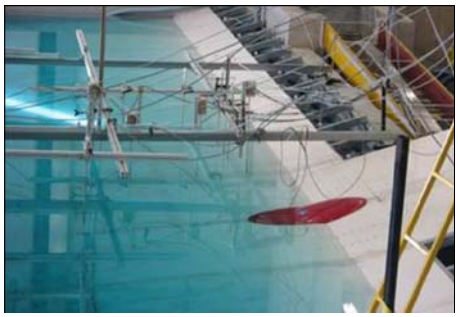

Figure 4.18: Picture of the physical model at the LIAM laboratory, L'Aquila, Italy.

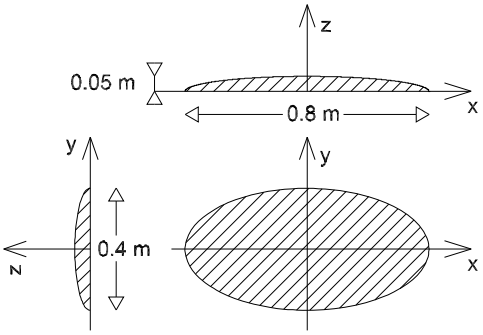

Figure 4.19: Sketch of the landslide used in the experiments.

the slope.

In the present section just one experiment, performed with a initially partially submerged landslide, is reported. Given that the problem is symmetric with respect to the cross-shore axis that passes along the centre of the landslide, only one half of the domain is reproduced numerically, in order to reduce computational costs. The computational domain used for the numerical model is 3 m in the x-direction and 5 m in the y-direction, which corresponds to a total length of the coast of 10 m. In figure 4.20 is presented a sketch of the numerical wave tank, only the left side of the landslide and of the generated waves field is modeled, and the free surface elevation results are analyzed at the gauges position points: gauge $R1$ ($y = 3.10$ m, $x = 0$) and gauge $R2$ ($y = 4.07$ m, $x = 0$).

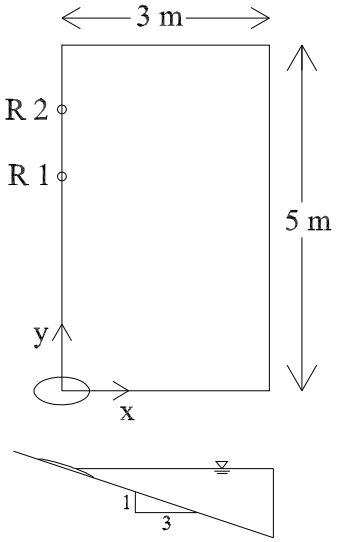

Figure 4.20: Sketch of the experimental layout of the landslide generated waves over a plane beach experiments.

The shoreline ($x = 0$) and the boundary of simmetry ($y = 0$) are simulated as a fully reflective wall, while along the external boundaries ($x = 3\ m$, and $y = 5\ m$) a radiation contidion is imposed.

The numerical model simulates a time series of 60 s, with a Δt of 0.001 s, resulting in 60,000 time steps and an equal number of frequency components to be solved. For the present application the model is solved following a 'direct' procedure. The landslide is modeled with a gaussian shape, instead of an half ellipsoide, and its law of motion is determined by a constant sliding speed on 1 m/s. By knowing the shape, the dimensions and the landslide's motion law, it has been possible to generate the function $h(x, y, t)$, which represents the variation of the sea floor, due to the landslide movements. The second derivative in time of the function $h_{tt}(x, y, t)$ is carried out using a numerical approximation and its Fourier transform is applied, in order to insert it into the field equation (3.48).

In figure 4.21 are presented the vertical free surface elevation (left panels) and the wave energy spectra (right panels) at the shore gauges $R1$ (top panels) and $R2$ (bottom panels). The red dashed lines represent the physical

model results and black solid lines those of the numerical model. An overall agreement is achieved in terms of wave height and wave period. From the free surface elevation comparison it can be recognized a first wave train, that in the numerical simulation is longer (until the 13^{rd} and 16^{th} second) followed by irregular waves (bigger for the physical experiments) which are due to wave reflection. The first wave crest is slightly underestimated by the numerical model, this could be due by having approximated a gaussian landslide model, which enters into the water more smoothly.

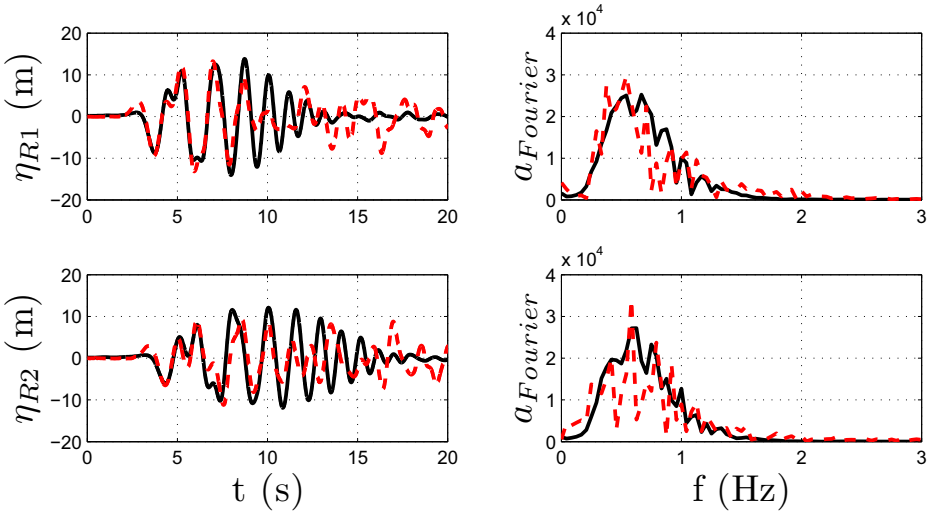

Figure 4.21: Comparison of the experimental data (red dashed line) and the numerical one (black solid line)

From the wave energy spectra (right panels) it can be noted that the peak frequency is about 0.5-0.6 Hz, corresponding to a peak period of about 1.5-2 s, and that the most part of the wave energy content is distributed along frequencies smaller than 3 Hz. Thus the numerical model was run just for frequencies up to 3 Hz.

The same results of the numerical model are now compared with the results of the analytical model of Sammarco & Renzi, (2008). In their model the landslide shape and kinematics is equal to the numerical one, but the wave propagation is approximated with the shallow water theory. The figure 4.22 shows the free surface elevation estimated with the analytical model (thin black lines) and with the numerical one (thick black lines).

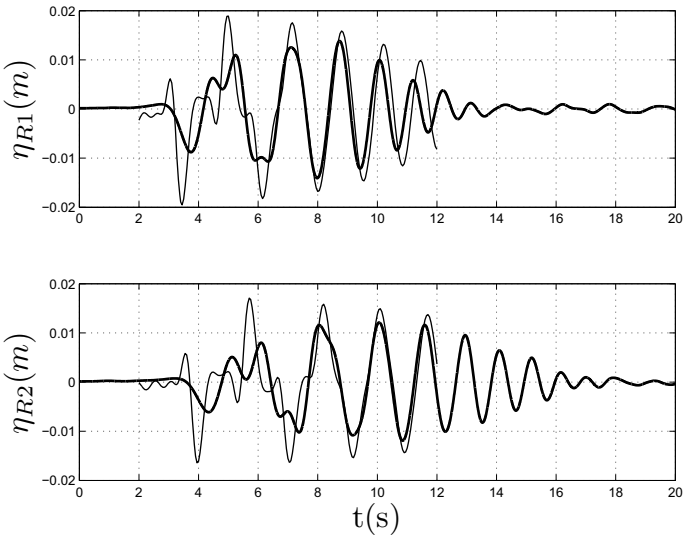

Figure 4.22: Comparison of the numerical data (thick black line) and the analytical solution one (black thin line)

The general properties of the wave field are predicted with satisfactory accuracy by both mathematical models. Quantities of fundamental engineering insterest such as the maximum elevation are very well reproduced. The biggest difference in the comparison of figure 4.22 appears in the first incoming wave, which is overestimated in the analytical model based on shallow water equations.

4.5 Landslide generated waves around a conical island

Further physical experiments which aims at studying the tsunami wave field generated by landslide have been carried out in a large wave tank at the Research and Experimentation Laboratory for Coastal Defence (LIC) of the Technical University of Bari, Italy, in cooperation with the Environmental and Maritime Hydraulics Laboratory Umberto Messina (LIAM) of the University of L'Aquila, Italy. They simulate landslide body falling on the flank of a conical island. The conical island was built in order to approximatly

reproduce in scale 1:1000 Stromboli island, south Tyrrhenian Sea, Italy (Tinti et al., 2006b). As mentioned in the Introduction Stromboli is a volcanic island, that was interested by landslide dislocations which falling into the sea, provocates tsunami waves, dangerous especially for the island shoreline. Most of the tsunamis studies pose attention to the wave propagation and the inundations of the coasts ahead the landslide/earthquake which generate it. The case when the tsunami is generated close to a small island needs of detailed analysis for the wave field entrapped close to the shoreline. Two different wave pattern are generated when aerial or partially submerged landslides impact the sea water surface: one which propagates toward the direction of the landslide motion and has circular fronts, the other which is entrapped close to the shoreline, i.e. around the island.

The physical model results have been used to validate the numerical model, in terms of results reliability and application's methods, and to further comprend and characterize the phenomena.

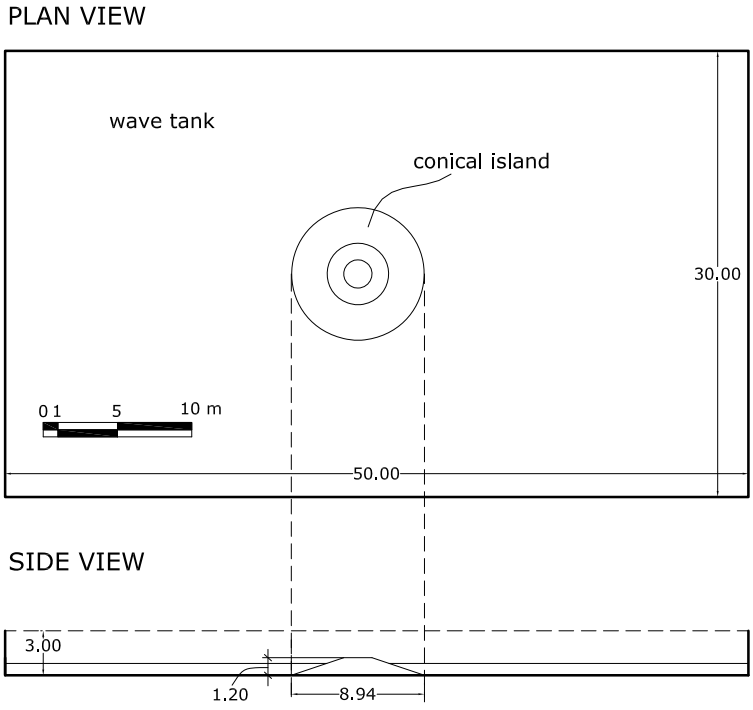

Figure 4.23: Sketch of the layout of the conical island experiments.

More details about the experiments can be found in the paper of Di Risio et al. (2009b). The physical model consist in a wave tank, 30.00 m wide, 50.00 m long and 3.00 m deep; at the center of the tank is placed a conical island, built using PVC sheets (thickness 0.01 m) and sustained by a steel frame, with a radius of 4.47 m at the tank bottom level. The slope of the flanks of the island is 1/3 (1 vertical, 3 horizontal). By varying the water depth it has been possible to study the waves propagation around islands with different shoreline curvature radius: three radius of the circular shoreline, 2.07 m, 2.20 m and 2.60 m, have been used, corresponding to three values of water depth, 0.80 m, 0.76 m and 0.62 m respectively.

The figure 4.23 shows a plan and side view of the physical model. While figure 4.24, taken from the paper of Di Risio et al. (2009b), shows three pictures of the island and landslide model on the top, and the island during its construction and an overall view of the water tank in the bottom pictures.

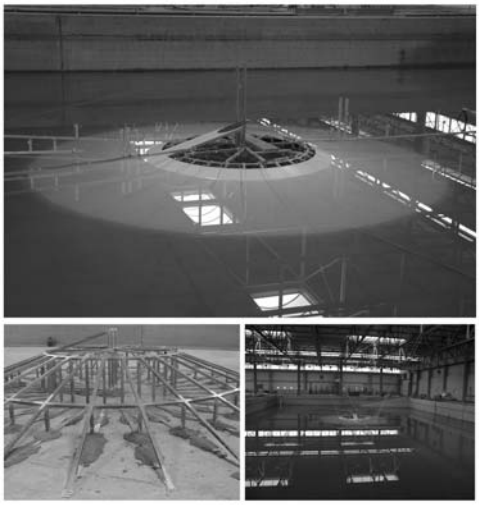

Figure 4.24: Pictures of the conical island experiments. Figure taken from the paper of Di Risio et al. (2009b)

The landslide model is the same of that used for the plane beach experiments performed at LIAM laboratory and described in the previous section (see figure 4.19). The landslide falls along the flank of the island and is constrained to move on rails placed along the slope; it therefore moves

exactly along a specified line. The landslide motion was measured as in the experiments of the sloping plane beach, previously described.

The instantaneous displacements of the shoreline have been measured by means of 20 special wave gauges that have been built employing two steel bars (square section of 4 mm x 4 mm) directly embedded into the PVC of the slope, as in Di Risio et al. (2009b). Traditional resistive gauges were employed to register the instantaneous vertical displacement of the free surface. All the signals have been acquired simultaneously at a frequency of 1000 Hz. The exact position of all the gauges can be found in the figure 4.25 and in the tables 4.2 and 4.1.

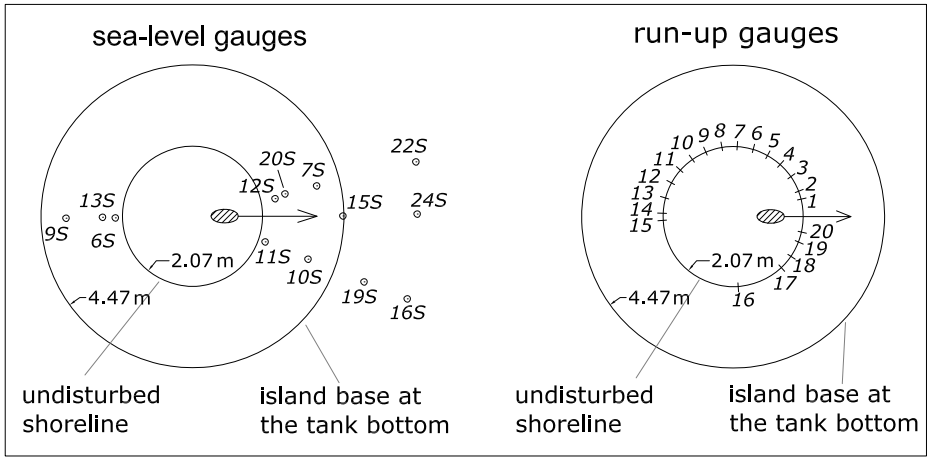

Figure 4.25: Layout of sea-level and run-up gauges position

The numerical computations have been carried out on a two-dimensional domain, sketched in figure 4.26. The numerical simulations here presented reproduces just one experimental case, defined by the off-shore constant water depth of 0.80 m, and the consequently shoreline radius of 2.07 m, and characterized by a landslide falling distance from the undisturbed shoreline of $\zeta = 0.30$ m. In order to save computational costs, not all the wave tank was numerically reproduced: the domain is circular around the island up to 8.00 m from the island center; only half of the circular domain is reproduced given the simmetry of the problem (see figure 4.26).

At the internal circular border (the undisturbed shoreline) the reflection condition is imposed with equation (3.32). Along the external circular

Gauge name	Angular position θ (°)	Radial position r (m)
15S	-0.1	4.44
24S	0.6	6.62
12S	11.8	2.49
20S	13.5	2.80
7S	13.7	3.76
22S	13.7	6.78
11S	-19.5	2.27
10S	-20.5	3.64
19S	-20.9	5.42
16S	-21.0	6.78
6S	181.3	2.27
13S	180.8	2.65
9S	180.9	3.72

Table 4.1: Radial and Angular position of Sea Level gauges

Gauge name	Angular position θ (deg)	Gauge name	Angular position θ (deg)
1R	14.5	11R	138.6
2R	20.6	13R	164.6
3R	34.3	14R	176.8
4R	47.6	15R	-176.9
5R	60.2	16R	-85.7
6R	72.9	17R	-46.5
7R	86.3	19R	-20.9
8R	98.7	20R	-12.8
10R	125.2		

Table 4.2: Angular position of Runup gauges

boundary the waves are allowed to freely exit the computational domain by imposing equation (3.34). The landslide falls down in the direction of the right-bottom border, in figure 4.26. At that boundary the fully reflection condition (3.32) is imposed in order to take into account of the symmetric half of the domain not simulated. On the contrary at the opposite boundary a radiation condition (3.34) was used, even if as well this boundary falls in the axis of symmetry of the problem. More words need to be spent for this condition, applied in order to avoid numerical errors due to the waves entrapments. Indeed it should be kept in mind that, when solving partial differential equations using the discrete Fourier Transform, the solution is obtained for a finite time interval, and it is assumed that the solution is

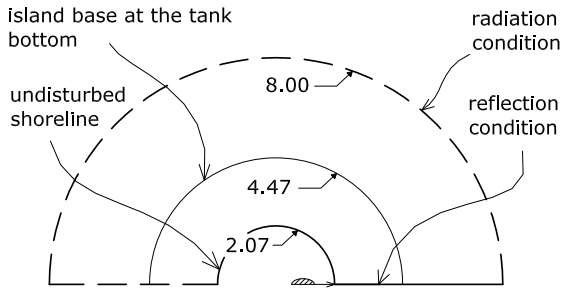

Figure 4.26: Numerical domain of the frequency-dispersive model. The numbers 2.07, 4.47 and 8.00 express the radii in meters of the undisturbed shoreline of the island base at the tank bottom and of the external circular boundary respectively

periodical over that time interval and it repeats identically over the following and the preceding time. Therefore the selected time interval should be long enough to allow all the waves to exit the computational domain trough the open boundaries before the time interval ends. Otherwise interference between wave energy coming from different time intervals is obtained. In the laboratory experiments the edge waves remain partially trapped around the conical island (Renzi & Sammarco, 2010) and they slowly radiate toward offshore. Furthermore in the numerical simulations there is no energy dissipation, thus even using a very long simulation time some waves still would remain trapped around the island. Thus a radiation condition is imposed at that boundary to allow all the wave energy to leave the domain at the end of the computation, and thus provide to the following one zero initial conditions everywhere, as desired. Of course this induces the loss of the effect of the waves that from the non reproduced half of the island would have propagate in the clock-wise direction. Regarding the numerical reproduction of the generation process, here reference is made of both the procedure described in section 3.2. In the following two subsetions are shown the results obtained when simulating the wave generation by means of a wave-maker boundary condition ('indirect' procedure) and by means of an added

source term in the MSE ('direct' procedure).

4.5.1 Waves generation with the 'indirect' procedure

Here is presented the numerical model applied following the 'indirect' procedure to estimate the waves source term. The idea is to see how the model calculates the tsunami, when a registration is available to determine the waves source. As it will be discussed, the tsunami forecast depends on the position of the wave registration available. In particular the laboratory measurements at two different gauges are tested as they would be the real registration of a tsunami wave. These two gauges are respectively the $12S$ and the $15S$, one located close to the generation area, the other far away of it. The different tsunami fields calculated are discussed in the following. When building a tsunami early warning system is important to determine a priori where to locate the monitoring instruments, because the measurements are a key input parameter for the forecasting model. This implies the knowledge of the tsunamogenic source position, that in most of the cases is easy to hypothesize realistically. Knowing the landslide width and its motion from the physical experiments, it is possible to define the arc of the shoreline where the landslide impacts the water. Therefore a wave maker condition (3.38), which moves that boundary with a generic velocity is here imposed and the problem is solved for all the wave frequencies. The solution of the water surface elevation, $N'(x, y, \omega)$, in the frequency domain is saved at the positions of all the wave gauges. The apices means that the solution is obtained for a unitary source term. In order to estimate the wave field due to the landslide movement, use is made of the physical registration of the water surface elevation time series at one point, i.e. gauge position. The simulation reproduces a time series of 50 s, using a Δt of 0.01 s, thus corresponding to 5,000 time steps and equal number of wave frequencies to solve. In order to save computational costs, it is verified that the wave energy is mostly concentrated in the range of frequencies of $0.02 \leq f \leq 2\ Hz$, thus just 100 frequencies are solved. The numerical simulation has been carried out using triangular linear elements. The maximum elements size is set as 0.05 m, as one tenth of the shortest wave length simulated, since a resolution of 10 nodes per wave length is required. The resulting Degrees of Freedom are 80,970 for a computational time of about 20 s on a AMD Opteron 246 2GHz computer equipped with 4GB of RAM. Since the elliptic MSE is solved in the present simulation for 100 wave frequencies, the total computational time is about

half an hour.

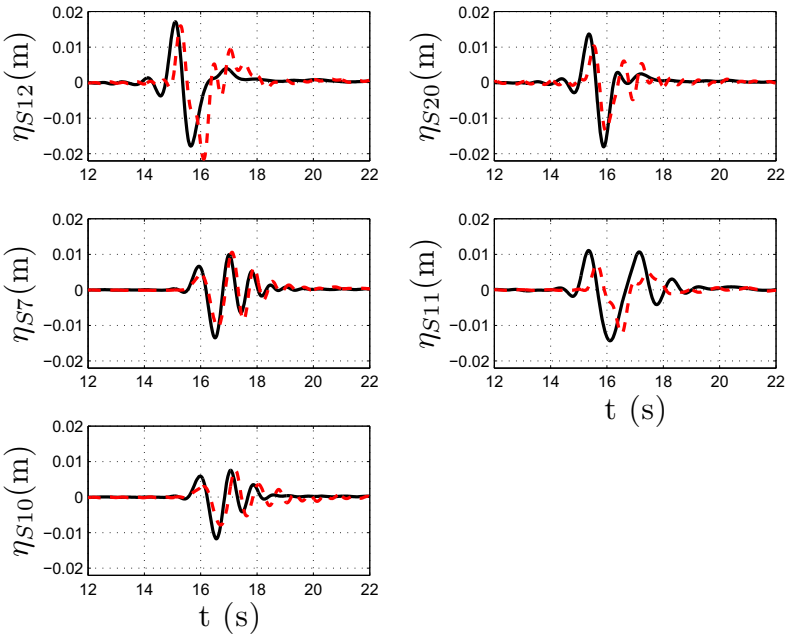

Figure 4.27: Comparison of the free surface elevations at the near field gauges position, measured (red dashed line) and obtained from the numerical model (black solid line). The numerical results are achieved by using the registration of the free surface elevation at the gauge $15S$ to estimate the wave source term.

The first comparison results (figures 4.27, 4.28 and 4.29) refer to the numerical computations obtained by using the registration at the sea level gauge $15S$ to 'indirectly' estimate the source term and consequently solve the wave field. In particular the figures refer only to the water surface elevation time series at the 13 sea level gauges (see table 4.1). A distinction is made between 5 gauges ($12S$, $20S$, $7S$, $11S$ and $10S$) which are located in front of the landslide movement and close to the island; 5 other gauges ($15S$, $22S$, $24S$, $19S$ and $16S$) placed far from the island, all in the off-shore region, i.e. water depth of 0.80 m; and the last 3 gauges ($6S$, $13S$ and $9S$) located at the rear side of the island with respect to the landslide movement. The figures 4.27, 4.28 and 4.29 refer respectively to these three groups of sea level gauges. In all the following figures the red dashed lines represent the experimental

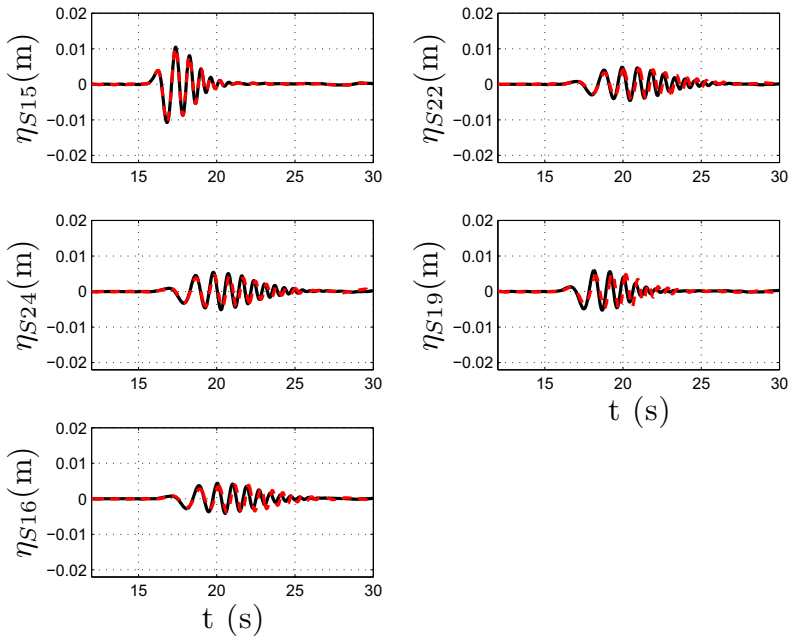

Figure 4.28: Comparison of the free surface elevations at the far field gauges position, measured (red dashed line) and obtained from the numerical model (black solid line). The numerical results are achieved by using the registration of the free surface elevation at the gauge $15S$ to estimate the wave source term.

measurements, while the black solid lines the numerical model solutions. In figure 4.27 it can be noted an overall good agreement in the comparison, but, specially for the comparison at the gauges $12S$, $20S$ and $11S$, the numerical model seems not able to reproduce exactly the experiments. This can be explained by the fact that those gauges are the ones located closer to the landslide impact and in shallower waters where the waves are generally complex and nonlinear. At these gauges it appears a wave pattern at high frequency component which are not modelled numerically (see after figure 4.30 of wave energy spectra).

Looking at the figures 4.28 and 4.29, an overall good agreement is achieved, specially in the comparisons at the gauges located in the far field (figure 4.28). About these first simulations it can be said that, when using a far field registration in order to estimate the waves source term, the wave

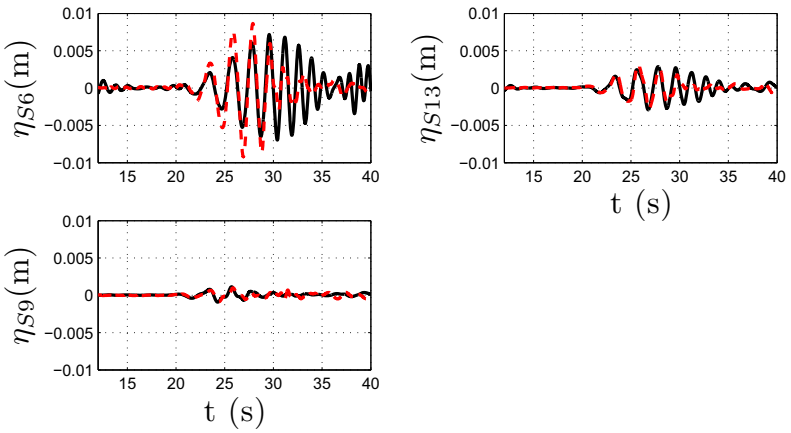

Figure 4.29: Comparison of the free surface elevations at the back field gauges position, measured (red dashed line) and obtained from the numerical model (black solid line). The numerical results are achieved by using the registration of the free surface elevation at the gauge $15S$ to estimate the wave source term.

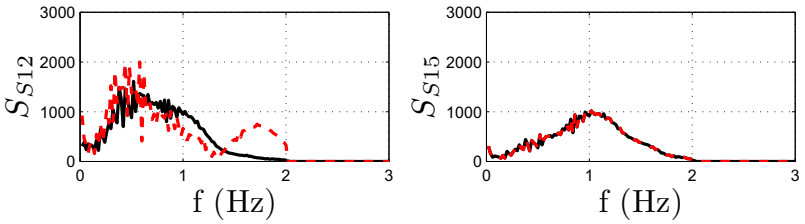

Figure 4.30: Comparison of the wave energy spectra at gauges $12S$ (left panel) and $15S$ (right panel), measured (red dashed line) and obtained from the numerical model (black solid line). The numerical results are achieved by using the registration of the free surface elevation at the gauge $15S$ to estimate the wave source term.

field produced is not able to take into account of the near field waves features. In fact the landslide motion generates two pattern of waves, one which propagates toward the direction of the landslide and has circular fronts, the other which is entrapped close to the shoreline, i.e. around the island in this

case. Thus the far field sea level gauges reproduce the more regular waves, radiating offshore, and the near field gauges measure a more complex wave field, composed by irregular and nonlinear waves.

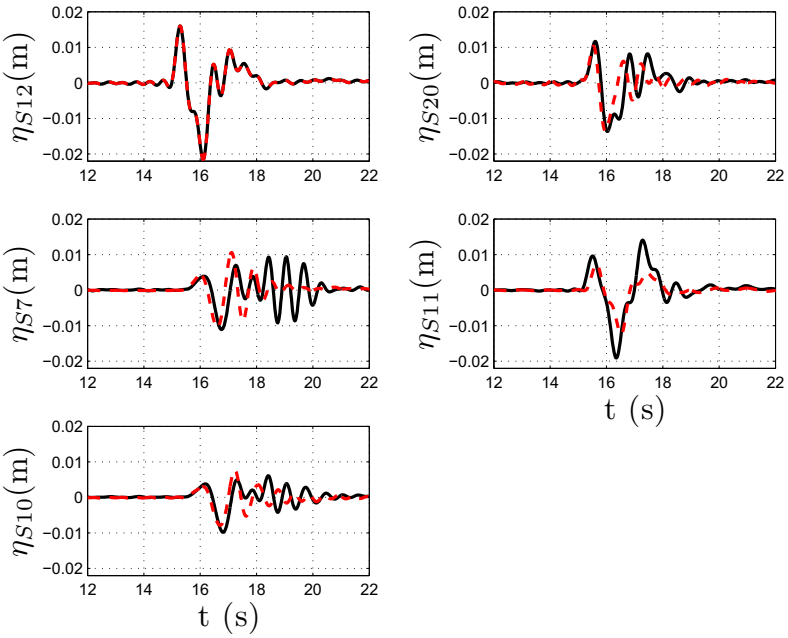

Figure 4.31: Comparison of the free surface elevations at the near field gauges position, measured (red dashed line) and obtained from the numerical model (black solid line). The numerical results are achieved by using the registration of the free surface elevation at the gauge $12S$ to estimate the wave source term.

Figure 4.30 shows the wave energy spectra for the same simulation at gauge $12S$ and $15S$. The dashed red lines again represent the energy spectra measured experimentally and the solid black one the energy spectra calculated by the numerical model. It is shown only the wave energy spectra at two gauges, choosen as representative of the wave field near and far from the generation/shallower area. From the figure it can be noted that the wave gauge $12S$ register a wave energy spectrum which presents two maxima, the higher frequency one is not simulated by the numerical model implemented as described before. As already said, only the frequencies up to 2 Hz are solved numerically, thus, as can be view by the figure 4.30, even the

experimental results are cut at that frequency in order to compare the same range of frequency. Now similar considerations can be made, when a near

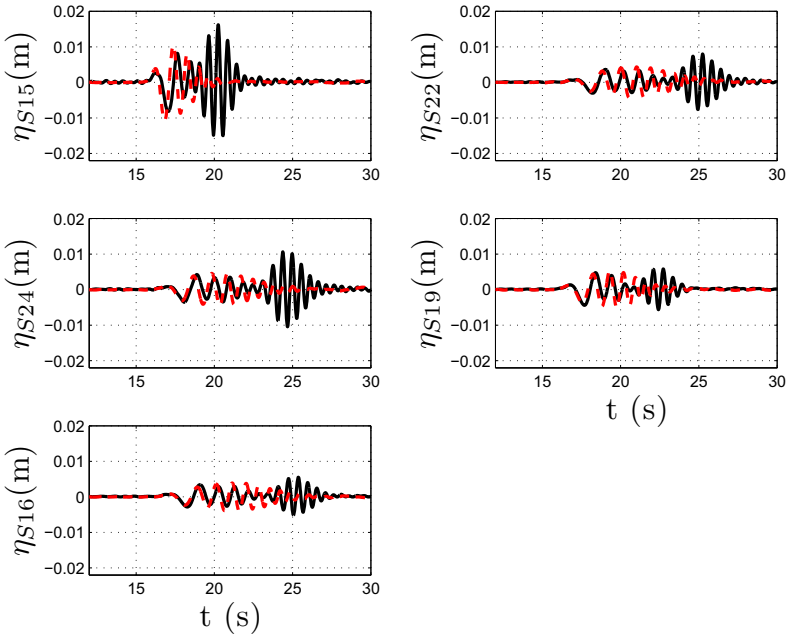

Figure 4.32: Comparison of the free surface elevations at the far field gauges position, measured (red dashed line) and obtained from the numerical model (black solid line). The numerical results are achieved by using the registration of the free surface elevation at the gauge $12S$ to estimate the wave source term.

field sea level gauge is used to determine the source term and the wave field is calculated at all the other gauges by means of the inversion technique. The laboratory registration of the free water surface elevation at the gauge $12S$ is taken as the available measurement to correct the pre-calculated unitary simulations. In the following figures, as for the previous one, the red dashed lines refer to the physical model results and the solid black lines to those of the numerical model. In figure 4.31 the comparison of the free water surface elevation is shown at the near shore gauges. The comparison at the gauge $12S$ is perfect because mathematically imposed; at the gauges $7S$ and $10S$ the numerical model reproduces a high frequency wave packet which does not compare in the physical model. Looking at the figure 4.32 this discrepancy

is even more accentuated: it is easy to distinguish a first wave train, which almost perfectly superimpose the laboratory measurement, and a second one which appears only in the numerical model results.

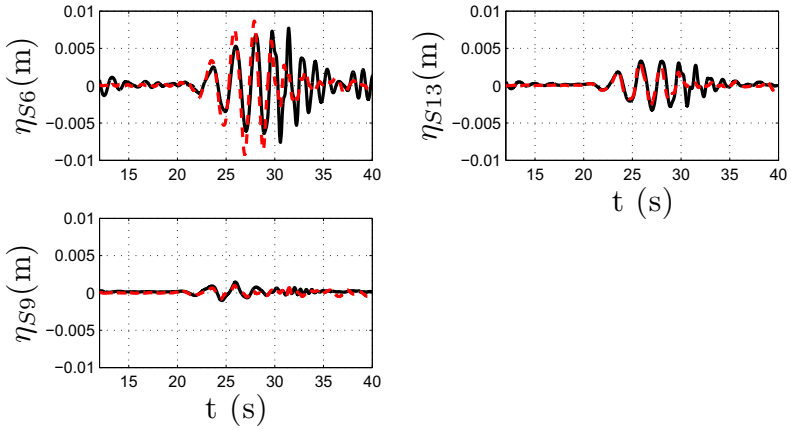

Figure 4.33: Comparison of the free surface elevations at the back field gauges position, measured (red dashed line) and obtained from the numerical model (black solid line). The numerical results are achieved by using the registration of the free surface elevation at the gauge $12S$ to estimate the wave source term.

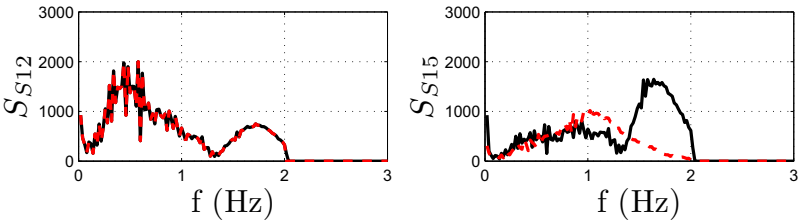

Figure 4.34: Comparison of the wave energy spectra at gauges $12S$ (left panel) and $15S$ (right panel), measured (red dashed line) and obtained from the numerical model (black solid line). The numerical results are achieved by using the registration of the free surface elevation at the gauge $12S$ to estimate the wave source term.

Comparing the model results at the gauges located in the rear side of the island (figure 4.33) it can be noted that this error is here attenuated.

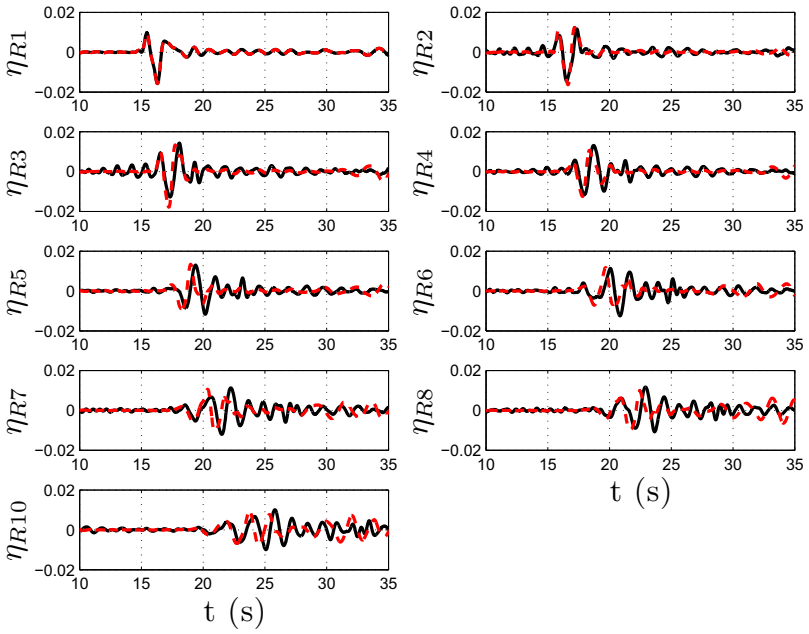

Figure 4.35: Comparison of the free surface elevations at the first 10 run up gauges position, measured (red dashed line) and obtained from the numerical model (black solid line). The numerical results are achieved by using the registration of the free surface elevation at the first run up gauge $1R$ to estimate the wave source term.

Again use is made of the wave spectra in order to analyze how the wave energy is distributed in frequency. In figure 4.34 only the results at gauges $12S$ and $15S$ are presented. Assuming that the wave energy spectra at gauge $12S$ as to be equal to that measured in the laboratory, and using this identity to estimate the wave generation term, bring to an overestimation of the wave energy in high frequency, as can be seen from the wave spectra at gauge $15S$ reproduced numerically. Therefore, using a near field measurement to estimate the correct source term for the wave field calculation, generates an error specially in the far field forecasting, because the source term will be wrongly affected by the high frequency component which are typical just of the near field close to the tsunamogenic source.

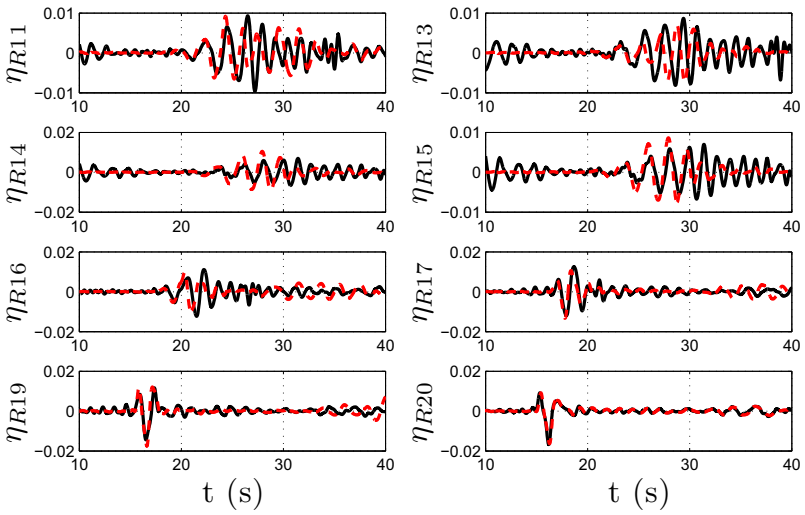

Figure 4.36: Comparison of the free surface elevations at the second 10 run up gauges position, measured (red dashed line) and obtained from the numerical model (black solid line). The numerical results are achieved by using the registration of the free surface elevation at the first run up gauge $1R$ to estimate the wave source term.

With regard to the shore inundation, the results at the run-up gauges are analyzed. The shoreline in the numerical model is simulated as a reflecting wall with a water depth of 0.0001 m, which for numerical reasons can not be equal to zero. Using the sea level registration at gauges $12S$ and $15S$ in order to estimate the run-up on the island does not produce reliable results, specially when using gauge $15S$. The shore inundation forecasting has to be carried out using water level measurements at the shoreline, or close to it. In figures 4.35 and 4.36 are shown the comparison results at the run-up gauges. Again the red dashed lines refer to the physical results and the solid black one to the numerical results. The results at the gauges $R9$, $R12$ and $R18$ are not presented, because the instruments didn't work during the laboratory experiments. At the first run-up gauge $R1$ the perfect agreement of the models results is imposed in order to estimate the source term from this identity. The numerical model seems to correctly predict the wave heigths and periods of the bigger main waves. As can be seen in the figures for all the gauge comparison, the numerical model reproduces spurios waves in

high frequency. At these gauges locations waves are relatively high compared to the water depth, therefore could not be properly reproduced using linear equations. It is worth to mention here that the numerical model does not reproduce energy disspiation due to friction at the interface of water and island flanks. This explains why in the laboratory registrations the waves are attenuated. However the model provides satisfactory results for engineering applications, where the intrest is orientated to the order of magnitude of the relevant wave features.

4.5.2 Waves generation with the 'direct' procedure

Hereinafter are described and discussed the results of the numerical model applied using the 'direct' procedure to generate waves. Therefore the effect of the landslide movement is inserted as a forcing term into the MSE. The water depth function $h(x, y, t)$, which takes into account of the sea floor motion, due to the landslide, is determined by knowing the landslide shape and movement. The second derivative in time of the function, $h_{tt}(x, y, t)$, is carried out using a numerical approximation and its Fourier transform is applied, in order to insert it into the field equation (3.48).

The domain and the boundary conditions are equal to those used for the previous simulations, except for the wave-maker boundary condition that here is not imposed anywhere. Inside the computational domain (see figure 4.26) the area where it passes the landslide, is defined as a subdomain where the MSE with the forcing term (4.8) is solved, else where the MSE (3.29) is solved. The numerical simulation has been carried out using triangular linear elements, which maximum size is 0.05 m. The resulting Degrees of Freedom and the computational costs are similar to those of the simulations described in the previous subsection. Figures 4.37, 4.38 and 4.39 show the comparison results between the laboratory measurement of the water surface elevation (red dashed lines) and numerical simulations (solid black lines). Figure 4.37 refer to the sea level gauges close to the generation area, figure 4.38 to the ones in the off-shore region and figure 4.39 to the ones in the rear side of the island with respect to the landslide. As it can be seen from the figures the model gives reliable results, this can be said expecially for the gauges located in the off-shore area (figure 4.38). The comparison shows that the model is not able to correctly reproduce the water level oscillations close to the shoreline, see the numerical results at gauges $S12$, $S11$ and $S6$ (table 4.1 shows their distance from the island center). This behaviour can be explained by the

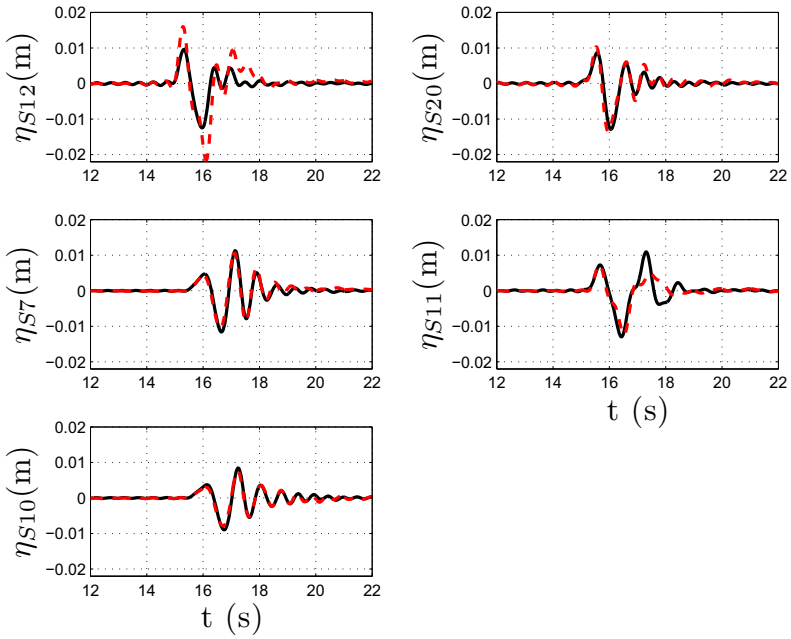

Figure 4.37: Comparison of the free surface elevations at the near field gauges position, measured (red dashed line) and obtained from the numerical model (black solid line). The numerical results are achieved imposing a forcing source term in the MSE.

fact that the numerical model equations are valid for submerged landslides, beacuse reproduce the effect of the moving seafloor on the water surface. No reproduction of the landslide entering phase is made, which, as seen in the laboratory experiment, has a piston-like effect (especially if it has a steep front), which induces a deformation of the shoreline. Another point to be considered is that the numerical model does not reproduce any dissipation at the interface between water waves and the island.

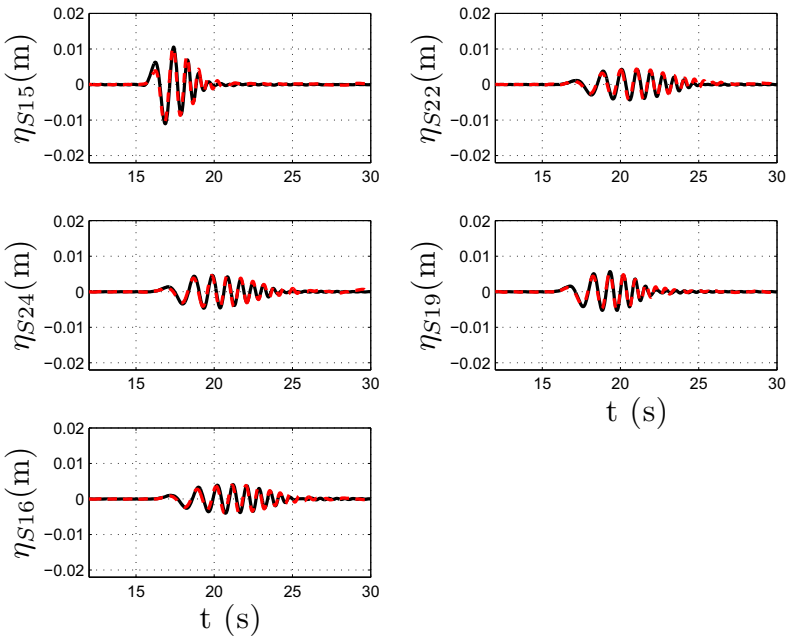

Figure 4.38: Comparison of the free surface elevations at the far field gauges position, measured (red dashed line) and obtained from the numerical model (black solid line). The numerical results are achieved imposing a forcing source term in the MSE.

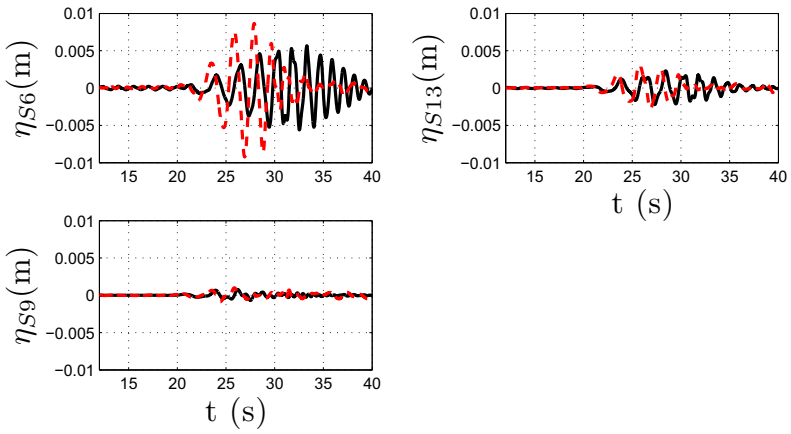

Figure 4.39: Comparison of the free surface elevations at the back field gauges position, measured (red dashed line) and obtained from the numerical model (black solid line). The numerical results are achieved imposing a forcing source term in the MSE.

4.6 Matching of elliptic and parabolic MSE - Numerical experiments

As already introduced the solution of the fully elliptic mild-slope equation for a large number of wave frequencies, is computationally very expensive, and until now has limited the application of the model over relatively small geographical areas, typically of the order of 100 km^2 (Bellotti et al., 2008). Thus the further reduction of the computational costs and the model application extension to larger geographical areas (thousand of km^2) can be achieved by solving the parabolic approximation of the MSE. It is here shown a simple numerical experiment which aims at validating the numerical model when it solves the elliptic MSE over a restricted domain and the parabolic MSE over a bounding larger domain. The experiment consists on choosing an hypotethical tsunami scenario domain, which covers the generation area and a large propagation field, and split the domain in two parts, one close to the source (near field), the other far from it (far field). In the near field is solved the elliptic MSE (equation 3.29 or 3.48), at the boundary of matching with the far field domain the solution is saved and it is given as input condition to the model which solves the parabolic MSE (3.57) in the far field. Since here

a validation test is shown, the elliptict MSE is solved in the whole domain (near and far filed), thus its solution is taken as the reference one.

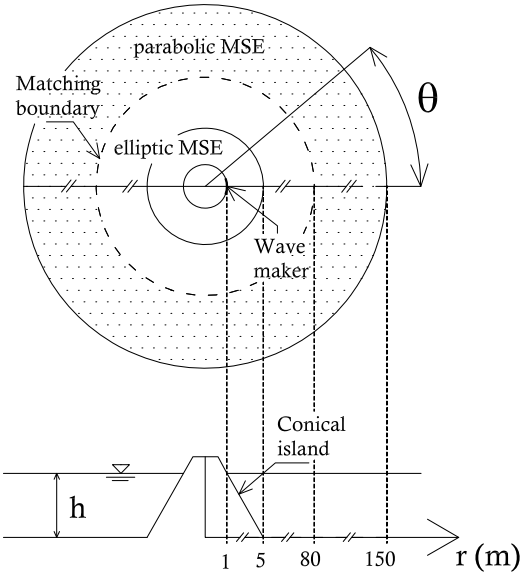

Figure 4.40: Layout of the numerical experiment aimed at validating the matching between the solution of the elliptic and parabolic MSE

The layout of the chosen numerical domain is shown in Figure 4.40. The upper sketch reproduce a planimetric view of the circular domain, where the dashed circumference is the boundary of matching between the so called near and far field. In the lower sketch a vertical section of the domain (not in scale) can be viewed and the domain dimensions are explicitly written. The generation mechanism is supposed to occur at the coast of a conical island, posed in the center of the numerical domain, as if it would represent a landslide sliding on a flank of the island and impacting the water surface. However no particular interest is given to the generation mechanism since the aim of the present experiment is to test the far field tsunami propagation. The boundary matching is posed at a distance from the generation area which is far enough to allows the generated waves (with a specified frequency) cross it everywhere perpendicularly. In the far field the parabolic MSE is solved in cylindrical coordinates (see equation B.36 in the appendix B.3). A system of reference centered in the middle of the island and covering the domain

for 360° is used to solve the MSEs in cylindrical coordinates. The reference origin $r = 0$ falls in the middle of the island, while $\theta = 0$ is in corrispondence with the center of the wave maker boundary and points toward the direction of the radiated waves.

In order to save computational time, given the model symmetry, only the upper half of the circular domain was reproduced. The elliptic MSEs are solved with the finite element method, as for the previously described experiments, and the linear elements have a maximum size of 0.5 m. The simulation which solves the elliptic MSE in the half circle of maximum radius of 150 m have around 605 kDOF and took about one minute to reproduce one wave frequency component on a AMD opteron 246 2GHz computer equipped with 4GB of RAM.

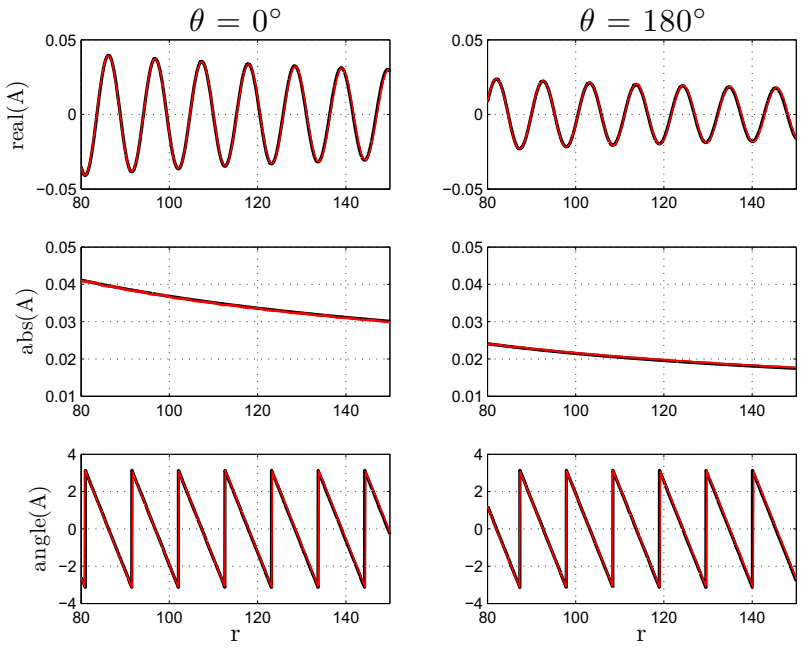

Figure 4.41: Comparison between the elliptic (black lines) and the parabolic MSE (red lines) solved for the frequency $T = 3$ s. The upper panels show the wave amplitudes, in the middle and lower panels the amplitude absolute values and phase are shown respectively. The left and right panels refer to the distance along the directions $\theta = 0°$ and $\theta = 180°$

The circular shoreline around the conical island has a radius of $1m$, here a reflection boundary condition is imposed everywhere, except that in the arc of $\pi/2$ posed between $\theta = -\pi/4$ and $\theta = \pi/4$. In this arc of circumpherence a wave maker condition is imposed, which introduces a unit source term into the numerical domain. In the external semi-circumpherence (radius of $150m$) a radiation boundary condition is imposed.

The solution of the parabolic MSE is obtained using a Crank-Nicolson finite difference numerical scheme, which proceeds marching towards increasing values of the ray r. The numerical code is written with MatLab and runs in about $5/10$ s on the same computer.

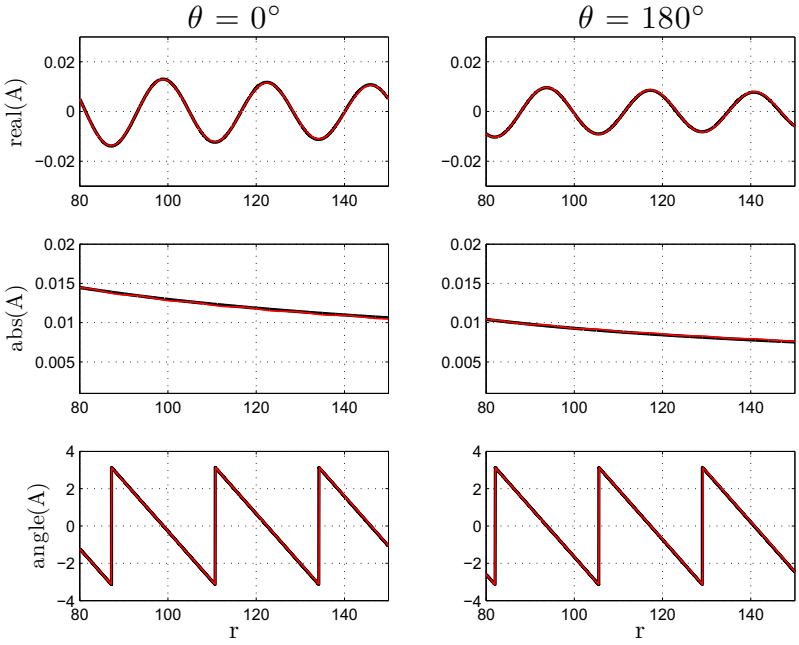

Figure 4.42: Comparison between the elliptic (black lines) and the parabolic MSE (red lines) solved for the frequency $T = 6$ s. For the notation refer to the caption of figure 4.41

The figures 4.41 and 4.42 show the results of the comparison between the solution of the MSE and its parabolic approximation for two different wave frequencies, respectively $T = 3$ s and $T = 6$ s. More frequency components and different water depths are tested and very similar comparison results were

obtained, which confirm the feasibility of the matching method. The figures show the results in terms of wave amplitude (upper panels), its absolute values (middle panels) and phase values (lower panels). The results are shown in the direction of $\theta = 0^\circ$ (left panels) and $\theta = 180^\circ$ (right panles), and are relative to the far field ($80 \leq r \leq 150$) where both elliptic and parabolie MSE are solved.

Chapter 5

Large scale model application to the Tyrrhenian Sea

5.1 Stromboli island

The Aeolian Islands are located in the south Tyrrhenian Sea to the west of Calabria and to the North of Sicily and constitute a volcanic islands arc, as it can be see in figure 5.1; Stromboli is the island located at north east of the archipelago and it is one of the most active volcanoes in the Mediterranean Sea (Tinti et al., 2003). The volcanic edifice of Stromboli is a broadly regular cone, with very steep slope: around 15 ° in the less steep submarine portion of the edifice. The volcano is characterized by a persistent activity with moderate rhythmic explosions (every 15 minutes) that are named "strombolian" by volcanologists, and by occasional more energetic paroxysmic phases also with lava effusion and fountains; pyroclastic flows occur at intervals of several years or decades. Volcanic eruptions of huge dimensions happened with a return period of thousands of years. The last episode is dated to less than 5,000 years ago, and caused the partial collapse of the edifice, creating a scar, named Sciara del Fuoco, on the north-west flank. This flank is characterized by very steep slope (38 ° in the subaerial island's portion) and thus represented a preferential lane for the lava and landslide fall, as it can be seen from the picture in figure 5.2.

The most relevant volcanic activities have been accompanied by local tsunamis. In some case the tsunamis generation is directly caused by the pyroclastic flows entering into the sea, in some others it can be caused

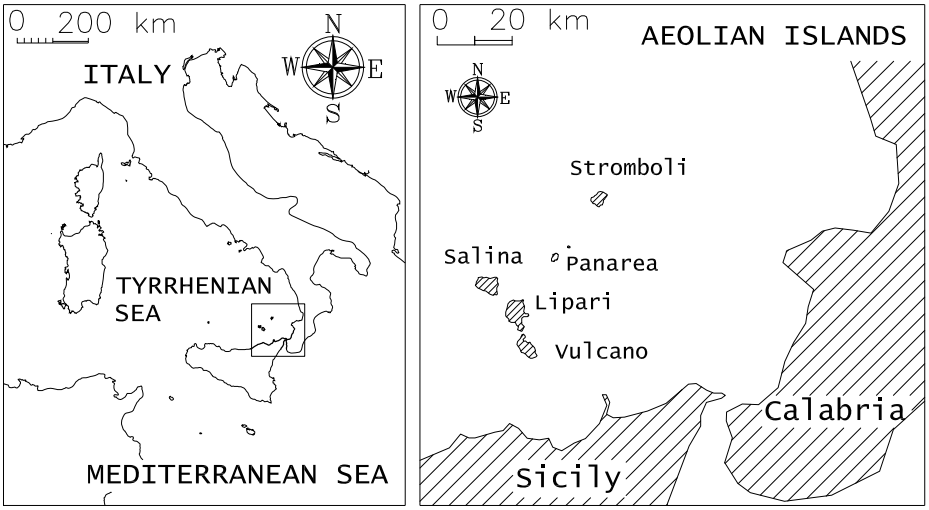

Figure 5.1: Sketch of Italy and the Aeolian islands

Figure 5.2: Picture of Stromboli island, Tyrrhenian Sea, Italy. (right picture from NE)

indirectly by the failure of aerial or underwater landslides. Accounts on tsunamis generated at Stromboli island are documented only since the last century and are associated with the largest eruptions. The most destructive tsunamis events of the last century are reviewed by Maramai et al. (2005) and

were those of 1919, 1930 1944, 1954. The generation of tsunami waves was due to submarine landslides or hot avalanches and caused several damages in the Stromboli coastal zone: inundation depth of the order of hundred meters, boats carried inland and building damages. The most recent tsunami event occurred on the 30^{th} December 2002, when two tsunamis attacked the coast of the island of Stromboli, as already introduced in the Introduction. These waves were generated by landslides that took place on the Sciara del Fuoco and caused a runup around Stromboli of the order of ten meters; for details refer to Tinti et al. (2005; 2006a).

Figure 5.3 collects 4 pictures taken the 26^{th} of February 2007, when a vulcanic eruption provocates the dislocation of a landslide, which fortunately did not generate a tsunami.

Figure 5.3: Pictures of a landslide events of 26^{th} February 2007 at the Sciara del Fuoco, Stromboli island.

It has been noted that tsunamis produced by the largest explosions of Stromboli, damaged the area close to the source (island's coast), but not the far field, where these waves arrive in form of small sea level perturbations.

However it is well recognized that Stromboli has also the potential to produce large catastrophic tsunami (return period of thousands of years), which can be the consequence of the lateral collapse of the volcanic cone. Numerical simulations of a possible catastrophic tsunamis were carried out by Tinti et al. (2003). In their work they have reproduced the collapsing of the lateral flank of Stromboli, which creates the Sciara del Fuoco slope, using a numerical model based on a lagrangian approach, and the associated tsunami generation and propagation. Assuming a landslide of about 1 km^3, the tsunami generated presents a maximum wave height in front of the Sciara del Fuoco of about 60 m, with a period of 100 s.

In the following sections some model simulations of possible tsunami scenario in the South Tyrrhenian Sea, generated at Stromboli island are presented. No detailed reproduction of the wave generation mechanism is given, because the focus of the present application is mostly on the propagation processes. Use is therefore made of the results of Tinti et al. (2003; 2006b), which on the contrary carefully modeled the landslide kinematic and its effects on the waves. The first section describes a simulation of a tsunami scenario, as the one reproduced by Tinti et al. (2003), where a wave 60 m high is supposed to occur in front of the Sciara del Fuoco, and that involves the Aeolian islands. The other section is aimed at reproducing a smaller tsunamis event, as that of 30^{th} December 2002, and testing the model as if it would work in real time.

5.2 Numerical model application to the Tyrrhenian Sea

In this research we have applied our model to simulate a Tyrrhenian tsunamis scenario caused by a landslide fall from the flank of Stromboli island. The focus of the present application is mostly on the propagation processes.

The computational domain is that enclosed into the dashed rectangle in figure 5.4. The modeled time series is 20,000 s long, with a Δt equal to 5 s, leading to 4,000 time steps, which correspond to the same number of frequencies to be solved. By inspection of the Fourier Transform of the reproduced wave field, the frequencies at which the energy content is significantly larger than zero and that consequently are worth to be reproduced are identified as those in the interval $0.00005 < f < 0.04$Hz,

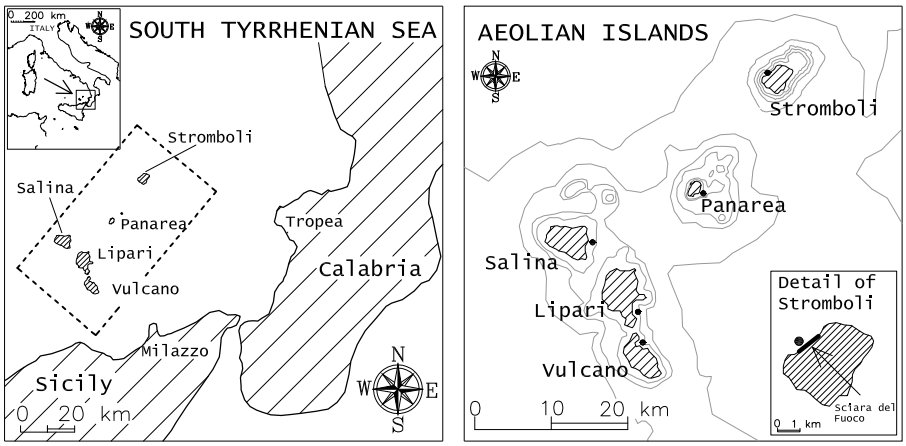

Figure 5.4: Sketch of the South Tyrrhenian Sea (Italy) and of the Aeolian islands archipelago. In the left panel with a dashed rectangle the numerical computation domain is shown, in the right panel the islands are presented in more detail together with the 5 points at which the computations results are presented.

resulting in 800 components of the spectrum. Thus 800 equations like (3.29) are solved, one for each frequency component. The computational time is in total 4 hours and 30 minutes in a AMD Opteron 246 2 GHz computer equipped with 4 GB of RAM. At the boundary of Stromboli island along the coast of the Sciara del Fuoco, a wave-maker condition as equation (3.38) is imposed, which generates a N-shaped wave with period of 100 s and height of 60 m. The boundaries of the islands are modeled as impermeable and fully-reflecting, using equation (3.32), while in the rectangular outer boundary a fully-absorbing condition (3.34) is imposed to allow the outgoing waves radiation.

The results, in term of water surface elevations in the time domain, are shown at five points in front of the five islands (see figure 5.4, right panel), all the points are located at a water depth of about 100 m.

In figure 5.5 the thick red lines represent the results of the present model, while thin black lines refer to the results of the same model solving the SWE as field equation. The comparison once again highlights the effects of reproducing or not the waves frequency dispersion. As it can be seen from the

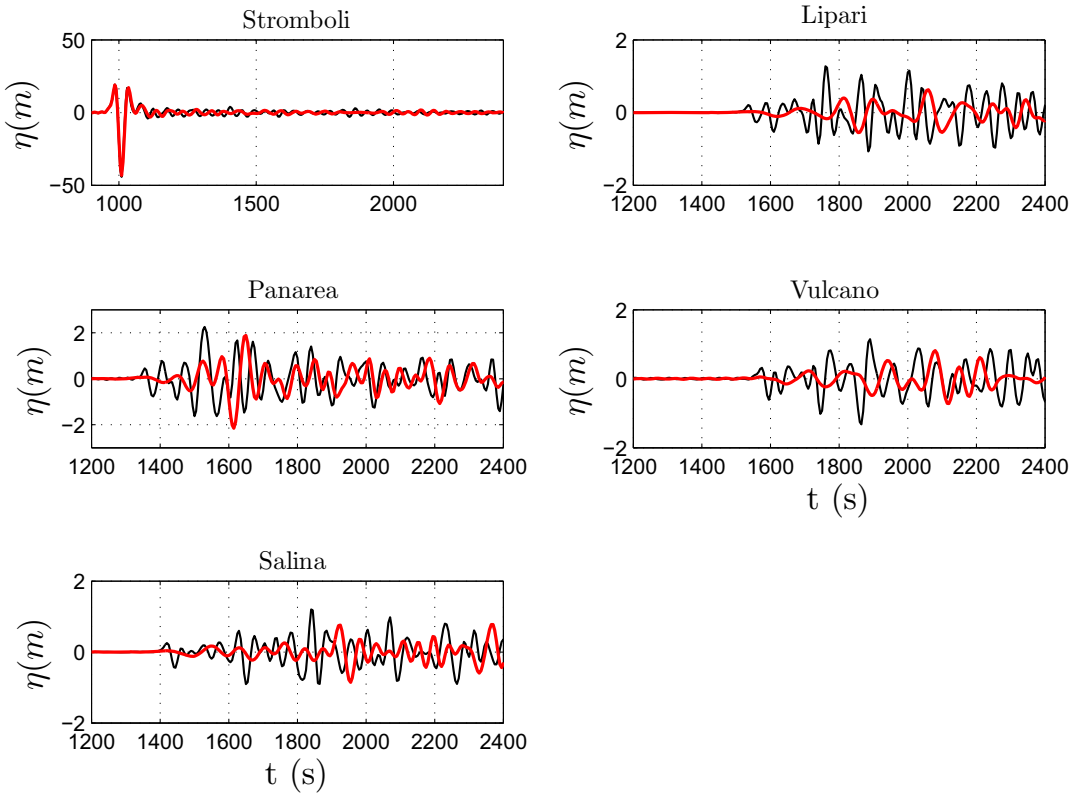

Figure 5.5: Free surface elevation calculated at the five points, sketched in figure 5.4, in front of each island. The thick red lines represent the results of the proposed frequency-dispersive model, while the thin black lines the results of the same model with the shallow water approximation.

free surface elevations, the first waves, simulated with both models, are not the highest ones. It can be noted that the two models simulate differently the wave propagation: the SWE predicts a larger surface elevation and a faster wave celerity, resulting in a earlier arrival of the highest wave. A good comparison with the results of Tinti et al. (2003) cannot be properly obtained, because the points where the results are shown are not exactly the same, and because the wave generation mechanism is different. From the plots it can be noted a strong reduction of the maximum wave height registered in front of Panarea, Salina, Lipari and Vulcano islands. Note that

the vertical scale of the plots varies. This is mainly due to the fact that the wave energy is spread into circular wave fronts as it moves away from the source.

The times of arrival of the first waves, from Stromboli to the other islands, are in good agreement with those obtained by Tinti et al. (2003). The wave which firstly reaches the island of Panarea (the closest one) arrives after about 380 s, while it takes about 430, 550 and 570 s to reach the other islands, respectively Salina, Lipari and Vulcano. Please note that the horizontal scale of the plot of Stromboli is different from the others.

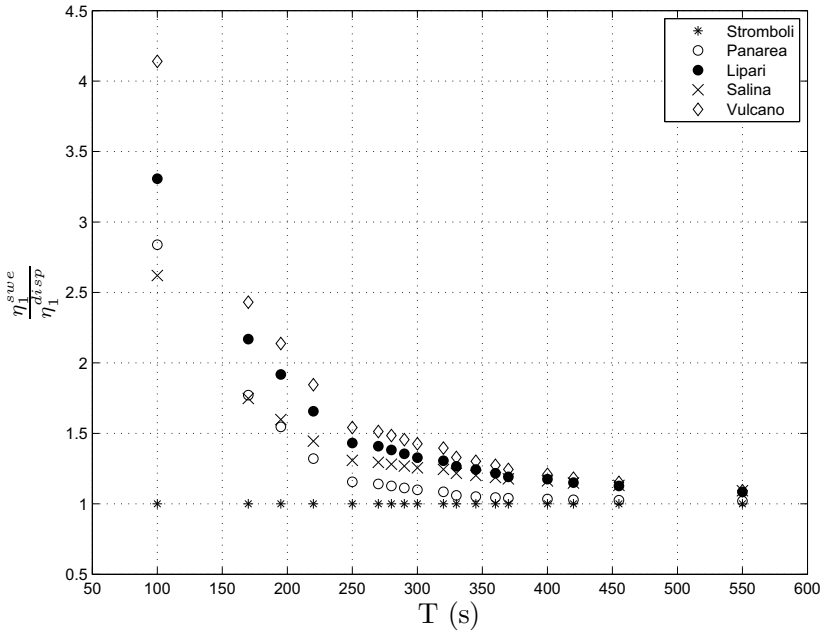

Figure 5.6: Ratio between the first wave crest height calculated with the shallow water approximation and with the frequency dispersive model versus the wave period.

Parametric computations are also carried out varying the period of the N-wave. In figure 5.6 there are highlighted the differences between the two models varying the period of the reproduced waves. The differences are expressed in term of the ratio between the maximum elevation of the first wave calculated with the non-dispersive model and that given by

the dispersive one. As expected, as the simulated waves become longer (increasing the period), this ratio assumes values close to one, while for waves with a smaller period ($100 - 200s$) it assume values between two and four, increasing as the waves propagate far away from Stromboli. It means that the SWE model gives a first wave overestimated in comparison with that from the full frequency dispersive model.

5.3 Example of Tsunami Early Warning System at Stromboli island

In this section are presented other simulations which have a closer look to the wave field generated in Stromboli and propagated offshore until it reach the closets coastline. The idea is to simulate the feasability of the model in a real time application, as if it would be used in a tsunami early warning system.

Here again the focus is just on the wave propagation and the model does not exactly reproduce one specific event, but simulates a possible tsunami scenario by using reasonable wave parameters. After careful evaluation of the conclusions of Tinti et al. (2006b) a N-wave with period of 1 min and height of 30 m is used to estimate a possible source term.

The model for this application is run using the 'indirect' procedure: first the elliptic MSE is solved for each frequency component using a unit source term at the wave-maker boundary, and the simulation results are saved in the point of interest, secondly a N-wave 1 min long and 30 m high is supposed to occur in front of Stromboli island triggered by a landslide and the source term which generates that wave is calculated by the inverse technique.

Figure 5.7 shows the computational domain used, which encloses the islands of Stromboli, Panarea and Basiluzzo. A wave-maker condition, as that expressed by equation (3.38), is imposed at the boundary of the Stromboli island along the coast of the 'Sciara del fuoco'. The boundaries of the islands are modeled as impermeable and fully-reflecting using equation (3.32), while in the circular outer boundary a fully-absorbing condition is imposed to allow the outgoing waves radiation (3.34). The modeled time series is 4,000 s long, $\Delta t = 4$ s, leading to $1,000$ time steps and frequencies to be solved. By inspection of the Fourier Transform of the considered N-wave, the frequencies at which the energy content is significantly greater

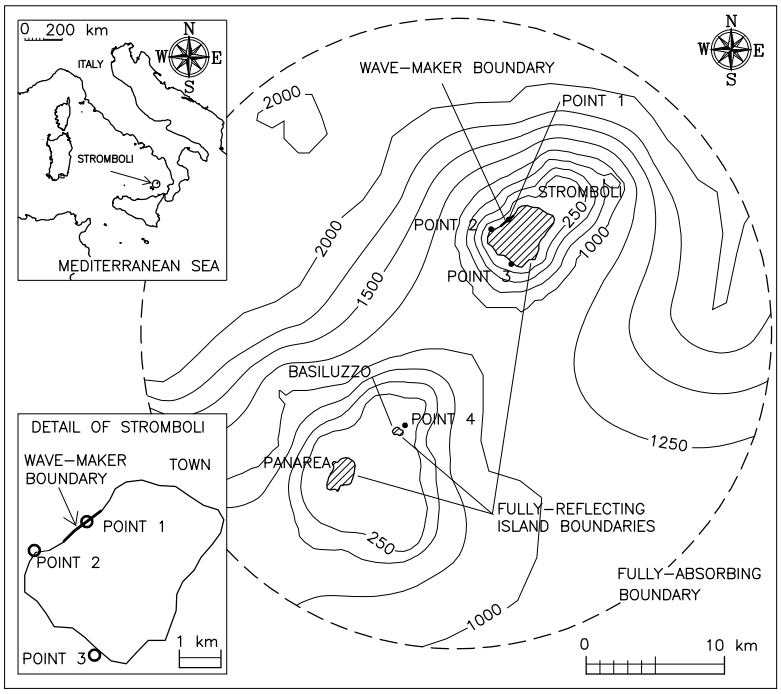

Figure 5.7: Computational domain of the Stromboli-Panarea tsunami simulations.

than zero and that consequently are worth to be reproduced are identified as those in the interval $0.00025 < f < 0.1$Hz, resulting in 400 components of the spectrum.

The computational domain is divided into three regions on the basis of the water depth; in each region a different finite element mesh is used. A coarser mesh covers the regions with water depth above 1,000 m where the maximum distance between the nodes is 350 m. In the regions with a water depth below 1,000 m a finer mesh was adopted (maximum elements length 300 m). The finest mesh (maximum elements length 100 m) covers the area with a water depth below 500 m around Panarea, Basiluzzo and Stromboli islands. With the above described computational mesh, the higher frequency component considered may be poorly reproduced in the shallower areas of the computational domain. However after careful inspection of the results it has been concluded that this had a minor effect. The total number of DOF is 416,000 and the total computational time for the solution of

the 400 elliptic equations is 4 hours, using the same computer described before. The numerical results of the overall propagation process appear in good qualitative agreement with the conclusions of Tinti et al. (2006b). The tsunami triggered by the subaerial landslide, propagates seawards with almost circular fronts. The fronts travel more slowly near the Stromboli coastline. About 4 minutes since the trigger of the tsunami, the entire Stromboli coast is under the attack of the waves, while the leading wave is about to hit the northern coast of Panarea (about 20 km South-West of the Stromboli island). The results of the computations are presented for 4 points of interest (see sketch on Figure 5.7). Point 1 is just at the wave-maker boundary. Point 2 is South-West of the generation area, in proximity of the Ginostra village, along the coast. Point 3 is about at the South corner of the island, in proximity of Punta Lena. Finally the results in proximity of Basiluzzo, 14 km away from the island are presented at point 4.

Figure 5.8 presents the numerical results in terms of water surface elevation at the four points introduced above. The fully frequency dispersive model (thick line) is compared with the linear long waves model (thin line). At the point 1 appear the sequence of crest-trough of the N-waves imposed at this point. As the distance from the 'Sciara del Fuoco' source grows, the height of the first positive wave reduces, and it appears other waves following. It can be noted at the other points 3 and 4, that the first incoming wave is not the highest. In particular at the point 4, in front of Basiluzzo Island (the most distant point from the generation area considered here) the first wave arrives for both models after about 240 s, which is consistent with the shallow water wave celerity in a constant water depth equal to the mean water depth between Stromboli and Basiluzzo (about 600 m). Here the results show significant differences between the two models: in the linear long wave theory the energy appears to be concentrated at the first incoming waves, while in the frequency dispersive model results the more dangerous waves are not the first ones.

The same simulation is now presented in a real time application, in order to show how the model would work inside an early warning system. As already introduced the model can be applied in two stages. In the first computations a tsunami scenario is reproduced assuming to known the area/boundaries of generation and here imposing a unit source term; in the second stages the water surface elevation has to be known, i.e. measured, at some point, in order to calculate the real source term and estimate the produced wave field. After the a priori tsunami simulations (i.e. unit source

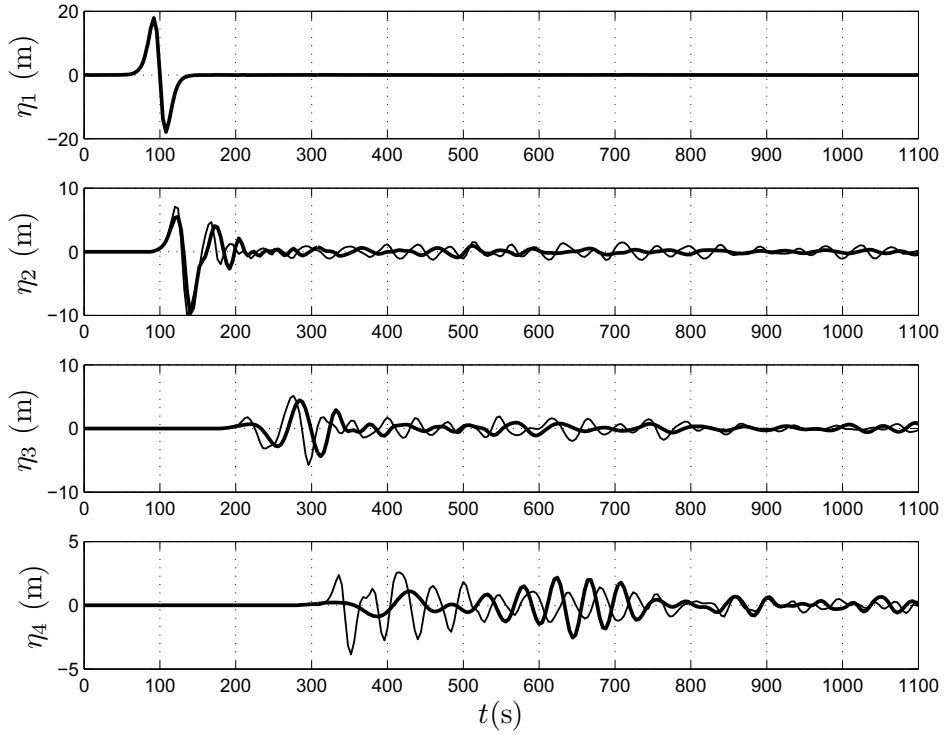

Figure 5.8: Numerical results of the Stromboli-Panarea tsunamis computations. Thick line: the present model results. Thin line: the shallow water waves model.

term computations) have been carried out, the results at the points of interest have to be obtained also for very unrealistic/noised input time series. This is important because when applying the model in real time the system should work also using truncated input time series: when a tsunami is detected by the tidal gauges, the tsunamis early warning system immediately has to forecast the wave properties at the target points. It is unrealistic, given the limited time available for spreading the warning, to wait until the tsunamis have been completely measured. It is therefore clear that as the tsunamis are measured, the available time series is to be used as input data.

The Stromboli tsunami simulation presented is here used to show the ability of the model to predict the water surface elevation at target points (i.e. points 2, 3 and 4), as the data become available at a gauge close to

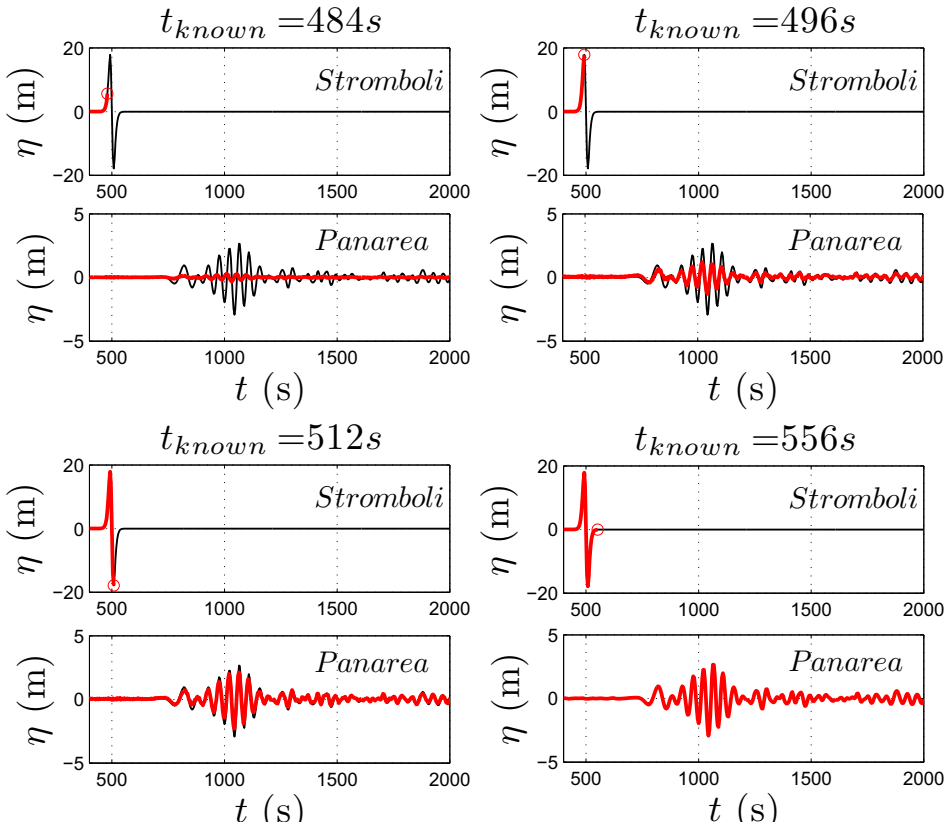

Figure 5.9: Example of application of the model using truncated input time series. Upper panels of each subplot: time series in front of Sciara del Fuoco (thick red lines represent the input data); lower panels: results in front of Panarea island (thick red lines). In each subplot the whole numerical water surface elevation time series is shown with thin black line).

the generation area (point 1). Several computations have been performed, assuming that the input time series is available up to a given time (t_{known}):

$$\eta_{input}(t) = \eta_1(t), \quad t \leq t_{known} \tag{5.1}$$

$$\eta_{input}(t) = 0, \quad t > t_{known}. \tag{5.2}$$

The results depend therefore on the value of t_{known}. Few sample results are reported in Figure 5.9, where the time series at the point 4 (named Panarea) are presented for t_{known} = 484, 496, 512 and 556 s. On the upper panel of

each subplot the input time series (η at point 1, in front of Stromboli) is represented using a thick red line, while on the lower panels it is shown the predicted η at point 4, in front of Panarea island.

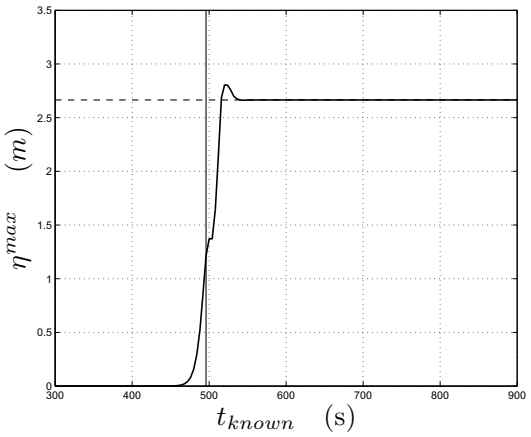

Figure 5.10: Example of application of the model using truncated input time series; maximum surface elevation in front of Panarea island (at the point 4 of figure 5.7) as the time series at Stromboli (point 1) becomes available

It is interesting to note that the use of a truncated input time series introduces very high frequency components, that are revealed by spurious short waves in the results. For t_{known}=496 s the crest of the first (highest) wave is used in the input time series and the prediction at Panarea appears to be already comparable to the final one. For t_{known}= 512 s, 3/4 of the first wave in front of Stromboli is used with very good results at Panarea. Then the results tend to those that would be obtained using the whole time series. The most important parameter predicted by the model is certainly the maximum elevation at the point 4 (Panarea), referred to as η^{max}. As the t_{known} increases the prediction tends to the final one, as shown in the figure 5.10. The vertical line in the figure represents the time at which the crest of the first wave is measured at point 1 (around $t = 500$ s). The horizontal line indicates the final value of η^{max}. It is interesting to note that due to spurious high frequency components, induced by the truncation of the input time series, for some values of the t_{known}, η^{max} may be larger than the final one. However it can be concluded that the model is able of dynamically provide estimates of the desired parameter without suffering of instabilities.

It is certainly desirable to carry out further research in the future in order to better understand if this good behavior of the model can be considered to apply under more general conditions.

Chapter 6

Conclusions

This thesis has presented a numerical model able to reproduce small amplitude transient waves. The most important feature of the model is that it is able of properly simulating the full-frequency dispersion of the waves, as other available wave theories such as the BTE. The numerical technique makes use of the Fourier Transform (with respect to the time) of the wave equation in order to obtain an elliptic equation for each component of the wave spectrum, which is solved using a numerical model based on the Finite Element Method. It is important to discuss in conclusion the role of the frequency dispersion: it is clear that the wave celerity is strongly influenced by this factor. The ability of predicting with good accuracy the celerity is of the utmost importance when estimating the arrival time of the tsunamis. However the frequency dispersion has also a further very important effect on the transient waves: it induces a decrease of the wave height, especially for the first waves of a wave packet. This is very clear in all the tests presented in this work, where the comparison of the results of the present model with those obtained using the linearized version of the NLSWE has allowed to highlight this effect. It has resulted that only due to this, the wave height predicted by the NLSWE can overestimate the actual height, for the experiments presented here, also by a factor of 2. On one hand it could be stated that the wave conditions predicted by the NLSWE are more severe than the real ones, so that safety is guaranteed. However, on the other hand, predicting tsunamis which is much more severe than the true ones, in the context of a tsunami early warning system, may lead to false alarms, which may induce the people not to trust the system, with possible catastrophic consequences.

Different validation tests have shown the capability of the model of accurately reproduce the results of laboratory experiments on tsunamis. Two methodologies are presented to generate waves inside the numerical domain: with a wave-maker boundary condition or inside the field equation. The model equation (MSE) has been derived with a source term which allows the reproduction of the seafloor movements. The source term is calculated as the time derivative of the water depth multiplied by a transfer function which depends on the generated wave frequencies. It differs from other techniques such that of Tinti et al. (2006b), who employ a transfer function based on the landslide length. Since the model equations are solved in the frequency domain, the inclusion of a frequency filter function in the source term appears natural. Anyway it is important to notice that the same approach can be easily applied to numerical models which work in the time domain, as those based on the NLSWE or the BTE. The procedure in these cases requires a previous filtering in the frequency domain of the source term, then anti-transformation in the time domain in order to provide the source term for the equations. From a physical point of view, the transfer function has the effect of a low-pass filter between the movements of the bottom and the movements of the free surface. Translating the bottom deformations directly to the free surface or by using a filter that has the same effect for all the frequencies, introduces a large amount of spurious energy in the high frequencies range, leading to unrealistic/wrong results. This effect is less evident if non dispersive equations, NLSWE, are used to reproduce the wave field, because the wave components propagate at the same celerity which is not function of the wave frequency. It is worth to remember that the technique used by Tinti et al. (2006b), although it does not consider the wave frequency dependence, has always provided good results, because it has been applied, since now, to models that do not reproduce the frequency dispersion.

It is finally worth to remember that the inclusion of a source term in the MSE has been here considered for submerged landslides. The extension of the technique discussed to subaerial landslides is to be done carefully. When a landslide enters the water it has a piston-like effect (especially if it has a steep front), which induces a deformation of the shoreline not considered by the source term used in the computations presented in this work.

A further important feature of the model is that it is suitable to be used in early warning systems for tsunamis. It has been shown that the model can be applied in two stages, in order to solve the heaviest computations in a

first stage, before the tsunami event, and to be able to solve in real time the forecasting calculations. This second part can be computed only if a tsunami wave detection is available and can be used to correct the pre-calculations of the a priori stage. It has been discussed the importance of where the tsunami is detected, i.e. where to locate tidal gauges or pressure sensors. The best solution would be to have nearshore measurements to forecast the near wave field, and even offshore measurements in order to register wave features of tsunami propagating in deep water, since the wave field generated nearshore presents a wave energy spectrum different from that of offshore wave field. Furthermore the model is suitable to be applied in real time because is very robust. After the unit source term computations have been carried out, the results at the point of interest are obtained also for very unrealistic/noised input time series. This is what happens in real time when the tsunami is deteced by tidal gauges: before the signal of the whole tsunami is measured, the model must have already forecasted the inundation field. The ability of the model to predict the water surface elevation at one target point, as the data become available at a gauge close to the generation area, has been tested in section 5.3.

In the present thesis a model application was highlighted, which is more suitable to reproduce large geographycal scale tsunami scenarios. It make use of the matching between the elliptic MSE and its parabolic approximation, which requires less computations. The elliptic MSE has the advantage of being able to reproduce diffraction and reflection, but needs heavier computations; the parabolic MSE has the advantage of being solved with lower computational costs, but is able to correctly reproduce just the undisturbed waves propagation. It appeared natural to perform a model which takes the advantages of using both equation solution, in order to be accurate and efficient. A simple numerical experiment to test this model application has been shown. When performing a similar application in a geographical domain more attention needs to be given. A few examples: the numerical solution of the parabolic MSE has to take into account when waves reach a shoreline and stop their propagation; a parabolic approximation should be solved which allows a wider wave propagation with respect to the predefined wave motion direction (see the paper of Dalrymple and Kirby, 1988).

All the numerical implementations of the model described here refer to tsunamis generated by aerial or submerged landslides; however it is important to keep in mind that the present model can be applied even to

earthquakes generated tsunamis. In those cases attention needs to be paid to a different reproduction of the generation mechanism. Normally underwater earthquakes involve the seafloor movement of a larger area, therefore a division of the seismic fault into more segments can be suggested. Since the model equations are linear, the resulting wave field can be calculated by superimposing the solutions of each scenario generated by the movement of a single segment. In view of the implementation of tsunami early warning system, pre-calculated scenarios can be constructed with the tsunamogenic source along all the faults of the sea/ocean of interest. Thus when a tsunami event occurs, its detection in more than one point, with further seismic information, can be used to determine the position of the source and its energy tranferred to the water.

Appendix A

Adimensional analysis

The goal of the adimensional analysis is to determine the relative order of magnitude of each term in the equations of the problem (2.6). This can be done by introducing a system of dimensionless variables based on the characteristic scales for the fluid motion. The independent dimensionless variables (denoted by $'$) are

$$(x, y) = L\,(x', y')\,; \qquad (z, h) = h_0\,(z', h')\,; \qquad t = \frac{L}{c_0}t' \tag{A.1}$$

where the scales used are

- L, a characteristic length scale
- h_0, a characteristic depth
- c_0, a characteristic velocity (typically the phase velocity for the waves)

This implies that differentiation with respect to these variables can be written as

$$\nabla_h = \frac{1}{L}\nabla'_h; \qquad \frac{\partial}{\partial z} = \frac{1}{h_0}\frac{\partial}{\partial z'}; \qquad \frac{\partial}{\partial t} = \frac{c_0}{L}\frac{\partial}{\partial t'} \tag{A.2}$$

The linear theory is used to express the variable η and ϕ as the product of a dimensionless quantity and a dimensional factor

$$\eta = a \cdot cos\,(kx - \omega t)\,; \tag{A.3}$$

and

$$\phi = \frac{ag}{\omega}\frac{cosh\left[k\left(h+z\right)\right]}{cosh\left(kh\right)} \cdot sin\left(kx-\omega t\right) \tag{A.4}$$

for the water surface elevation the dimensional factor can be chosen as the wave amplitude, while for the fluid velocity potential as the absolute value of the velocity potential in the shallow water condition, thus

$$\eta = a\eta' \tag{A.5}$$

and

$$\phi = \frac{agL}{c_0}\phi' \tag{A.6}$$

The mathematical problem, which describes the water motion and already defined as in (2.6), is rewritten here

$$\begin{cases} \nabla_h^2\phi + \phi_{zz} = 0 & -h\left(x,y\right) < z < 0 \\ \phi_z + h_t + \nabla_h\phi \cdot \nabla_h h = 0 & z = -h \\ \phi_z - \eta_t - \nabla_h\phi \cdot \nabla_h\eta = 0 & z = \eta \\ \phi_t + \frac{1}{2}\left(\phi_x^2 + \phi_y^2 + \phi_z^2\right) + g\eta = 0 & z = \eta \end{cases} \tag{A.7}$$

Substuituiting into this set of eqautions (A.7) the dimensionless variables and differentiation, the adimensional problem is achieved

$$\begin{cases} \frac{1}{L^2}\nabla_h'^2\phi' + \frac{1}{h_0^2}\phi'_{zz} = 0 & -h'\left(x,y\right) < z < 0 \\ \frac{L^2}{h_0^2}\phi'_z + \frac{h_0}{a}h'_t + \nabla'_h\phi' \cdot \nabla'_h h' = 0 & z = -h' \\ \frac{L^2}{h_0^2}\phi'_z - \eta'_t - \frac{a}{h_0}\nabla'_h\phi' \cdot \nabla'_h\eta' = 0 & z = \frac{a}{h_0}\eta' \\ \phi'_t + \frac{1}{2}\frac{a}{h_0}\left(\phi_x'^2 + \phi_y'^2 + \frac{L^2}{h_0^2}\phi_z'^2\right) + \eta' = 0 & z = \frac{a}{h_0}\eta' \end{cases} \tag{A.8}$$

From the dimensionless analysis three independent dimensionless parameters can be formed

- $\epsilon = \frac{a}{h}$, the amplitude parameter
- $\mu = \frac{h}{L}$, the wave length parameter
- $\alpha = \nabla_h h$, the bottom slope

Thus the problem can be rewritten as follows

$$\begin{cases} \nabla_h^2 \phi + \frac{1}{\mu^2}\phi_{zz} = 0 & -h'(x,y) < z < 0 \\ \frac{1}{\mu^2}\phi_z + \frac{1}{\epsilon}h_t + \nabla_h \phi \cdot \alpha = 0 & z = -h' \\ \frac{1}{\mu^2}\phi_z - \eta_t - \epsilon \nabla_h \phi \cdot \nabla_h \eta = 0 & z = \epsilon\eta' \\ \phi_t + \frac{1}{2}\epsilon\left(\phi_x^2 + \phi_y^2 + \frac{1}{\mu^2}\phi_z^2\right) + \eta = 0 & z = \epsilon\eta' \end{cases} \tag{A.9}$$

where in order to simplify the equations the $'$ that indicates the dimensionaless variables is omitted.

Appendix B

Parabolic MSE in cylindrical coordinate systems

B.1 MSE in conformal coordinate systems

Now it is considered the mappings of the MSE from Cartesian space (x,y) into an alternate space (u,v), where the mapping may or not may be conformal. Lets take

$$\begin{pmatrix} x \\ y \end{pmatrix} = \begin{pmatrix} x\left(u,v\right) \\ y\left(u,v\right) \end{pmatrix}, \qquad \begin{pmatrix} u \\ v \end{pmatrix} = \begin{pmatrix} u\left(x,y\right) \\ v\left(x,y\right) \end{pmatrix} \tag{B.1}$$

The mapping is presumed to be one-to-one in the domain of relevant fluid motion, and on boundaries of that domain. The first of equation (B.1) will typically be used below. From the chain of rule, the partial derivatives can be written in the following way

$$\frac{\partial \cdot}{\partial x} = \frac{\partial \cdot}{\partial u}\frac{\partial u}{\partial x} + \frac{\partial \cdot}{\partial v}\frac{\partial v}{\partial x} \tag{B.2}$$

$$\frac{\partial \cdot}{\partial y} = \frac{\partial \cdot}{\partial u}\frac{\partial u}{\partial y} + \frac{\partial \cdot}{\partial v}\frac{\partial v}{\partial y} \tag{B.3}$$

Herein for the sake of simplicity, the partial derivative is written with the subscription. The goal is that of writing the MSE (3.31) in the new system of coordinates (u,v). Here it is reminded the MSE in the cartesian coordinate system:

$$\nabla_h \left(cc_g \nabla_h a\right) + k^2 cc_g a = 0 \tag{B.4}$$

which comes from the assumption made on the free surface elevation of being time harmonic, as follows

$$\eta\left(x, y, t\right) = a\left(x, y\right) \cdot e^{i\omega t} \tag{B.5}$$

the first term of equation (B.4) can be expanded so that it yields to

$$\left(cc_g\right)_x a_x + cc_g a_{xx} + \left(cc_g\right)_y a_y + cc_g a_{yy} + k^2 cc_g a = 0 \tag{B.6}$$

The derivatives of the first order which compare in equation (B.6) become

$$\begin{array}{l} a_x = a_u u_x + a_v v_x \\ a_y = a_u u_y + a_v v_y \\ \left(cc_g\right)_x = \left(cc_g\right)_u u_x + \left(cc_g\right)_v v_x \\ \left(cc_g\right)_y = \left(cc_g\right)_u u_y + \left(cc_g\right)_v v_y \end{array} \tag{B.7}$$

For the derivatives of the second order it become

$$\begin{array}{l} a_{xx} = \left(a_x\right)_x = \left(a_x\right)_u u_x + \left(a_x\right)_v v_x = \\ = \left(a_u u_x + a_v v_x\right)_u u_x + \left(a_u u_x + a_v v_x\right)_v v_x = \\ = \left[a_{uu} u_x + a_u \left(u_x\right)_u + a_{uv} v_x + a_v \left(v_x\right)_u\right] u_x + \\ \left[a_{uv} u_x + a_u \left(u_x\right)_v + a_{vv} v_x + a_v \left(v_x\right)_v\right] v_x = \\ = a_{uu} u_x^2 + a_u u_x \left(u_x\right)_u + a_{uv} v_x u_x + a_v u_x \left(v_x\right)_u + \\ a_{uv} u_x v_x + a_u v_x \left(u_x\right)_v + a_{vv} v_x^2 + a_v v_x \left(v_x\right)_v = \\ = a_{uu} u_x^2 + a_{vv} v_x^2 + 2 a_{uv} v_x u_x + a_u \left(u_x\right)_x + a_v \left(v_x\right)_x \end{array} \tag{B.8}$$

and similarly for the second derivative in y:

$$\begin{array}{l} a_{yy} = \left(a_y\right)_y = \left(a_y\right)_u u_y + \left(a_y\right)_v v_y = \\ = \left(a_u u_y + a_v v_y\right)_u u_y + \left(a_u u_y + a_v v_y\right)_v v_y = \\ = \left[a_{uu} u_y + a_u \left(u_y\right)_u + a_{uv} v_y + a_v \left(v_y\right)_u\right] u_y + \\ \left[a_{uv} u_y + a_u \left(u_y\right)_v + a_{vv} v_y + a_v \left(v_y\right)_v\right] v_y = \\ = a_{uu} u_y^2 + a_u u_y \left(u_y\right)_u + a_{uv} v_y u_y + a_v u_y \left(v_y\right)_u + \\ a_{uv} u_y v_y + a_u v_y \left(u_y\right)_v + a_{vv} v_y^2 + a_v v_y \left(v_y\right)_v = \\ = a_{uu} u_y^2 + a_{vv} v_y^2 + 2 a_{uv} v_y u_y + a_u \left(u_y\right)_y + a_v \left(v_y\right)_y \end{array} \tag{B.9}$$

finally the first and third terms of equation (B.6) becomes

$$\begin{aligned}
&\left(cc_g\right)_x a_x = \left[\left(cc_g\right)_u u_x + \left(cc_g\right)_v v_x\right]\left[a_u u_x + a_v v_x\right] = \\
&= u_x^2 \left(cc_g a\right)_u + \left(cc_g\right)_u u_x v_x a_v + \left(cc_g\right)_v u_x v_x a_u + v_x^2 \left(cc_g a\right)_v = \\
&= a_u \left[u_x^2 \left(cc_g\right)_u + u_x v_x \left(cc_g\right)_v\right] + a_v \left[v_x^2 \left(cc_g\right)_v + u_x v_x \left(cc_g\right)_u\right]
\end{aligned} \tag{B.10}$$

and

$$\begin{aligned}
&\left(cc_g\right)_y a_y = \left[\left(cc_g\right)_u u_y + \left(cc_g\right)_v v_y\right]\left[a_u u_y + a_v v_y\right] = \\
&= u_y^2 \left(cc_g a\right)_u + \left(cc_g\right)_u u_y v_y a_v + \left(cc_g\right)_v u_y v_y a_u + v_y^2 \left(cc_g a\right)_v = \\
&= a_u \left[u_y^2 \left(cc_g\right)_u + u_y v_y \left(cc_g\right)_v\right] + a_v \left[v_y^2 \left(cc_g\right)_v + u_y v_y \left(cc_g\right)_u\right]
\end{aligned} \tag{B.11}$$

Now we are ready to write equation (B.6)

$$\begin{aligned}
&cc_g \left[a_{uu} u_x^2 + a_{vv} v_x^2 + 2a_{uv} u_x v_x + a_u \left(u_x\right)_x + a_v \left(v_x\right)_x\right] + \\
&+cc_g \left[a_{uu} u_y^2 + a_{vv} v_y^2 + 2a_{uv} u_y v_y + a_u \left(u_y\right)_y + a_v \left(v_y\right)_y + k^2 a\right] + \\
&+a_u \left[u_x^2 \left(cc_g\right)_u + u_x v_x \left(cc_g\right)_v\right] + a_v \left[v_x^2 \left(cc_g\right)_v + u_x v_x \left(cc_g\right)_u\right] + \\
&+a_u \left[u_y^2 \left(cc_g\right)_u + u_y v_y \left(cc_g\right)_v\right] + a_v \left[v_y^2 \left(cc_g\right)_v + u_y v_y \left(cc_g\right)_u\right] = 0
\end{aligned} \tag{B.12}$$

which can be rewritten as follows:

$$\begin{aligned}
&cc_g a_{uu} \left(u_x^2 + u_y^2\right) + cc_g a_{vv} \left(v_x^2 + v_y^2\right) + 2cc_g a_{uv} \left(u_x v_x + u_y v_y\right) + \\
&+cc_g \left(a_u \nabla^2 u + a_v \nabla^2 v\right) + cc_g k^2 a + \\
&+a_u \left(cc_g\right)_u \left(u_x^2 + u_y^2\right) + a_u \left(cc_g\right)_v \left(u_x v_x + u_y v_y\right) + \\
&+a_v \left(cc_g\right)_v \left(v_x^2 + v_y^2\right) + a_v \left(cc_g\right)_u \left(u_x v_x + u_y v_y\right) = 0
\end{aligned} \tag{B.13}$$

the first and the sixth terms of equation (B.13) can be assembled as the second and the seventh, yielding to

$$\begin{aligned}
&\left(u_x^2 + u_y^2\right)\left(cc_g a_u\right)_u + \left(v_x^2 + v_y^2\right)\left(cc_g a_v\right)_v + cc_g k^2 a + \\
&\left(u_x v_x + u_y v_y\right)\left[a_u \left(cc_g\right)_v + a_v \left(cc_g\right)_u + 2cc_g a_{uv}\right] + cc_g \left(a_u \nabla^2 u + a_v \nabla^2 v\right) = 0
\end{aligned} \tag{B.14}$$

while the derivatives of a above are taken with respect to the mapped coordinates (u, v), the coefficients of the derivatives still involve the

derivatives of u and v with respect to x and y. To change this, the chain rule derivative operator for x to the elemental lengths dx and dy is applied,

$$\begin{aligned} x_u u_x + x_v v_x &= 1 \\ y_u u_x + y_v v_x &= 0 \end{aligned} \tag{B.15}$$

this set of linear equations is easily solved for u_x and v_x

$$\begin{aligned} u_x &= \tfrac{1}{J} y_v \\ v_x &= -\tfrac{1}{J} y_u \end{aligned} \tag{B.16}$$

Where $J = x_u y_v - x_v y_u$ is the Jacobian of the transformation. Using the y derivative operator aplied to dx and dy results in

$$\begin{aligned} u_y &= -\tfrac{1}{J} x_v \\ v_y &= \tfrac{1}{J} x_u \end{aligned} \tag{B.17}$$

Thus in equation (B.14) some terms can be replaced as follows

$$\begin{aligned} &u_x^2 + u_y^2 = \tfrac{1}{J^2}\left(x_v^2 + y_v^2\right); \qquad v_x^2 + v_y^2 = \tfrac{1}{J^2}\left(x_u^2 + y_u^2\right); \\ &u_x v_x + u_y v_y = \tfrac{1}{J^2}\left(-y_u y_v\right) + \tfrac{1}{J^2}\left(-x_u x_v\right) = -\tfrac{1}{J^2}\left(x_u x_v y_u y_v\right) \end{aligned} \tag{B.18}$$

thus equation (B.14) becomes

$$\begin{aligned} &\left(x_v^2 + y_v^2\right)\left(cc_g a_u\right)_u + \left(x_u^2 + y_u^2\right)\left(cc_g a_v\right)_v + \\ &- \left(x_u x_v + y_u y_v\right)\left[a_u \left(cc_g\right)_v + a_v \left(cc_g\right)_u + 2cc_g a_{uv}\right] + \\ &J^2\left[k^2 cc_g a + cc_g\left(a_u \nabla^2 u + a_v \nabla^2 v\right)\right] = 0 \end{aligned} \tag{B.19}$$

By calling

$$\begin{aligned} x_v^2 + y_v^2 &= \alpha; \\ x_u^2 + y_u^2 &= \beta; \\ x_u x_v + y_u y_v &= \gamma; \end{aligned} \tag{B.20}$$

equation (B.19) can be rewritten in a more compact way

$$\begin{aligned} &\alpha\left(cc_g a_u\right)_u + \beta\left(cc_g a_v\right)_v - \gamma\left[a_u \left(cc_g\right)_v + a_v \left(cc_g\right)_u + 2cc_g a_{uv}\right] + \\ &J^2\left[k^2 cc_g a + cc_g\left(a_u \nabla^2 u + a_v \nabla^2 v\right)\right] = 0 \end{aligned} \tag{B.21}$$

Now $\nabla^2 u$ and $\nabla^2 v$ do not depend on x and y, $\nabla^2 u = u_{xx} + u_{yy}$ and $\nabla^2 v = v_{xx} + v_{yy}$ change and depend on J, $\frac{\partial}{\partial u}$, $\frac{\partial}{\partial v}$, $\frac{\partial^2}{\partial u^2}$ and $\frac{\partial^2}{\partial v^2}$

For special case of conformal transformation, it can be make use of the Cauchy-Riemann conditions:

$$\begin{aligned} x_u &= y_v \\ x_v &= -y_u \end{aligned} \tag{B.22}$$

To obtain

$$\nabla^2 u = \nabla^2 v = \gamma = 0 \tag{B.23}$$

and

$$\alpha = \beta = J(u, v) \tag{B.24}$$

Equation (B.21) then reduces to

$$\left(cc_g a_u\right)_u + \left(cc_g a_v\right)_v + Jk^2 cc_g a = 0 \tag{B.25}$$

Equation (B.25) represents the elliptic version of the MSE for a general coordiante system conformal to the Cartesian one. It can be noted that looks similar to equation (B.4) expect for the Jacobin in the last term.

B.2 Parabolization of equation (B.25)

If it is assumed that the wave propagates in the $x-$direction, the water surface displacement can be written as

$$a(u, v) = Re\left\{A(u, v)\, e^{i\int KJ^{1/2}du}\right\} \tag{B.26}$$

where the factor $KJ^{1/2}$ in the phase accounts for the proper accumulation of physical distance as the wave propagates. Since $K(u, v)$ and $J(u, v)$ still vary with v, it is convenient to define a reference phase function based on $K(u, v_0) = K_0(u)$ and $J(u, v_0) = J_0(u)$; i.e., the phase function for one particular line $v = v_0$. Then $K_0 J_0^{1/2}$ will be substitute in equation (B.26) in place of $KJ^{1/2}$. For this case, substituting the assumed form for a (equation B.26) into equation (B.25) produces the following equation

$$\begin{aligned} &cc_g A_{uu} + 2cc_g iA_u K_0 J_0^{1/2} - cc_g AK_0^2 J_0 + cc_g iA\left(K_0 J_0^{1/2}\right)_u + \left(cc_g\right)_u A_u + \\ &+ \left(cc_g\right)_u AiK_0 J_0^{1/2} + cc_g A_{vv} + \left(cc_g\right)_v A_v + JK^2 cc_g A = 0 \end{aligned} \tag{B.27}$$

Then after neglecting the smaller order term (the first and the fifth) $cc_g A_{uu}$ and $(cc_g)_u A_u$ it yields to the parabolic approximation of the MSE

$$\begin{aligned} &2cc_g iA_u K_0 J_0^{1/2} + \left(cc_g K_0 J_0^{1/2}\right)_u iA + (cc_g A_v)_v + \\ &(K^2 J - K_0^2 J) Acc_g = 0 \end{aligned} \tag{B.28}$$

Verification of validity of MSE in conformal mapping coordinate system is done by imposing x=u and y=v, calculating J, that comes equal to 1, estimating the x and y derivatives, it yields to the parabolic MSE in cartesian coordinate system as equation (see the paper of Kirby & Dalrymple, 1994).

B.3 Parabolic MSE in polar coordinate system

The polar transformation results to be a useful choice of a coordinate system from a physical point of view.

$$\begin{pmatrix} x \\ y \end{pmatrix} = r \begin{pmatrix} \cos\theta \\ \sin\theta \end{pmatrix}, \qquad \begin{pmatrix} r \\ \theta \end{pmatrix} = \begin{pmatrix} (x^2+y^2)^{1/2} \\ tan^{-1}(y/x) \end{pmatrix} \tag{B.29}$$

which relates (r, θ) to a Cartesian reference frame with a common origin. However a more appropriate choice of coordinates, which represents a true conformal map, is

$$\begin{pmatrix} x \\ y \end{pmatrix} = r_0 e^u \begin{pmatrix} \cos v \\ \sin v \end{pmatrix}, \qquad \begin{pmatrix} u \\ v \end{pmatrix} = \begin{pmatrix} ln(r/r_0) \\ \theta \end{pmatrix} \tag{B.30}$$

with the domain $(r_0 \leq r \leq \infty)$. The first representation can also be written as $z = r_0 e^w$. The Jacobian of this transformation results to be

$$J = x_u y_v - x_v y_u = r_0^2 e^{2u} \tag{B.31}$$

since

$$\begin{aligned} x_u &= r_0 e^u \cos v; \qquad x_v = -r_0 e^u \sin v \\ y_u &= r_0 e^u \sin v; \qquad y_v = r_0 e^u \cos v \end{aligned} \tag{B.32}$$

By inserting the Jacobian (B.31) into the parabolic MSE (B.28)

$$\begin{aligned} &2cc_g iK_0 r_0 e^u A_u + (cc_g K_0 r_0 e^u)_u iA + (cc_g A_v)_v + \\ &(K^2 r_0^2 e^{2u} - K_0^2 r_0^2 e^{2u}) Acc_g = 0 \end{aligned} \tag{B.33}$$

to find the polar representation, we then use the change of variables

$$r = r_0 e^u \qquad \theta = v \tag{B.34}$$

$$\frac{\partial}{\partial u} = r\frac{\partial}{\partial r} \qquad \frac{\partial}{\partial v} = \frac{\partial}{\partial \theta} \tag{B.35}$$

yields to

$$\begin{aligned} &2cc_g iK_0 r^2 A_r + \left(cc_g K_0 r\right)_r riA + \left(cc_g A_\theta\right)_\theta + \\ &r^2\left(K^2 - K_0^2\right) Acc_g = 0 \end{aligned} \tag{B.36}$$

Appendix C

Thomas algorithm

A tridiagonal system of equations is characterzied by a matrix which has non zero elements only in the central diagonal and in its upper and lower diagonal, an example of such a system is as follows

$$\begin{bmatrix} b_1 & c_1 & 0 & ... & ... & ... & 0 \\ a_2 & b_2 & c_2 & 0 & ... & ... & 0 \\ 0 & a_3 & b_3 & c_3 & 0 & ... & 0 \\ ... & ... & ... & ... & ... & ... & ... \\ 0 & ... & ... & 0 & a_{n-1} & b_{n-1} & c_{n-1} \\ 0 & ... & ... & ... & 0 & a_n & b_n \end{bmatrix} \begin{bmatrix} x_1 \\ x_2 \\ x_3 \\ ... \\ x_{n-1} \\ x_n \end{bmatrix} = \begin{bmatrix} d_1 \\ d_2 \\ d_3 \\ ... \\ d_{n-1} \\ d_n \end{bmatrix} \tag{C.1}$$

where a_i, b_i and c_i are the elements of the lower central and upper diagonals of the matrix respectively; x_i are the unknowns and d_i are the elements of the vector known. The Gaussian elimination is an algorithm which solves a system of linear equation finding the rank of a matrix and calculating the inverse of an invertible square matrix. The simplified case of tridiagonal system can be solved by means of the Thomas algorithm. The solution of a system of n equations in n unknowns is obtained in $O(n)$ operations by using the Thomas algorithm instead of $O(n^3)$.

The algorithm first eliminates the a_i elements of the matrix by modifying the coefficients as follows, denoting the modified coefficients with primes

$$c_i' = \begin{cases} \frac{c_1}{b_1} & ; \quad i = 1 \\ \frac{c_i}{b_i - c_{i-1}' a_i} & ; \quad i = 2, 3, ..., n-1 \end{cases} \tag{C.2}$$

and

$$d'_i = \begin{cases} \frac{d_1}{b_1} & ; \quad i = 1 \\ \frac{d_i - d'_{i-1} a_i}{b_i - c'_{i-1} a_i} & ; \quad i = 2, 3, ..., n \end{cases} \tag{C.3}$$

Then the solution is obtained by a backward substitution as follows

$$\begin{aligned} x_n &= d'_n \\ x_i &= d'_i - c'_i x_{i+1} \qquad ; \; i = n-1, n-2, ..., 1 \end{aligned} \tag{C.4}$$

References

Bellotti, G., Beltrami, G.M., De Girolamo, P., 2003. Internal generation of waves in 2D fully-elliptic mild-slope equation FEM models. *Coastal Engineering* 49(1-2), pp. 71-81.

Bellotti, G., Cecioni, C., De Girolamo, P., 2008. Simulation of small-amplitude frequency-dispersive transient waves by means of the mild-slope equation. *Coastal Engineering* 55, pp. 447-458.

Beltrami, G.M., Bellotti, G., De Girolamo, P., Sammarco, P., 2001. Treatment of wave-breaking and total absorption in a mild-slope equation FEM model. *Journal of Waterway Port Coastal and Ocean Engineering-ASCE* 127(5), pp. 263-271.

Berkhoff, J.C.W., 1972. Computation of combined refraction-diffraction *Proceedings of the 13th International Conference On Coastal Engineering-ASCE*, Vancouver, Canada.

Copeland, G.J.M., 1985. A practical alternative to the mild-slope wave equation. *Coastal Engineering* 9, pp. 125-149.

Dalrymple, R.A., Kirby, J.T., 1988. Models for very wide-angle water waves and wave diffraction. *Journal of Fluid Mechanics* 192, pp. 33-50.

Di Risio, M., 2005. Landslide generated impulsive waves: Generation, propagation and interaction with plane slopes. *Ph.D. Thesis. Third University of Rome*

Di Risio, M., Bellotti, G., Panizzo, A., De Girolamo, P., 2009. Three-dimensional experiments on landslide generated waves at a sloping coast. *Coastal Engineering* 56, pp. 659-671.

Di Risio, M., De Girolamo, P., Bellotti, G.,Panizzo, A., Aristodemo, F., Molfetta, M.G. and Petrillo, A.F., 2009. Landslide-generated tsunamis runup at the coast of a conical island: New physical model experiments. *Journal*

of Geophysical Research 114.

Fritz, H.M., Hager, W.H., Minor, H.E., 2001. Lituya Bay case: rockslide impact and wave run-up. *Sci. Tsunami Hazard* 19, pp. 3-21.

Grassa, J.M., 1990. Directional random waves propagation on beaches. *Proceedings of the International Conference on Coastal Engineering-ASCE*, Delft, Netherland, pp. 798-811.

Grilli, S.T., Vogelmann, S., Watts, P., 2002. Development of a 3D numerical wave tank for modeling tsunami generation by underwater landslides. *Engineering Analysis with Boundary Elements* 26, pp. 301-313.

Huber, A. and Hager, W.K., 1997. Forecasting impulsive waves in reservoirs. In *Commission internationale des grands barrages, Dix-neuvieme Congres des Grands Barrages*, Florence, Italy, pp. 993-1005.

Kervella, Y., Dutykh, D., Dias, F., 2007. Comparison between three dimensional linear and nonlinear tsunami generation models. *Theor. Comput. Fluid Dyn.* 21, pp. 245-269.

Kirby, J.T., Dalrymple, R.A., 1983. A parabolic equation for the combined refraction-diffraction of Stokes waves by mildly varying topography. *Journal of Fluid Mechanics* 136, pp. 453-466.

Kirby, J.T., Dalrymple, R.A., 1984. Verification of a parabolic equation for a propagation of weakly-nonlinear waves. *Coastal Engineering* 8, pp. 219-232.

Kirby, J.T., Lee, C., Rasmussen, C., 1992. Time-Dependent Solutions of the Mild-Slope Wave Equation. *Proceedings of the twenty-third International Conference on Coastal Engineering-ASCE*, Venice, Italy. By Billy L. Edge, (editor), New York, 0-87262-933-3, pp. 391-404, 3600 pp., 3 vols.

Kirby, J.T., Dalrymple, R.A., 1994. Parabolic approximations for water waves in conformal coordinate system. *Coastal Engineering* 23, pp. 185-213.

Kubo, Y., Kotake, Y., Isobe, M., Watanabe, A., 1992. Time-Dependent Mild Slope Equation for Random Waves. *Proceedings of the twenty-third International Conference on Coastal Engineering*, Venice, Italy. By Billy L. Edge, (editor), New York: ASCE, 0-87262-933-3, pp. 419-431, 3600 pp., 3 vols.

Kulikov, E.A., Medvedev, P.P., Lappo, S.S., 2005. Satellite recording of

the Indian ocean tsunami on December 26, 2004. *Doklady Earth Sciences* 401A(3), pp. 444-448.

Lee, C., Kim, G., Suh, K., 2003. Extended mild-slope equation for random waves. *Coastal Engineering* 48(4), pp. 277-287

Lee, C.H., Kim, G., Suh, K.D., 2006. Comparison of time-dependent extended mild-slope equations for random waves. *Coastal Engineering* 53(4), pp. 311-318

Liu, P.L.F., Mei, C.C., 1976. Water motion on a beach in the presence of a breakwater. 1. Waves. *Journal of Geophysical Research* 81, pp. 3079-3094.

Liu, P.L.F., Tsay, T.-K., 1983. On weak reflection of water waves. *Journal of Fluid Mechanics* 131, pp. 59-71.

Lynett, P., Liu, P.L.F., 2002. A numerical study of submarine-landslide-generated waves and run-up. *Proc. The royal Society London* 458, pp. 2885-2910.

Madsen, P.A., Larsen, J., 1987. An efficient finite-difference approach to the mild-slope equation. *Coastal engineering* 11(4), pp. 329-351.

Madsen, P.A., Murray, R., Sorensen, O.R., 1991. A new form of boussinesq equations with improved dispersion characteristics. *Coastal Engineering* 15, pp. 371-388.

Maramai, A., Graziani, L., Tinti, S., 2005. Tsunamis in the Aeolian Island (southern Italy): review. *Marine Geology* 215, pp. 11-21.

Mei, C.C., 1983. The applied dynamics of ocean surface and waves. *World Scientific*, Singapore.

Miller, D.J., 1960. Giant waves in Lituya Bay, Alaska. *U.S. Geol. Surv. Prof. Pap.* 354-c, 86 pp.

Mei, C.C., Tuck, E.O., 1980. Forward scattering by long thin bodies. *SIAM Journal of Applied Maths* 39, pp. 178-191

Mirchin, N., Pelinovsky, E., 2001. Dispersive Intensification of Tsunami Waves. *Int. Tsunami Symposium Proc.* (ITS 2001) Seattle, Washington, USA, 7-10, Session 7, Nos.7-10, pp. 789-794

Monaghan, J.J., Kos, A., 2000. Scott Russell's wave generator *Physics of Fluids* 12(3), pp. 622-630.

Noda, E., 1970. Water waves generated by landslides. *Journal of Waterway, Harbours, and Coastal Engineering Division-ASCE* pp. 835-855.

Nwogu, O., 1993. Alternative form of the boussinesq equations for nearshore wave propagation. *Journal of Waterway Port Coastal and Ocean Engineering-ASCE* 119, pp. 618-638.

Panizzo, A., Bellotti, G., De Girolamo, P., 2002. Application of wavelet transform analysis to landslide generated waves. *Coastal Engineering* 44(4), pp. 321-338.

Panizzo, A., De Girolamo, P., Di Risio, M., Maiastri, A., Petaccia, A., 2005. Great landslide events in Italian artificial reservoirs. *Natural Hazard and Earth System Sciences* 5, pp. 733-740.

Peregrine, D.H., 1967. Long waves on a beach. *Journal of Fluid Mechanics* 27, pp. 815-827.

Prins, J. E., 1958. Characteristics of waves generated by local disturbance. *Transactions, American Geophysical Union*, pp. 865-874.

Radder, A.C., 1979. On the parabolic equation method for water-wave propagation. *Journal of Fluid Mechanics* 95(1), pp. 159-176.

Radder, A.C., Dingemans, M.W., 1985. Canonical equations for almost periodic, weakly nonlinear gravity-waves. *Wave Motion* 7(5), pp. 473-485.

Renzi, E., Sammarco, P., 2010. Landslide tsunamis propagating around a conical island. *Journal of Fluid Mechanics* in press.

Sammarco, P., Renzi, E., 2008. Landslide tsunamis propagating along a plane beach. *Journal of Fluid Mechanics* 598, pp. 107-119.

Smith, R., Sprinks, T., 1975. Scattering of surface-waves by a conical island. *Journal of Fluid Mechanics* 72, pp. 373-384.

Sommerfeld, A., 1964. Lectures on theoretical physics. Academic Press, Inc., San Diego.

Steward, D.R., Panchang, V.G., 2000. Improved boundary condition for surface water waves. *Ocean Engineering* 28, pp. 139-157.

Stokes, G.G., 1847. On the theory of oscillatory waves. *Cmbridge Phil. Soc.* 8, pp. 441-473.

Tadepalli, S, Synolakis, C.E., 1996. Model for the leading waves of

tsunamis. *Physical Review Letters* 77(10), pp. 2141-2144.

Tinti, S., Pagnoni, G., Zaniboni, F., Bortolucci, E., 2003. Tsunami generation in Stromboli island and impact on the south-east Tyrrrhenian coasts. *Natural Hazard and Earth System Sciences* 3, pp. 299-309.

Tinti, S., Manucci, A., Pagnoni, G., Armigliato, A., Zaniboni, R., 2005. The 30 December 2002 landslide-induced tsunamis in Stromboli: sequence of the events reconstructed from the eyewitness accounts. *Natural Hazards and Earth System Sciences* 5(6), pp. 763-775.

Tinti, S., Maramai, A., Armigliato, A., Graziani, L., Manucci, A., Pagnoni, G., Zaniboni, F., 2006. Observations of physical effects from tsunamis of December 30, 2002 at Stromboli volcano, southern Italy. *Bulletin of Volcanology* 68(5), pp. 450-461

Tinti, S., Pagnoni, G., Zaniboni, F., 2006b. The landslides and tsunamis of the 30th of December 2002 in Stromboli analysed through numerical simulations. *Bulletin of Volcanology* 68(5), pp. 462-479.

Van Dongeren, A.R., Svendsen, I.A., 1997. Absorbing-generating boundary condition for shallow water models. *Journal of Waterway Port Coastal and Ocean Engineering-ASCE* 123(6), pp. 303-313.

Watts, P., Grilli, S. T., Kirby, J. T., Fryer, G. J., Tappin, D. R., 2003. Landslide tsunami case studies using a boussinesq model and a fully nonlinear tsunami generation model. *Natural Hazards and Earth System Sciences* 3, pp. 391-402.

Wei, G., Kirby, J.T., 1995. A time dependent numerical code for extended boussinesq equations. *Journal of Waterway Port Coastal and Ocean Engineering-ASCE* 120, pp. 251-261.

Wiegel, R. L., Noda, E. K., Kuba, E. M. Gee, D. M., and Tornberg, G., 1970. Water waves generated by landslides in reservois. *Journal of Waterway Port Coastal and Ocean Engineering-ASCE* 96, pp. 307-333

Yue, D.K.-P., Mei, C.C., 1980. Forward diffraction of Stokes waves by a thin wedge. *Journal of Fluid Mechanics* 99, pp. 33-52.

Zhao, L., Panchang, V., Chen, W., Demirbilek Z., Chhabbra N., 2001. Simulation of wave breaking effects in two-dimensional elliptic harbor wave models. *Coastal Engineering* 42(4), pp. 359-373.